

INVESTIGATION OF BIODEGRADABLE Zn-Li-Cu ALLOYS  
FOR CARDIOVASCULAR STENT APPLICATIONS

by

JACOB STEELE YOUNG

RAMANA G. REDDY, COMMITTEE CHAIR

MARK L. WEAVER

NILESH KUMAR

DANIEL J. FONSECA

VINOY THOMAS

A DISSERTATION

Submitted in partial fulfillment of the requirements  
for the degree of Doctor of Philosophy in the  
Department of Metallurgical and Materials Engineering  
in the Graduate School of  
The University of Alabama

TUSCALOOSA, ALABAMA

2020

Copyright Jacob Young 2020  
ALL RIGHTS RESERVED

## ABSTRACT

Zinc has been recently proposed as a suitable biodegradable material for temporary medical device applications due to an intermediate corrosion rate, high biocompatibility, and ease of processing. While pure zinc fails to meet the minimum mechanical property requirements for cardiovascular stents, Zn can be easily customized through alloying with non-toxic elements to improve both its strength and ductility while maintaining an ideal degradation behavior and biocompatibility.

In this research project, the novel Zn-Li-Cu alloy system has been investigated and developed to optimize the mechanical properties and corrosion behavior for cardiovascular stent applications through simulation and *in vitro* examination.

Through this research work, the primary accomplishments were:

- Synthesized Zn-Li-Cu alloy ingots and sheets through an inert atmosphere casting, annealing, and hot rolling procedure. Individual samples are sectioned, ground, and polished for characterization and corrosion testing.
- Characterized the morphology and chemistry of rolled alloys through optical microscopy, SEM, XRD, EDS, ICP-OES, FTIR, and XPS. Experimental and nominal chemistries are compared through thermodynamic modeling of the Zn-Li-Cu phase diagram with PANDAT software.

- Simulated the biodegradation behavior in the human body through *in vitro* immersion testing and EIS using HBSS to examine weight loss-based corrosion rate, corrosion products and their effect on corrosion resistance, and long-term structural stability.
- Determined the ultimate tensile strength, yield strength, elongation to failure, modulus of elongation, and Vickers hardness of rolled alloys. Tensile fracture surfaces were analyzed to find relationships between mechanical properties, fracture behavior, and alloying element concentration.
- Measured the cell viability and relative metabolic behavior of NIH3T3 fibroblast cells on Zn alloy substrates through indirect MTS cytotoxicity testing to ascertain potential toxicity effects.
- Established the optimal alloy chemistry to best meet the design criteria for cardiovascular stent devices and ascertain avenues for future property improvements and optimization.

## LIST OF ABBREVIATIONS AND SYMBOLS

BM	Biodegradable metal/material
Zn	Zinc
Li	Lithium
Cu	Copper
DRX	Dynamic recrystallization
HCP	Hexagonal close packed
SHE	Standard hydrogen electrode
HBSS	Hank's Balanced Salt Solution
ICP-OES	Inductively coupled plasma – optical emission spectrometry
SEM	Scanning electron microscopy
EDS	Energy dispersive X-ray spectroscopy
XRD	X-ray diffraction
EIS	Electrochemical impedance spectroscopy
FTIR	Fourier transform infrared spectroscopy
XPS	X-ray photoelectron spectroscopy
CALPHAD	<b>C</b> ALculation of <b>P</b> Hase <b>D</b> iagrams
$\Delta G$	Change in Gibbs energy
ANOVA	<b>A</b> Nalysis <b>O</b> f <b>V</b> ariance
MTS	(3-(4,5-dimethylthiazol-2-yl)-5-(3-carboxymethoxyphenyl)-2-(4-sulfophenyl)-2H-tetrazolium)

## ACKNOWLEDGMENTS

My sincere thanks to my graduate research advisor and chairman of my dissertation committee, Professor Ramana G. Reddy, for his consistent instruction, guidance, and aid throughout my doctoral study. Through working with Dr. Reddy during my time as a graduate student, I have come to know him as an excellent advisor, project leader, and scholar who has made an enormous positive impact on my education here at UA.

I would like to also thank my committee members Dr. Mark Weaver, Dr. Nilesh Kumar, Dr. Daniel Fonseca, and Dr. Vinoy Thomas for their valuable insight and advice toward this project.

A big thank you to Johnny Goodwin, Robert Holler, and Michael Buettner from the Alabama Analytical Research Center (AARC) for their time and assistance with instrument training and operation and sample analysis. Additional thanks to Sidhartha Bhattacharyya from the Geochemical Research Laboratory for his help with ICP-OES analysis.

I want to also thank Dr. Shreyas Rao and Raghu Kondapaneni for their extreme generosity, patience, and use of their laboratory for the cytotoxicity analysis. This was the last piece of data to acquire, and their help with this final, critical experiment allowed me to finish during a quite turbulent 2020 year.

I am grateful to all the past and current members of Dr. Reddy's group for their advice and friendship: Dr. Mallikharjuna Bogala, Dr. Hoaxing Yang, Dr. Yuxiang Peng, Dr. Yudong Li, Andrew Kim, Dr. Muhammad Imam, Dr. Pravin Shinde, Nafis Admed, and Khalid Nahian.

Additional thanks to my peers and friends in the Metallurgical and Materials Engineering department at UA. Special thanks to Dr. Zhongqi Liu for all the trips to get coffee to keep me focused.

Finally, this dissertation would not have been possible without the continuous love and encouragement from my family.

## CONTENTS

ABSTRACT .....	ii
LIST OF ABBREVIATIONS AND SYMBOLS .....	iv
ACKNOWLEDGMENTS .....	v
LIST OF FIGURES .....	xi
CHAPTER 1 – INTRODUCTION .....	1
CHAPTER 2 – LITERATURE REVIEW .....	5
2.1 Medical Device Overview.....	5
2.1.1 Modern Stent Fabrication Techniques .....	7
2.2 Biodegradable Materials Summary.....	12
2.2.1 What are Biodegradable Materials? .....	12
2.2.2 Design Constraints for Biodegradable Alloys.....	15
2.3 Why Zinc? .....	18
2.3.1 Benefits and Limitations of Zinc.....	18
2.3.2 Material Selection: Alloying Element Effects in Zinc .....	20
2.3.2.1 Effect of Aluminum on Zinc .....	21
2.3.2.2 Effect of Calcium on Zinc .....	22
2.3.2.3 Effect of Copper on Zinc.....	23

2.3.2.4 Effect of Lithium on Zinc.....	24
2.3.2.5 Effect of Magnesium on Zinc.....	25
2.3.2.6 Effect of Silver on Zinc.....	26
2.3.2.7 Effect of Strontium on Zinc .....	27
2.3.3 Reported Mechanical and Corrosion Properties of Zinc Alloys .....	28
2.3.4 Metal Toxicity in the Human Body .....	32
CHAPTER 3 – HYPOTHESIS AND RESEARCH OBJECTIVES.....	36
CHAPTER 4 - EXPERIMENTAL METHOD .....	38
4.1 Melting and Annealing.....	38
4.2 Hot Rolling.....	39
4.3 Characterization .....	40
4.4 Immersion Corrosion Testing.....	41
4.5 Electrochemical Impedance Spectroscopy Analysis.....	42
4.6 Cytotoxicity Assessment.....	43
4.7 Mechanical Testing .....	44
CHAPTER 5 – RESULTS AND DISCUSSION.....	46
5.1 Alloy Characterization .....	46
5.1.1 Chemical and Phase Analysis .....	46
5.1.2 Optical Microscopy .....	49
5.1.3 Phase Diagram Modelling.....	51

5.2 Corrosion Testing.....	58
5.2.1 <i>In vitro</i> Immersion Corrosion Analysis.....	58
5.2.2 Electrochemical Impedance Spectroscopy Analysis.....	70
5.2.3 Corrosion Product Formation.....	72
5.3 Mechanical Properties.....	76
5.3.1 Tensile Testing.....	76
5.3.2 Vickers Hardness.....	84
5.3.3 Fracture Surface Morphology .....	89
5.4 Cytotoxicity Testing.....	98
CHAPTER 6 - CONCLUSIONS.....	101
6.1 Feasibility Determination of Zn-Li-Cu Alloys.....	101
6.2 Future Work .....	103
REFERENCES .....	106
APPENDIX I – HBSS composition and ion concentration.....	120
APPENDIX II – Zn-Li-Cu CALPHAD TDB code for PANDAT software.....	121
APPENDIX III – Example calculation of corrosion rate .....	129
APPENDIX IV – Example calculation of Vickers hardness .....	131
APPENDIX V – Optical microscopy of NIH3T3 cells .....	132

## LIST OF TABLES

<b>Table 1:</b> Design criteria for biodegradable metal stents. ....	15
<b>Table 2:</b> Average healing time for bone fractures and mechanical properties of bone tissues....	17
<b>Table 3:</b> Summary of alloying element function and toxicology in the adult human body.....	32
<b>Table 4:</b> Nominal and experimental alloy compositions from ICP-OES.....	47
<b>Table 5:</b> Extrapolated $R_{\text{bulk}}$ and $R_{\text{CT}}$ of Zn-0.3Li-3.5Cu after <i>in vitro</i> corrosion. ....	71
<b>Table 6:</b> Mechanical properties of hot-rolled Zn-based alloys from this study and selected Zn alloys from literature. *Data extrapolated from figures in literature. ....	78
<b>Table 7:</b> Simulated equilibrium volume fraction of phases at 25 °C for studied Zn-based alloys. ....	82
<b>Table 8:</b> Composition of HBSS.....	120
<b>Table 9:</b> Ion concentration in HBSS. ....	120

## LIST OF FIGURES

<b>Figure 1:</b> Cardiovascular stent fabrication process summary.....	8
<b>Figure 2:</b> Schematic of necklace grain formation during dDRX.....	10
<b>Figure 3:</b> Schematic mechanisms of cDRX for (a) homogeneous increase of misorientation, (b) lattice rotation near grain boundaries, and (c) microshear band grain formation. Dashed lines are LAGBs and bold lines are HAGBs.....	11
<b>Figure 4:</b> Ideal mechanical integrity and degradation behavior throughout the lifetime of a BM device.....	13
<b>Figure 5:</b> Comparison of UTS for reported hot-rolled and extruded biodegradable Zn alloy classes.....	29
<b>Figure 6:</b> Comparison of elongation to failure for hot-rolled and extruded reported biodegradable Zn alloy classes.....	30
<b>Figure 7:</b> Comparison of <i>in vitro</i> immersion corrosion rate for reported Zn alloy classes.....	31
<b>Figure 8:</b> (a) Melting setup in inert atmosphere glovebox; (b) Annealing furnace with attached Ar gas line.....	39
<b>Figure 9:</b> (a) Stanat hot rolling instrument; (b) Example hot-rolled metal sheets.....	40
<b>Figure 10:</b> (a) Schematic of <i>in vitro</i> immersion corrosion experiment, where (1) HBSS, (2) hot-rolled alloy sample, (3) Nylon wire, (4) drying oven with air atmosphere; (b) Example long-term corrosion experiment setup.....	41
<b>Figure 11:</b> Tensile testing setup of Zn alloy dogbone-shaped sample with extensometer attached.....	44
<b>Figure 12:</b> Tensile test sample dimensions; all measurements in mm.....	45
<b>Figure 13:</b> Theoretical vapor pressures of Li, Zn, and Cu compared to Ar atmosphere vs. temperature [112].....	48
<b>Figure 14:</b> XRD patterns of hot-rolled Zn-based alloys, where $\blacktriangledown = \text{Zn}$ , $\circ = \alpha\text{LiZn}_4$ , and $\diamond = \epsilon\text{CuZn}_5$ .....	49

<b>Figure 15:</b> Optical micrographs of hot-rolled (a) Zn, (b) Zn-0.3Li, (c) Zn-3.5Cu, (d) Zn-0.3Li-2Cu, (e) Zn-0.3Li-3.5Cu, and (f) Zn-0.3Li-5Cu. ....	50
<b>Figure 16:</b> Binary phase diagram of Cu-Zn modeled in PANDAT using a CALPHAD approach. ....	52
<b>Figure 17:</b> Abbreviated binary phase diagram of Li-Zn modeled in PANDAT using a CALPHAD approach. ....	53
<b>Figure 18:</b> Binary phase diagram of Cu-Li modeled in PANDAT using a CALPHAD approach. ....	54
<b>Figure 19:</b> Abbreviated ternary Zn-Li-Cu phase diagram modeled with PANDAT using a CALPHAD approach. Studied chemistries are marked with red stars. ....	55
<b>Figure 20:</b> Solidification diagram of Zn-0.3Li-3.5Cu. ....	56
<b>Figure 21:</b> Gulliver-Scheil solidification diagram for Zn-0.3Li-3.5Cu. ....	57
<b>Figure 22:</b> Representative morphologies of the corrosion products from Zn alloys after (a) 5 days and (b) 21 days. ....	59
<b>Figure 23:</b> (a) SEM micrograph of 5-day corrosion of Zn; (b) EDS of oxide layer; (c) SEM micrograph of corrosion precipitate agglomerate after 21 days; (d) EDS of agglomerate. ....	60
<b>Figure 24:</b> FTIR analysis of corrosion product agglomerates after <i>in vitro</i> immersion in HBSS. ....	61
<b>Figure 25:</b> XPS spectra of Zn and Zn-0.3Li-3.5Cu corrosion product after 50 days <i>in vitro</i> immersion. ....	62
<b>Figure 26:</b> Cross-section SEM micrographs of pure Zn after (a) 5 days, (b) 12 days, (c) 21 days, and (d) 50 days of immersion corrosion. ....	65
<b>Figure 27:</b> SEM micrographs of (a) surface and (b) cross-section of Zn-0.3Li-3.5Cu after 100 days of immersion corrosion. ....	66
<b>Figure 28:</b> Oxide layer thickness with respect to <i>in vitro</i> immersion duration for pure Zn and Zn-0.3Li-3.5Cu samples. ....	67
<b>Figure 29:</b> <i>In vitro</i> corrosion rate in HBSS of selected Zn-based alloys after 21 days. ....	68
<b>Figure 30:</b> Comparison of <i>in vitro</i> corrosion rate of pure Zn in HBSS with and without solution stirring. ....	69
<b>Figure 31:</b> Nyquist plot of EIS measurement of Zn-0.3Li-3.5Cu after <i>in vitro</i> corrosion. ....	70

<b>Figure 32:</b> Extrapolated curve lines associated with (a) $R_{\text{bulk}}$ and (b) $R_{\text{CT}}$ from Nyquist plot of Zn-0.3Li-3.5Cu after <i>in vitro</i> corrosion. ....	71
<b>Figure 33:</b> Schematic of the corrosion mechanism of pure Zn in HBSS. ....	73
<b>Figure 34:</b> Representative engineering stress vs. engineering strain curves of hot-rolled Zn-based alloys. ....	77
<b>Figure 35:</b> Change in grain size for pure Zn after hot-rolling. Dotted lines highlight large grains in as-cast Zn. ....	79
<b>Figure 36:</b> Amount of Cu and Li solutes within the $\eta$ Zn phase from 25 – 350 °C for Zn-0.3Li-xCu ( $2 \leq x \leq 5$ ). ....	81
<b>Figure 37:</b> Vickers hardness of hot-rolled Zn-based alloys. ....	85
<b>Figure 38:</b> Schematic diagram of (a) upper bound iso-strain model and (b) lower bound iso-stress model for an alloy composed of phases A and B. ....	88
<b>Figure 39:</b> SEM fracture micrographs of Zn. ....	90
<b>Figure 40:</b> SEM fracture micrograph of Zn-3.5Cu. ....	91
<b>Figure 41:</b> SEM fracture micrograph of Zn-0.3Li. ....	92
<b>Figure 42:</b> SEM fracture micrograph of Zn-0.3Li-2Cu. ....	93
<b>Figure 43:</b> SEM fracture micrograph of Zn-0.3Li-3.5Cu. ....	94
<b>Figure 44:</b> SEM fracture micrograph of Zn-0.3Li-5Cu. ....	95
<b>Figure 45:</b> (a) SEM micrograph and (b) EDS analysis of Zn and Cu content of Zn-0.3Li-5Cu phase regions. ....	96
<b>Figure 46:</b> Schematic of crack propagation through two phase alloy with ductile matrix and brittle second phase with (a) low and (b) high crack tip driving force. ....	97
<b>Figure 47:</b> Cell viability of NIH3T3 cells on (a) pure Zn, (b) Zn-0.3Li-2Cu, (c) Zn-0.3Li-3.5Cu, and (d) Zn-0.3Li-5Cu substrate with respect to extraction concentration and duration. ....	98
<b>Figure 48:</b> Front and side view of corrosion sample. ....	129
<b>Figure 49:</b> Schematic of (a) Vickers hardness indenter and (b) shape of indentation. ....	131
<b>Figure 50:</b> Representative optical images of NIH3T3 cells incubated with 10%, 50%, and 100% pure Zn and negative control extracts for 1, 4, and 7 days. ....	132

**Figure 51:** Representative optical images of NIH3T3 cells incubated with 10%, 50%, and 100% Zn-0.3Li-2Cu alloy and negative control extracts for 1, 4, and 7 days. .... 133

**Figure 52:** Representative optical images of NIH3T3 cells incubated with 10%, 50%, and 100% Zn-0.3Li-3.5Cu alloy and negative control extracts for 1, 4, and 7 days. .... 134

**Figure 53:** Representative optical images of NIH3T3 cells incubated with 10%, 50%, and 100% Zn-0.3Li-5Cu alloy and negative control extracts for 1, 4, and 7 days. .... 135

## CHAPTER 1 – INTRODUCTION

Interest toward biodegradable metals (BMs) as an alternative class of materials for short-term orthopedic and cardiovascular medical device applications has drastically increased within the past decade. Target applications for BMs are stents, meant to maintain blood flow in damaged arteries after balloon angioplasty, and orthopedic fixation devices, designed to support damaged bone during healing. A good BM should be mechanically robust while degrading at a controlled rate to ensure the body tissue heals successfully [1]. The byproducts from BM degradation should not be toxic to the human body and the entire device should disintegrate entirely, absorbed by the body after completion of tissue healing.

Modern biomaterials for implants and stents in production today, such as titanium alloys and stainless steels, have mechanical properties far surpassing human tissue and bone, which can promote detrimental stress shielding effects [2,3]. Additionally, current implant devices are not designed to erode, resulting in costly removal surgeries that increase the risk of patient complications. Among the proposed BM alloy systems, magnesium, iron, and zinc have drawn considerable interest due to their favorable biocompatibility, controllable degradation rates, and compatible mechanical properties with human tissues.

Although interest in Mg and Fe alloys have garnered scientific attention for a longer time than Zn alloys, they exhibit significant design complications toward their medical application. Mg alloys demonstrate high corrosion rates, associated with premature degradation of mechanical properties, unwanted hydrogen gas evolution, and pH imbalances [4]. Fe alloys have very low

degradation rates, akin to permanent orthopedic implants, as well as corrosion products that are not absorbed by the human body at an appropriate rate [5]. Zn alloys tend to have corrosion rates between that of Fe and Mg as well as harmless byproducts [6].

While Zn is an attractive potential biomedical material, the mechanical properties of pure Zn significantly lack for BM applications. The primary objective of Zn alloy development is the enhancement of mechanical properties while simultaneously preserving a suitable degradation rate and biocompatibility. Methods to tune the properties of Zn include the introduction of alloying elements to promote intermetallic phase precipitates and grain refinement through thermomechanical synthesis processes.

Copper is a promising alloying element as Tang et al. [7] found that additions up to 4 wt.% improved tensile strength and dramatically increased ductility, although tensile strength does not meet the general design criteria for stents [8]. While adhering to the recommending daily allowance of  $900 \mu\text{g day}^{-1}$  [9], Cu is non-toxic and is proven to be not cytotoxic in previous studies [10,11]. Lithium as an alloying element has been initially investigated by Zhao et al. [12] and Yuan et al. [13], finding that additions of Li in Zn, up to the eutectic point of 0.4 wt.%, enhance mechanical strength and ductility. Alloys with Li content  $< 0.4 \text{ wt.}\%$  do not have satisfactory ductility, while surpassing the eutectic point led to a sudden brittle behavior [12]. *In vitro* corrosion rate determined by Tafel curve extrapolation compared similarly to pure Zn, while long term *in vivo* corrosion rate of Zn-0.1Li in rat abdominal aorta was increased after six months with uniform gradual acceleration [14]. The recommended daily allowance of Li is suggested as  $1000 \mu\text{g day}^{-1}$  [15].

This dissertation research study investigates and addresses the shortcomings of Zn-Cu and Zn-Li alloy systems through simultaneous alloying of Zn with both Cu and Li in order to meet mechanical property and corrosion behavior design goals. Chapter 2 provides a comprehensive background on current medical device technologies and materials, as well as design goals and challenges of BM devices. Chapter 3 presents the research hypothesis based on literature review of reported Zn alloy systems as well as the specific objectives of this study. Chapter 4 explains details regarding alloy synthesis, material characterization, and property analysis. Chapter 5 presents the characterization, data, and analysis regarding each of the following topics: (1) the CALPHAD-based modeling of the Zn-Li-Cu ternary phase diagram and determination of processing conditions; (2) the chemical and microstructural characterization of the selected alloy compositions; (3) the *in vitro* corrosion behavior of selected alloys in a simulated body fluid; (4) the mechanical properties, strengthening mechanisms, and failure analysis with regard to composition and phase fraction; (5) an overview on potential cellular toxicity of pure Zn and Zn-0.3Li-*x*Cu alloys using indirect cytotoxicity testing methods. Finally, Chapter 6 provides a summarization of the entire works, conclusions regarding the feasibility of utilizing Zn-Li-Cu alloys for medical devices, and suggestions for future studies.

This doctoral dissertation is partially based on one conference proceedings article and one technical article, both of which are related to the feasibility of Zn-Li-Cu alloys for biomedical device applications. The references are listed below:

1. **J. Young**, R.G. Reddy, Investigation of Biodegradable Zn-Li-Cu Alloys for Orthopedic and Cardiovascular Applications, TMS 2019 148<sup>th</sup> Annual Meeting & Exhibition Supplemental Proceedings, (2019) 809–818.

2. **J. Young**, R.G. Reddy, Synthesis, mechanical properties, and *in vitro* corrosion behavior of biodegradable Zn-Li-Cu alloys, J. Alloys Compd. 844 (2020) 156257.

## CHAPTER 2 – LITERATURE REVIEW

### 2.1 Medical Device Overview

Through the need for long-term, external bodily support and the ceaseless progress of medical engineering over the centuries, man-made implant devices have been developed to replace missing body structures, enhance current biological anatomy, and support impaired bodily functions. Many of the biological implant devices available today can be categorized as neurological implants [16], cardiovascular implants [17], orthopedic implants [18], cosmetic implants [19], structural implants [20], or dental implants [21]. The United States was estimated to have a medical device market value of \$156 billion in 2017 and is expected to grow to \$208 billion by 2023 [22]. The rising demand for medical devices can be attributed to the rise in automobile and trauma injuries, cardiovascular issues related to an increasingly sedentary lifestyle and poor eating habits, and a growing aging population as average life expectancy rises [23].

Orthopedic surgery involves of the replacement, fixation, and support of fractured or broken bone tissues in the human body [24]. Bone damage is caused by the application of external force that exceeds the strength of bone tissue, mostly commonly categorized as traumatic injuries. After fracture, the remaining bone tissue is supplemented by orthopedic implants that either bind the tissues together to promote healing, or to entirely replace the missing bone tissue. Orthopedic devices for fixation are typically nontoxic, non-degradable, metal alloy screws, pins, plates, and wires, while implants for permanent bone replacement can be more complex shapes. Modern

implant alloys include 316 stainless steels, Co-Cr-Mo alloys, coated Ti alloys, NiTi, and Ni-free shape memory alloys [25].

Heart disease is a general term for the range of problems that cause a decline in the function of heart muscles, vessels, or rhythm. Reduction in heart function leads to reduced circulation of blood and the nutrients it carries throughout the body. These cardiovascular issues commonly lead to fatal heart attack or stroke, thus medical attention to treatment and prevention is significant. A prevalent heart disease is coronary artery disease (CAD) which is caused by the buildup of plaque and narrowing of interior artery walls, inhibiting blood flow [26]. Starting with the development of balloon angioplasty by Grüntzig in 1977 [27], stent implants are the primary means of treating CAD.

Stents are tubular medical devices, primarily metal alloys, used as scaffolds to support the interior of an artery until the risk of blockage is reduced. For implantation, the stent is placed around a deflated balloon catheter and inserted into the narrowed artery, a process known as balloon angioplasty [28]. Upon placement, the balloon is inflated, expanding the stent permanently to the required diameter. The balloon is removed, while the stent remains to provide radial support to the artery for life.

Permanent stent materials require certain physical attributes to be successful devices [29]. Most obvious is suitable biocompatibility with the human body, specifically in blood and plasma in veins and arteries, as this is the normal environment for stents. Additionally, the stent material should not degrade or corrode over the life of the product (i.e. human lifespan). Mechanically, stents require a lower yield strength to allow for expansion during implantation. Simultaneously, high tensile properties after expansion are desired for the stent to stay open and to minimize

material volume. To achieve this, a large work-hardening factor should be present for the stent to strengthen upon expansion. Finally, significant ductility is required in order to deform and preserve strength during expansion. Notably, many of these are competing properties (i.e. strength and ductility), therefore careful optimization is required during material selection and design. Alloys used in modern devices are valued for their excellent mechanical properties and radial strength, low mass, and unparalleled corrosion resistance. Popular materials used in production include 316 stainless steels, CoCr alloys, Nitinol, PtCr alloys, and Ti alloys [29–31].

As medical knowledge and technology has advanced, so has the expected quality of medical products and associated patient quality of life. While corrosion resistant alloys are excellent for permanent devices, new materials required development to meet the clinical needs of short-term issues, such as tissue healing or blood vessel blockage. Polymers have traditionally been utilized for their biodegradable nature as sutures, but they lack the structural properties to support surrounding tissue. Mechanically strong and ductile alloys that dissolve over time are the ideal candidate for this new temporary device class.

### 2.1.1 Modern Stent Fabrication Techniques

While a plethora of alloys are used for prevailing stent products, the majority are synthesized through a common casting and thermomechanical procedure, summarized in Figure 1 [1,29,32]. Stent production starts with bulk alloy synthesis into a billet or ingot geometry. Casting involves the liquid metal poured quickly into a simple mold of the desired ingot size, followed by solidification either naturally by atmospheric cooling or artificially quickly using chillers or quenching. Annealing is often done after casting to promote phase equilibrium and elimination of localized element concentration differences. Inert atmospheres, either vacuum or a

shielding gas, are often used during casting and annealing to prevent oxide formation and melt loss.

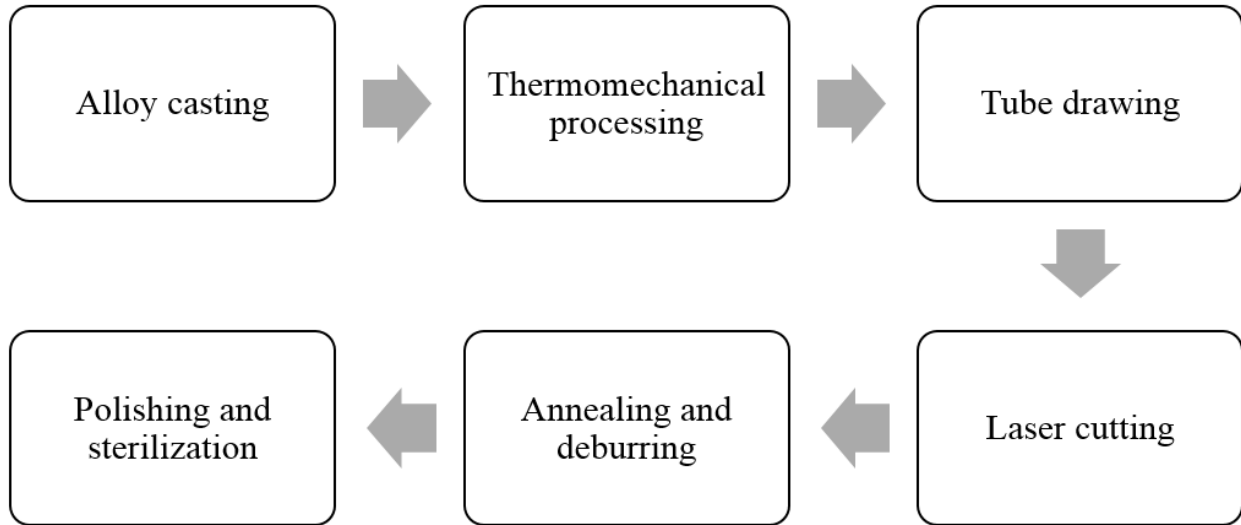


**Figure 1:** Cardiovascular stent fabrication process summary.

Mechanical processing procedures are utilized at elevated temperatures to easily shape the raw ingots into approximate product geometries (i.e. tube, plate, etc.) during commercial production. Common thermomechanical techniques include rolling, extrusion, drawing, and forging. Often, these processes are performed at selected elevated temperatures to permit deformation of the alloys without fracture and promote certain mechanical strengthening mechanisms while limiting oxide scale formation. Alloys can be strengthened during thermomechanical processing through two synchronistic mechanisms: work hardening and dynamic recrystallization.

Work hardening is the strengthening of a metal through the buildup and entanglement of defects through plastic deformation [33]. As a material plastically deforms, the dislocation density increases and defects increasingly impede the movement of one another, raising the stress required for further plastic deformation. Dynamic recrystallization (DRX) is the nucleation and

growth of new, stress-free grains during high shear deformation at  $>0.5 T_M$  [34]. When the strain rate is also high, two main subtypes of DRX are viable depending on the stacking fault energy (SFE) of the material: discontinuous dynamic recrystallization (dDRX) and continuous dynamic recrystallization (cDRX) [35].

When a material's SFE is low, dDRX is more prevalent, illustrated in Figure 2. Partial dislocations are easier to form, therefore wider stacking faults are possible. Localized strain increases rapidly since cross-slip and climb mechanisms are difficult to activate. Near the grain boundaries, strain-induced subgrains are initially formed. As the dislocation density increases, capillary forces are overcome, forming a necklace of new, smaller, stress-free grains along previous grain boundaries. The dDRX process repeats itself through these two distinct steps of strain buildup followed by strain release through grain nucleation.

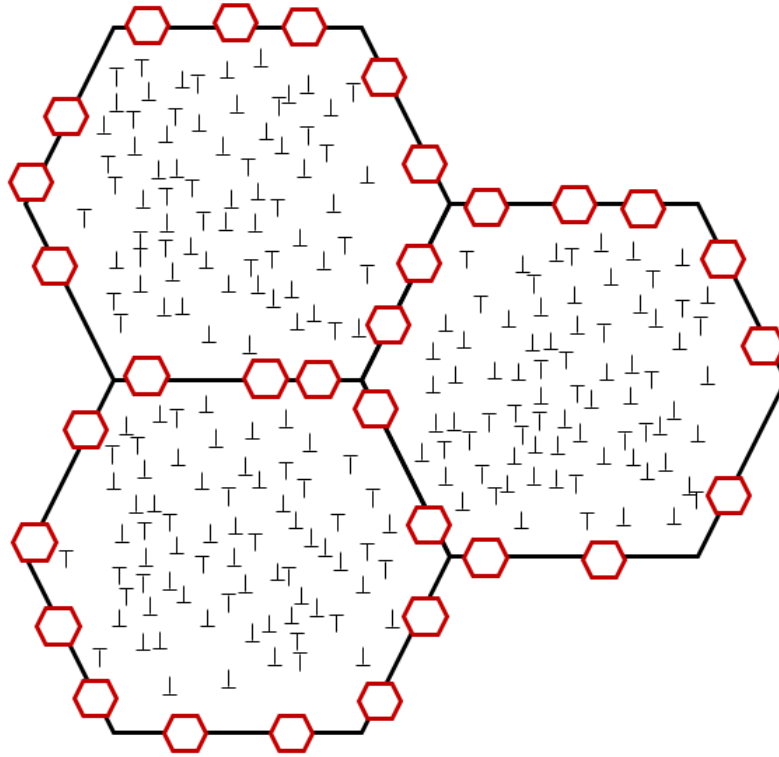


**Figure 2:** Schematic of necklace grain formation during dDRX.

Conversely, high SFE leads to cDRX, manifested in three variations through the formation of localized, high misorientation subgrains, shown in Figure 3. When SFE is large, cross-slip and glide are preferred over partial dislocation creation, leading to crystal structure misorientation and new grain boundaries. The first variation of cDRX is a homogeneous increase of misorientation, occurring at relatively high temperatures. Dislocations accumulate within a given grain and consolidate into low angle grain boundaries (LAGBs) and eventually into high angle grain boundaries (HAGBs). Lattice rotation at grain boundaries can also occur at moderate deformation temperatures and in systems with a lack of independent slip systems (i.e. HCP crystal structures). Local shearing develops near grain boundaries, forming subgrains and LAGBs through absorption of dislocations through climb. HAGBs eventually develop and the process can repeat at these new boundaries. The last variation is the creation of microshear bands

at relatively low strains during hot deformation. Dislocations are arranged into shear bands within each grain, quickly forming LAGBs and HAGBs at shear band intersections, evolving into an equiaxed, fine microstructure.

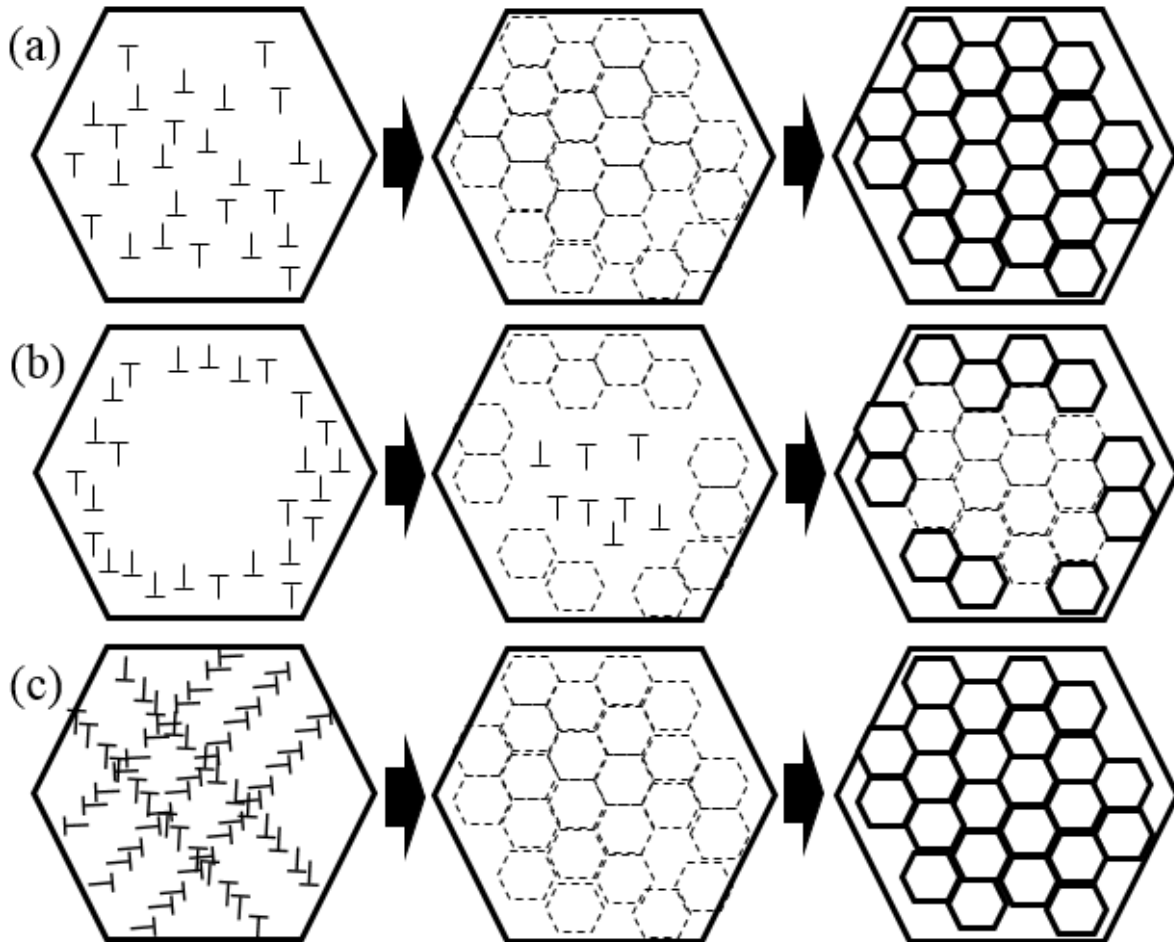


**Figure 3:** Schematic mechanisms of cDRX for (a) homogeneous increase of misorientation, (b) lattice rotation near grain boundaries, and (c) microshear band grain formation. Dashed lines are LAGBs and bold lines are HAGBs.

Following thermomechanical processing and tube drawing, the material is the approximate diameter for stent production. Automated laser cutting is utilized to remove material accurately and without flash to create the finalized mesh-like geometry. During laser cutting, inert gases, such as argon or nitrogen, are used as an atmosphere to inhibit corrosion and cracking. Localized

residual stress can be a product of the generated heat from the laser, so a brief annealing step is necessary to relieve stress and restore mechanical properties.

The final steps of traditional stent production focus primarily on product surface finish. Acid pickling is utilized to remove extra material (i.e. burrs, extra tubing, surface debris) as well as any oxide scaling that has built up during elevated temperature processing. Electropolishing is utilized last to remove any remaining burrs and defects generated during forming and cutting to form a smooth surface with low roughness. Before biological use, stents are exposed to certain  $\gamma$ -radiation or UV radiation briefly to sterilize the products for optimal biocompatibility [1].

## 2.2 Biodegradable Materials Summary

### 2.2.1 What are Biodegradable Materials?

Bioabsorbable metals are a recently developed class of materials meant to replace traditional, corrosion resistant alloys for biomedical implant applications. BMs are metals or alloys that are meant to aid the repair of tissues and arteries, while slowly dissolving *in vivo* after healing is completed, eliminating the need for device removal procedures. A primary requirement is mechanical integrity during tissue healing; the corrosion rate of the BM cannot be too fast or the device will fail. Conversely, BMs need to fully dissolve after tissue has started remodeling itself when mechanical support is no longer necessary. A schematic of degradation quantity and mechanical integrity over the lifetime of a BM is shown in Figure 4.

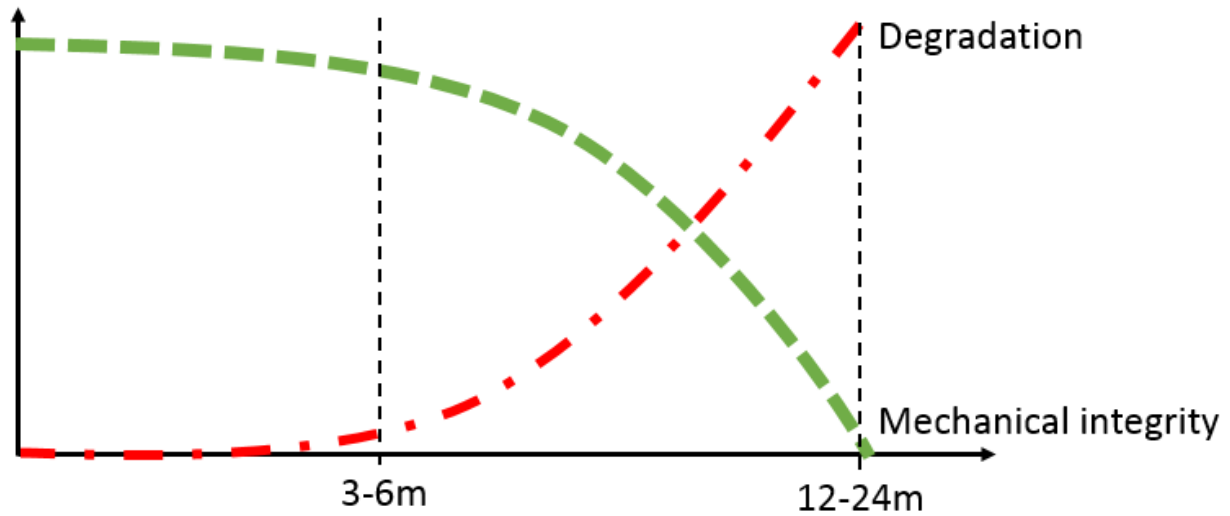
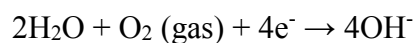
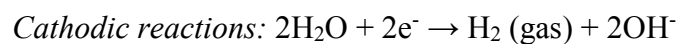
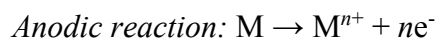


**Figure 4:** Ideal mechanical integrity and degradation behavior throughout the lifetime of a BM device.

Biocompatibility of the BM alloying elements and their corrosion products in the human body is also critical. All components of the BM and dissolution products should be easily broken down, metabolized, and either naturally utilized or excreted from the body. Inflammation, thrombosis, scarring, and cytotoxic effects should be minimized to prevent medical complications.

Degradation is typically carried out by electrochemical reactions, ultimately producing metal oxides, gas byproducts, or other compounds. In the near neutral pH environment of the human body, basic anodic and cathodic reactions are as follows [1,6,36]:



Ideal degradation behavior initiates upon implementation in the body, where the dissolved oxygen in body fluid oxidizes the BM surface into metal ions and released electrons. The cathodic reaction expends the electrons, reducing water into hydroxide ions. Both metal and hydroxide ions combine to form a homogeneous metal hydroxide layer on the entirety of the BM surface. Given favorable conditions, the metal hydroxide product can reduce further into a metal oxide product. Galvanic effects between alloy phases can amplify the corrosion behavior of the BM by acting as pitting corrosion sites. The hydroxide layer is very corrosion resistant and acts as a passivation layer, although will breakdown over time due to buildup of  $\text{Cl}^-$  in pits naturally found in high concentration in the body. Chloride ion buildup and microgalvanic corrosion leads to accelerated pitting corrosion, promoting further  $\text{Cl}^-$  buildup and metal-chloride salt formation, pH decrease, and gradual increase in corrosion rate until the entire BM device is consumed.

Among BM alloys, Fe and Mg systems have received the largest share of scientific attention. Mg implants have been investigated for over 100 years for various medical applications, such as ligatures, sutures, musculoskeletal devices, and intestine connectors, although commercial implants are still unavailable [37]. While Mg is an attractive candidate for clinical applications due to its nontoxicity, degradability, and high strength, many design challenges still exist. The majority of Mg alloys are strong but brittle, which is not appropriate for expanding stent devices. Additionally, Mg alloys tend to dissolve too quickly in chloride environments, leading to early degradation of mechanical integrity accompanied by evolution of hydrogen gas [31].

Fe-based alloys have also been investigated, largely due to the success of 316L stainless steel as a nontoxic, non-corroding medical device material. *In vivo* studies on pure Fe stents in pigs did not induce any local toxicity or inflammation, however severe limitations were encountered [38]. Fe-based materials predictably have very low degradation rates (e.g. 316L SS), leading to

incomplete device dissolution, hindered tissue regeneration, and bone tissue stress shielding [39]. Additionally, hazardous iron oxide corrosion byproducts are observed to be retained in the body, challenging the feasibility of degradable Fe alloys [40]. The magnetic properties of Fe may also present issues during exposure to strong magnetic forces, such as during Magnetic Resonance Imaging (MRI), which could warp and damage Fe devices.

### 2.2.2 Design Constraints for Biodegradable Alloys

The primary application for biodegradable materials are temporary stents and orthopedic fixation implants, therefore new design requirements have collectively been determined by the research community that differ from traditional permanent devices. While many of the design criteria for biodegradable metals are similar regardless of projected product life, there exists some variation, especially when considering stent vs. orthopedic devices. The most commonly reported design constraints for biodegradable metal stents are listed in Table 1 [8,31,41].

**Table 1:** Design criteria for biodegradable metal stents.

<b>Criteria</b>	<b>Constraints</b>
Product life	Mechanical stability for 3 – 12 months; full absorption within 12 – 24 months.
Biocompatibility	Non-toxic corrosion products; hypoallergenic; non-inflammatory.
Mechanical properties	Yield strength > 200 MPa; ultimate tensile strength > 300 MPa; elongation to failure > 15%; elastic recoil < 4%; >10M cycles before fatigue failure.
Corrosion rate	< 0.02 mm/yr
Microstructure	Homogenous; ideally isotropic.

The nominal operation of a temporary coronary stent in an artery should be less than 2 years. When first implanted, the stent should expand and release drugs to prevent restenosis, maintaining mechanical integrity. After successful treatment to the vein within 1 year,

dissolution of the stent is critical to prevent chronic stent thrombosis and additional long-term treatment [42]. Obviously, biocompatibility is critical; side effects from metal or corrosion product toxicity should be negligible. Additionally, inflammation should be minimized to prevent chronic effects such as chest pain and autoimmune disorders. Corrosion rate is recommended at or below 0.02 mm/yr based on average stent sizes and ideal absorption duration.

The mechanical property criteria give general indications as to how stents should resist deformation, product geometry and mass, and expected product life. Stent yield strength is generally a measure of the material's upper limit to applied load before permanent, plastic deformation occurs. The ultimate tensile strength is a measure of a material's maximum allowable load before breaking. Elongation to failure, synonymous with ductility, is the amount of allowable total strain before material failure, generally preferred at 30% or greater, but a minimum of 15% is acceptable [31].

For balloon-expandable stents, compromise is required between these contradictory properties during product design [29]. Before and during expansion, a low yield strength is optimal, allowing for easy stent crimping during delivery and lower balloon pressures upon expansion. After expansion, high tensile strength is preferred for mechanical stability, smaller stent geometry, and reduction of total foreign material implanted into the body. An increase of tensile properties upon expansion requires a high strain-hardening rate, where strength increases dramatically during plastic deformation, traditionally found in ductile metals and accompanied by loss of ductility. A certain amount of radial expansion is required, therefore strain-hardening behavior and elongation to failure need to be optimized. Upon deflation of the balloon, minimal stent recoil is necessary, generally correlated with the previously mentioned high yield strengths

upon expansion. Finally, fatigue resistance should be high in order to keep mechanical integrity for 1 year, which is related to small-grained microstructures that feature high yield strengths.

Orthopedic fixation implants are much more varied in function and application, while their geometry can also change dramatically (e.g. screws, plates, pins, etc.). The size and shape is dependent on the type of damaged bone needed support. Table 2 lists mechanical properties of two types of bone and average healing time for selected bone fractures. Since the healing time can range from 4 – 24 weeks, the required degradation rate is not a well-defined criterion [1]. Similarly, the mechanical properties of bone tissue vary depending on location and type [43]. Ultimately, multiple alloys may be ideal candidates for separate locations and fractures in the human body. Due to the criteria ambiguity, material selection and design for stents is the primary focus of this dissertation study, although orthopedic applications should be kept in mind for adjacent applicability.

**Table 2:** Average healing time for bone fractures and mechanical properties of bone tissues.

Fracture	Healing time (weeks)	Property	Cortical	Cancellous
Finger	4 – 8	Tensile strength (MPa)	50 – 150	10 – 20
Radius and ulna	8 – 12	Compressive strength (MPa)	100 – 230	2 – 12
Pelvis	6 – 10	Strain to failure	1 – 3	5 – 7
Neck of femur	12 – 24	Modulus (GPa)	7 – 30	0.5 – 0.05

## 2.3 Why Zinc?

### 2.3.1 Benefits and Limitations of Zinc

Zinc alloys were initially developed in the 20<sup>th</sup> century using pressure die casting as a means to substitute tin and lead for printing type for typewriters [44]. With the advent of high-purity zinc (99.99%), zinc alloys became a proven material with excellent mechanical properties as well as aqueous corrosion resistance. A prevalent use of Zn during World War II was its development using gravity casting as a superior bearing material compared to bronze, possessing a lower coefficient of friction and better mechanical properties [45]. The mechanical properties of zinc alloys have continuously been improved over time through the addition of certain alloying elements, such as Al, Cu, Mg, Cr, Sn, and Ti.

Utilizing Zn as structural material has many advantages. Zinc alloys have traditionally been simple to cast, primarily due to its low melting point, high casting fluidity, low as-cast surface roughness, and reasonable mechanical properties [44]. Pressure die casting is the most prevalent and economical zinc processing technique since zinc generally does not require inert atmosphere during casting due to a low chemical reactivity. Additionally, lower processing temperature means die costs are cheaper due to reduced wear over time. Zinc metal is also relatively inexpensive as it's the 23<sup>rd</sup> most abundant element on Earth [46].

With regard to biological applications, zinc exists as a trace element in the human body, consisting of approximately 0.0038% of a normal adult male's body weight [47]. Primarily, zinc is stored in skeletal muscle and bone, therefore any potential release of zinc ions within the body should be safely metabolized through normal processes. While Zn has reasonable corrosion resistance in general aqueous environments, in saline environments Zn tends to corrode at a

controllable, moderate rate compared to magnesium and iron. The electrode half-cell potential (vs. SHE) of Zn (-0.762 V) falls between Fe (-0.447 V) and Mg (-2.372 V), highlighting the medium stability and chemical reactivity of Zn [48]. Within the body, Zn has not been observed to exhibit certain drawbacks associated with Mg and Fe alloys, such as excess hydrogen gas production, harmful corrosion products, or premature loss of mechanical stability.

Despite the prevalent use of zinc alloys in the die casting field during the past century as well as the more recent promising results from *in vitro* and *in vivo* biological experiments, the feasibility of zinc alloys as a BM is still actively investigated due to the inherent limitations and challenges with using zinc, summarized as [45]:

1. As a structural material, as-cast pure Zn only possesses a moderate strength and ductility that does not meet the mechanical design criteria for stents [6]. Common methods utilized for improved strength and ductility are the introduction of certain alloying elements or thermomechanical processing techniques. Careful consideration is needed since strength and ductility are often inversely related.
2. Magnesium-based alloys have been reported to have decreased fatigue strength and elongation to failure during corrosion [49,50]. While fatigue strength and cycles to failure are not well defined for BM products and Zn alloys are not known for low fatigue strength, the interaction between pitting corrosion and fatigue crack propagation in body fluids should be kept in mind.
3. Pure Zn and certain Zn alloys are known to undergo creep in industrial applications with constant loads. Goodwin et al. [51] investigated the creep behavior of aged Zn die cast alloys under loads of 40 – 100 MPa, finding that long-duration primary power-law creep (1 – 2 % creep strain) was observed at room temperature for the duration of the tests (up

to 2000 h). Creep resistance can be improved through alloying with certain elements, primarily Al and Cu.

4. The low melting point of Zn can contribute to long-term weakening effects on strength and ductility due to aging or static recrystallization (SRX). Natural metal aging is a spontaneous process at low temperatures where highly mobile atoms allow for thermodynamically stable phase transformation, changing mechanical properties and physical geometries. Jin et al. [52] observed aging in Zn-0.8Mg alloy due to formation and migration of the  $Mg_2Zn_{11}$  precipitate phase to grain boundaries. SRX is another thermodynamically spontaneous process at low temperatures where high mobility atoms will allow for recrystallization without applied effects, reducing work hardening and strengthening effects from previous processing [53]. While DRX and alloying are observed to inhibit SRX, fine grain sizes accompanied by stored energy should be minimized.

While the natural degradation rate of Zn in body fluid is optimal, the mechanical properties need to be optimized based on the various phenomena observed which weaken Zn. The most prevalent method of altering the properties of Zn is through alloying; therefore, materials selection of the appropriate alloying elements is critical in order to meet the mechanical, corrosion behavior, and biocompatibility design criteria.

### 2.3.2 Material Selection: Alloying Element Effects in Zinc

Zinc is the 4<sup>th</sup> most prevalent metal in use for a plethora of applications, including but not limited to galvanization, bearings, automobiles, batteries, and zinc oxide compounds [54]. In 2019 alone, approximately 13 million tons of zinc metal was produced worldwide [46]. Zinc

alloys display an expansive range of microstructure, mechanical properties, and degradation behavior with respect to elemental composition and processing parameters. Alloying elements are normally chosen for their improvements to mechanical properties, corrosion resistance, or transport properties. Common alloying elements for commercial applications are aluminum, calcium, copper, lithium, magnesium, silver, and strontium. With design constraints for biological implants in mind, the previously reported effects of these elements on zinc are summarized to assist with future materials selection in order to overcome pure zinc's limitations.

#### 2.3.2.1 Effect of Aluminum on Zinc

Aluminum (Al) is a nonessential element in the human body that is ingested in small amounts through food ingredients and preparation, excreted primarily in urine [55]. Toxicity of Al in the body through ingestion is questionable, although evidence of neurotoxicity to certain organs is present. Zinc-aluminum alloys (e.g. ZA-27) are commonly used as bearing materials due to easy machinability, similar as-cast tensile strength to grey cast iron, and low friction surface [56]. A maximum solubility of ~1 wt% Al in Zn is allowable, while greater concentrations of Al promote  $\beta$ ZnAl phase to precipitate as dendrites [57].

Mechanical properties of Zn-Al alloys vary greatly with quantity of Al and processing parameters [58]. Sand casting and gravity casting have slower cooling rates than die-casting, promoting larger microstructure and lower strength properties. Additionally, hardness, ductility, and yield stress increase with larger Al content (5 – 25%), correlated to volume fraction of  $\beta$  dendrites.

Corrosion resistance of Zn-Al alloys has been investigated by Ares et al. [59] and Osório et al. [60] in 3% NaCl solution. While Al content certainly has an effect on corrosion resistance, the

primary factor is the distribution of Al in phases and microstructure of the dendrites. In hypoeutectic alloys, finer dendritic microstructures improve corrosion resistance, while coarser dendrites in hypereutectic alloys yield higher resistance. The amount of corrosion products and the thickness of product layer increases with Al content, although the product layer is harder to reduce with larger Al content.

#### 2.3.2.2 Effect of Calcium on Zinc

Calcium (Ca) is one of the primary elements that influence development of skeletal bone growth and bone mass/density [61]. While not a common alloying element of Zn, Ca is frequently used during the steelmaking process, as a strengthening element in Al alloys, and in lead-calcium automotive batteries [62–64]. Ca has a negligible solid solubility within Zn, with up to ~5 wt.% Ca forming a two phase alloy consisting of a Zn matrix with dispersed  $\text{CaZn}_{13}$  precipitates [65]. Thermomechanical processing promotes a more homogeneous and smaller grain morphology of Zn and  $\text{CaZn}_{13}$ .

Both as-cast and mechanically processed Zn-Ca alloys display larger tensile yield and ultimate tensile strengths, compressive yield strength, and ductility compared to pure Zn, attributed to the precipitation of the  $\text{CaZn}_{13}$  phase. After 8 weeks of *in vitro* immersion, the alloy has a slight decline in tensile strength and ductility [66].

The corrosion rate of Zn-Ca alloys in HBSS using both electrochemistry and immersion testing methods is larger compared to pure Zn. A uniform corrosion product layer is observed on the surface of the alloy with minimal pitting or galvanic corrosion, preserving the mechanical strength [66].

### 2.3.2.3 Effect of Copper on Zinc

Copper (Cu) is an essential elemental in the human body, combining with proteins to produce critical enzymes for a variety of functions [67]. Commercially, Cu alloys are the third largest metal group, broadly used for their superb electrical and thermal properties, corrosion resistance, anti-bacterial properties, good strength, high ductility, and range of available manufacturing methods [68]. Cu and Zn are frequently alloyed together to form a variety of brasses, bronzes, and other specialty alloys. Up to 14 wt.% Cu in as-cast Zn alloy results in a primary  $\eta$ Zn matrix with a dendritic  $\epsilon$ CuZn<sub>5</sub> intermetallic phase [69]. The volume fraction of  $\epsilon$ CuZn<sub>5</sub> increases and dendrite arm spacing decreases with more Cu content. After extrusion of Zn-Cu alloys, an inhomogeneous finer grain size is achieved. The  $\epsilon$ CuZn<sub>5</sub> phase is lengthened along the extrusion direction, while the  $\eta$ Zn grains are progressively smaller with closer proximity to the intermetallic phase [7]. Increasing Cu content was found to result in an overall finer equiaxed microstructure.

Extruded Zn-Cu alloys exhibit dramatically increased tensile properties with increased Cu content when compared to pure Zn. This was largely accredited to the high solid solubility of Cu in Zn, similar hexagonal crystal structure between  $\eta$ Zn and  $\epsilon$ CuZn<sub>5</sub>, and the gradient microstructure [7].

Zn-Cu alloys observe an increased *in vitro* corrosion rate compared to pure Zn in c-SBF solution [7]. A compact corrosion product composed of mainly Zn(OH)<sub>2</sub> is formed on the metal surface, increasing corrosion resistance. Traditionally, the addition of Cu and subsequent  $\epsilon$ CuZn<sub>5</sub> phase would suggest the presence of galvanic corrosion between noble Cu and more reactive Zn. Due

to only a small increase in corrosion rate compared to pure Zn and no significant differences between various Cu concentrations (up to 4 wt.%), the galvanic effect is experimentally minimal.

*In vivo* testing of Zn-0.8Cu by Zhou et al. [70] observed a reasonable degradation rate after 24 months after stent implantation, where 28 vol.% remained. Mechanical integrity was maintained after 6 months with no toxicity or inflammatory issues in the tested artery.

#### 2.3.2.4 Effect of Lithium on Zinc

Lithium (Li) is not commonly used as an alloying element in Zn, but is regularly ingested in the human body in small amounts and is prescribed as an effective medication for controlling mania and bipolar disorders [71]. From the Zn-Li phase diagram, Li has a solid solubility limit at approximately 0.1 wt.% and a eutectic point between  $\eta\text{Zn}$  and  $\beta\text{LiZn}_4$  at 0.4 wt.% [72,73]. Zhao et al. [12,14] initially investigated Zn-Li binary alloys for biodegradable applications. For an as-cast hypereutectic alloy, small amounts of a  $\text{Zn}+\text{LiZn}_4$  eutectic mixture are present within a  $\eta\text{Zn}$  matrix. A cast eutectic alloy consists of a lamellar of  $\eta\text{Zn}+\text{LiZn}_4$  and  $\eta\text{Zn}$  grains in random orientations. The hypoeutectic Zn-Li alloy produces a dendritic microstructure of  $\eta\text{Zn}+\text{LiZn}_4$  with interdendritic channels of  $\eta\text{Zn}$ . After hot rolling, a hypereutectic alloy exhibits an equiaxed microstructure, while alloys with Li content above 0.4 wt.% have a severe rolling texture with refined dendritic arms. Based on the phase diagram, it can be assumed that all  $\beta\text{LiZn}_4$  transforms into  $\alpha\text{LiZn}_4$  given appropriate annealing/homogenization conditions.

Zn-Li alloys exhibit increased yield and ultimate tensile strengths, as well as increased hardness, with larger contents of Li (i.e.  $\text{LiZn}_4$ ) [12,74]. Using traditional processing methods like extrusion or hot rolling, ductility is drastically decreased with additional Li content above the eutectic point, possibly limiting stent applications for hypoeutectic Zn-Li alloys.

The corrosion rate of Zn-Li alloys is an order of magnitude lower than pure Zn in m-SBF solution [12]. After two weeks of immersion, a protective layer of apatite phase spherical particles with a diameter of  $\sim 1 \mu\text{m}$  is observed, raising alloy corrosion resistance. The eutectic alloy was found to have the lowest corrosion rate of the Zn-Li alloys tested. In general, the corrosion rates and products closely emulate pure Zn in previous *in vitro*, plasma, and blood studies.

#### 2.3.2.5 Effect of Magnesium on Zinc

Magnesium (Mg) is a critical component of the human body which regulates nerve and muscle function, activates Vitamin D, aids calcium and potassium transportation, and helps control glucose levels [75–77]. Mg is the lightest of the commonly used light metals and its alloys are frequently the preferred material when a high strength-to-weight ratio and high stiffness is required, such as in the automotive and aerospace industries. Based on the Mg-Zn phase diagram, small amounts of Mg added to Zn form a hypoeutectic alloy containing primary Zn dendrites with a eutectic interdendritic mixture of Zn +  $\text{Mg}_2\text{Zn}_{11}$  [78,79]. After thermomechanical processing, an elongated texture is observed with Zn regions separated by thin  $\text{Mg}_2\text{Zn}_{11}$  rows [80]. Increased Mg content further produces a larger amount of  $\text{Mg}_2\text{Zn}_{11}$ , forming an interconnected network.

A direct relationship exists between alloy mechanical properties and Mg concentration, investigated by Kubásek et al [80]. Hardness, compressive strength, and tensile strength all increase with increasing Mg content, attributed to precipitation of  $\text{Mg}_2\text{Zn}_{11}$ . Elongation to failure initially increases up to  $\sim 1 \text{ wt.}\%$  Mg, but sharply declines below pure Zn.  $\text{Mg}_2\text{Zn}_{11}$  is a naturally brittle intermetallic, where the microstructure evolves from separated fine grains to a connected

network as Mg content increases. The interconnected brittle phase enables cracks to propagate through the alloy with extreme ease with applied stress.

With even minor additions of Mg, the corrosion rate of Zn-Mg alloys increase in HBSS [6]. As the concentration of Mg increase, the corrosion rate further increases.  $Mg_2Zn_{11}$  and the eutectic phase are more reactive than Zn and corrode first. A corrosion product layer is formed on the alloy, primarily composed of Zn, Mg, O, P, and Ca, assumed to be various metal oxides and phosphates.

#### 2.3.2.6 Effect of Silver on Zinc

Silver (Ag) is frequently used in chemical cauterization of wounds and burns (i.e.  $AgNO_3$ ) as well as an alloy within dental implants [81]. Additionally, Ag has been noted to have significant antibacterial properties due to the prevention of bacterial adhesion by silver ions or nanoparticles [82]. From the Zn-Ag phase diagram, as-cast Zn-alloys containing Ag content greater than 2.5 wt.% produces a fine-grained  $\eta$ Zn matrix with  $\epsilon AgZn_3$  dendrites, where  $\epsilon AgZn_3$  content is proportional to Ag concentration [83]. Below 2.5 wt.%, Ag is completely in solid solution in Zn. Thermomechanical processing forms an equiaxed grain structure where fine  $\epsilon AgZn_3$  precipitates are dispersed along grain boundaries.

Sikora-Jasinska et al. [84] and Li et al. [85] investigated the mechanical properties of Zn-Ag alloys. After hot extrusion, Ag additions improve yield strength and ultimate tensile strength at room temperature compared to pure Zn. Additionally, ductility is overall increased, although minimal differences were observed between Zn-Ag binary alloys (up to 7 wt.% Ag). The improvement of mechanical strength is attributed to the large Zn-Ag solid solution and grain refinement due to  $\epsilon AgZn_3$  at grain boundaries.

Zn-Ag alloys have marginally faster corrosion rates than pure Zn during electrochemical and weight loss immersion tests in HBSS [84,85]. The primary degradation products are ZnO, Zn(OH)<sub>2</sub>, and calcium phosphates and carbonates. When Ag content is above 2.5 wt.%, localized pitting corrosion is observed, attributed to the galvanic effect between ηZn (cathode) and εAgZn<sub>3</sub> (anode). The oxide layer on the surface of the alloy is broken up by corrosion of εAgZn<sub>3</sub>, decreasing corrosion resistance.

#### 2.3.2.7 Effect of Strontium on Zinc

Strontium (Sr) is absorbed by the human body in a similar fashion to Ca; after consumption it attaches to the surface of bones, aiding bone growth and increasing bone density and strength [86]. Sr can be used as an alloying element in aluminum to improve ductility and strength, and as an inoculant in ductile iron castings. Additionally, Sr oxides and carbonates are frequent materials in glass and ceramic manufacturing [87]. There is limited to no solubility of Sr in Zn according to the Zn-Sr phase diagram, therefore low additions of Sr produce a two phase alloy consisting of a ηZn matrix with SrZn<sub>13</sub> precipitates [88].

Following hot rolling or extrusion, Li et al. [66] observed Zn-1Sr exhibited improved mechanical strength and ductility compared to pure Zn through precipitation strengthening of the ductile SrZn<sub>13</sub> phase, while Yang et al. [89] measured negligible strength differences at 0.1 and 0.4 wt.% Sr. Since the solubility of Sr in Zn is limited, Sr will be enriched in the liquid, thus restricting grain growth during solidification, promoting grain refinement and overall mechanical strengthening at a critical amount.

The *in vitro* corrosion rate from electrochemical and immersion tests of Zn alloys with low Sr concentration (1 wt.%) is slightly higher than that of pure Zn in HBSS [66,89]. A higher

corrosion rate suggests galvanic corrosion coupling between the Zn matrix and SrZn<sub>13</sub> precipitates. A uniform deposition of corrosion products containing Ca and P are formed on the alloy surface after two weeks, common with HBSS testing. After eight weeks of immersion, the mechanical integrity of the Zn-Sr alloy is only slightly declined compared to the fast degradation of Mg-based alloys.

### 2.3.3 Reported Mechanical and Corrosion Properties of Zinc Alloys

A multitude of binary and ternary Zn alloy systems involving the previously mentioned nontoxic alloying elements have been investigated thus far for BM applications. While the design focus for each alloy may be different (i.e. stent, implant, etc.), the physical and biological properties relating to the general design constraints (Table 1) are always measured in initial reports as they are easily comparable between alloys. Summarized below in Figures 5 - 7 are reported ranges of ultimate tensile strength, elongation to failure, and corrosion rate [6,7,12,45,66,80,84,90]. Variability for a given property within each alloy is attributed to processing conditions, microstructure, variation of alloying element concentration, and testing parameter choices.

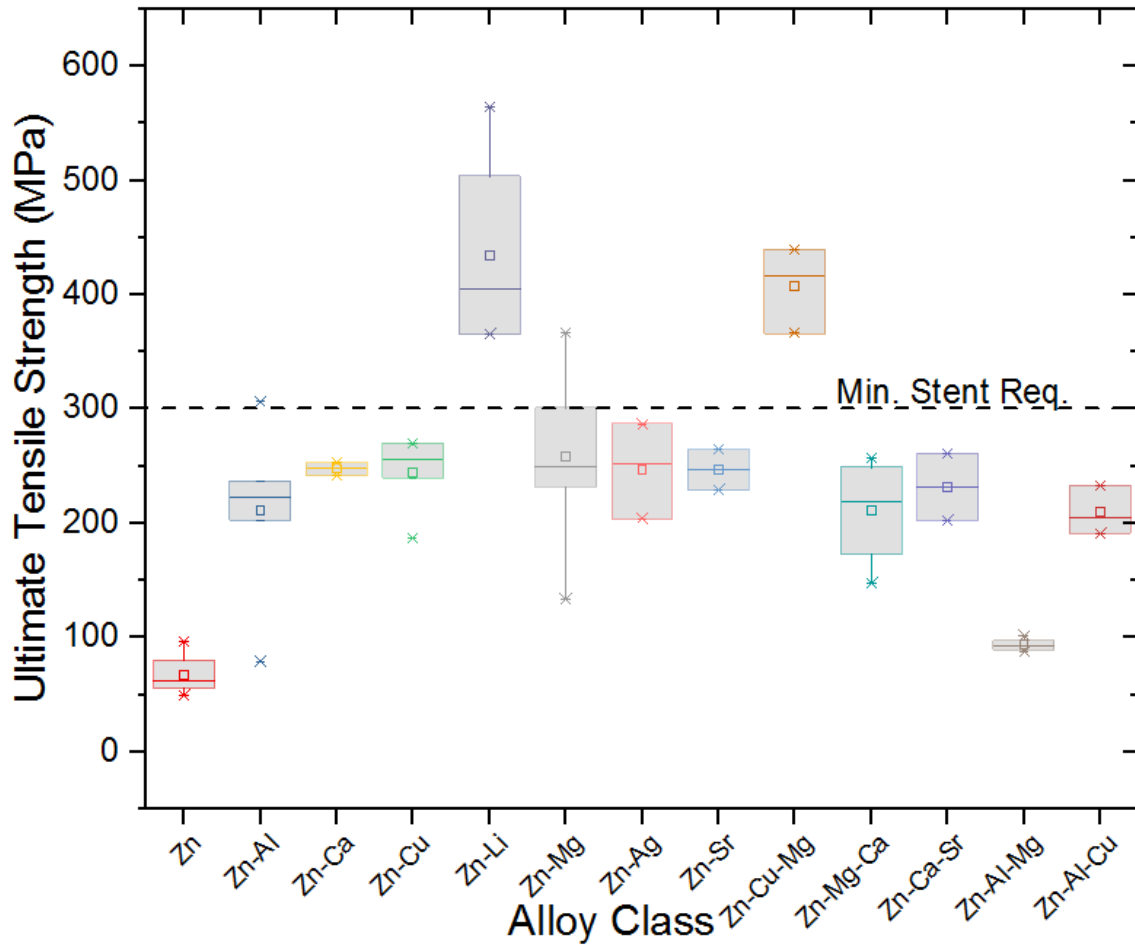


**Figure 5:** Comparison of UTS for reported hot-rolled and extruded biodegradable Zn alloy classes.

While pure Zn traditionally has a low tensile strength, alloying promotes the formation of stronger intermetallic phases, precipitation strengthening, and solid solution strengthening. Most Zn BM alloys do not meet the minimum stent requirement for ultimate tensile strength of 300 MPa thus far. Only Zn-Li, Zn-Mg, Zn-Al, and Zn-Cu-Mg systems has been reported to exceed 300 MPa, and no alloys have exceeded 600 MPa. Therefore, Li, Mg, Al, and Cu can be considered primary candidates for further optimization based on their promising ultimate tensile strengths.

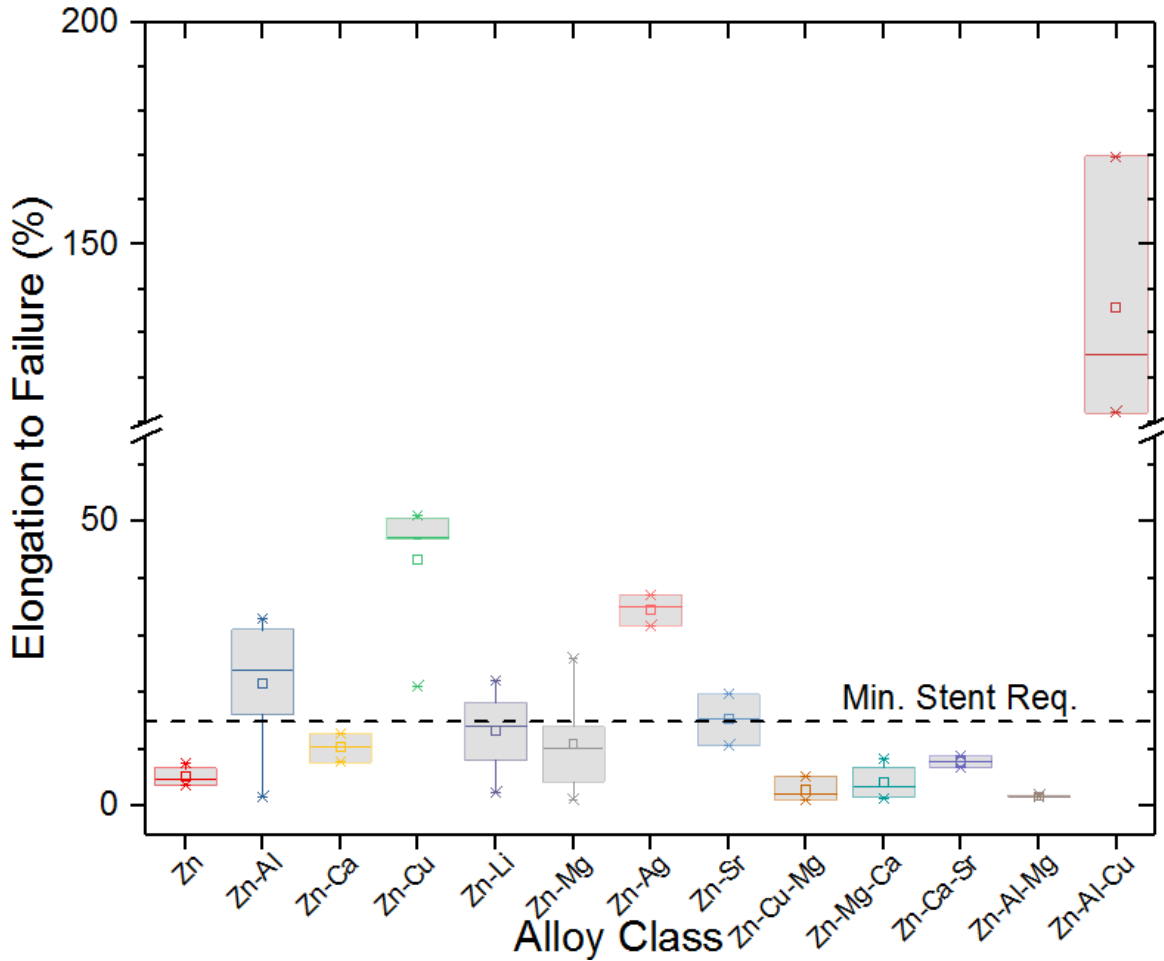


**Figure 6:** Comparison of elongation to failure for hot-rolled and extruded reported biodegradable Zn alloy classes.

Often tensile strength and ductility are inversely proportional to one another. Many Zn alloy systems exhibit this relationship and it is rare for an alloy to have both high ultimate tensile strength and elongation to failure. Optimizing the two mechanical properties by varying processing parameters and alloying elements is a primary focus of materials design for BM applications. Solely focused on elongation, Zn-Al, Zn-Cu, Zn-Mg, Zn-Ag, Zn-Sr, and Zn-Al-Cu systems have been reported to exceed the minimum design requirement for stents of 15% elongation to failure.

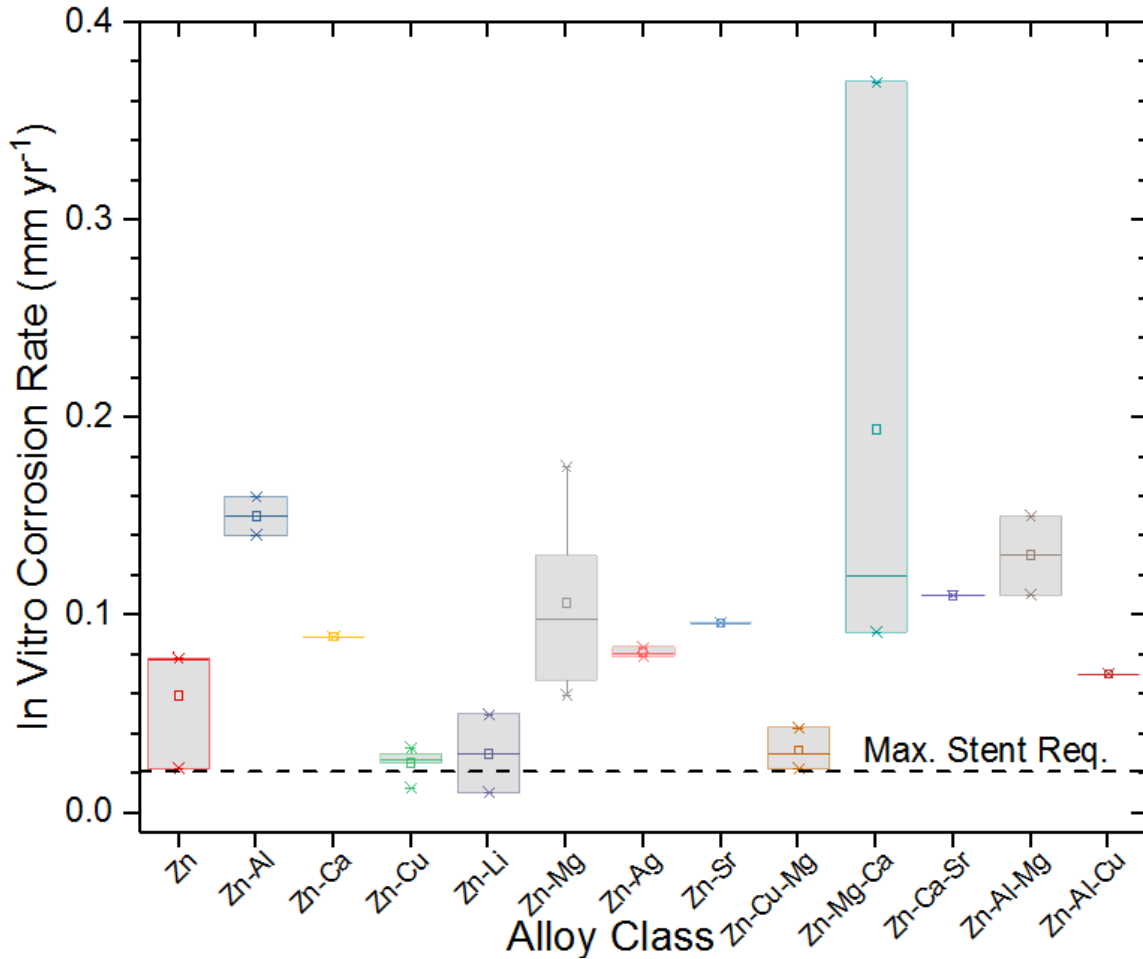


**Figure 7:** Comparison of *in vitro* immersion corrosion rate for reported Zn alloy classes. *In vitro* corrosion rate is primarily affected by the phases present and their reactivity in saline solutions, such as HBSS or SBF. The corrosion products and behavior of all Zn alloys classes are very similar to one another, primarily adjusted based on elemental and phase concentrations. The maximum recommended corrosion rate for stents is  $0.02 \text{ mm yr}^{-1}$  and is only met by pure Zn and some Zn-Cu, Zn-Li, and Zn-Cu-Mg alloys.

A key observation from the compilation of mechanical and corrosion data is that there is not an ideal Zn alloy that satisfies all design requirements as of yet. The most promising alloying elements are Cu, Li, and Mg. While Zn-Cu does not quite meet the UTS requirement, it far exceeds the minimum ductility constraint and has a compatible corrosion rate. Conversely, Zn-Li

just meets the minimum ductility, surpasses the minimum UTS requirement by a large margin, and also meets the corrosion rate constraint. While some Zn-Mg alloys have satisfactory strength and ductility, their corrosion rates are an order of magnitude too high and are very difficult to adjust due to the high reactivity of Mg. Optimizing a hypothetical Zn-Li-Cu ternary alloy could take advantage of the individual binary alloy benefits, while minimizing downsides and having a low corrosion rate. Thus far, a Zn-Li-Cu alloy has not been reported in literature for any application.

### 2.3.4 Metal Toxicity in the Human Body

While not all elements are considered essential to the human body, a normal amount of each is stored, used, or excreted regularly. While material selection and alloy design is guided by mechanical and biodegradation constraints, *in vivo* elemental toxicology is a critical property to consider. Both essential and nonessential elements can become harmful when ingested above certain daily intake limits. The biological role, toxicology, and daily allowance for the average human body of selected alloying elements for BM materials are summarized in Table 3.

**Table 3:** Summary of alloying element function and toxicology in the adult human body.

Element	Daily Upper Limit	Biological Role	Toxic Effects	Ref.
Zn	40 mg	Enzyme catalysis; protein and muscle growth; cell division.	Nausea; reduced copper and iron usage; impaired immune function.	[91]
Al	N/A	Nonessential metal; small amounts absorbed in body are excreted.	Neurotoxicity if injected; controversial evidence of causation to Alzheimer's disease.	[55]
Ca	2.5 g	Majority is stored in bone tissue; nerve signals; blood flow.	Constipation; increased risk of kidney stones; reduced absorption of iron and zinc.	[92]

Cu	10 mg	Enzyme cofactor; brain development; white blood cell formation.	Liver damage; gastrointestinal-based nausea.	[93]
Li	85 – 169 mg	Treatment of manic-depressive disorder.	Nausea; neurotoxicity; nephrogenic diabetes insipidus; reduced endocrine function.	[94,95]
Mg	670 – 770 mg	Muscle and nerve function; regulates blood sugar and pressure; factor toward DNA synthesis.	Nausea; cardiac issues.	[96]
Ag	N/A	Nonessential element; topical treatment of burns; endotracheal tube alloy.	Decreased blood pressure; stomach issues; liver and kidney damage; argyria; argyrosis.	[97]
Sr	0.2 mg	Used for metabolic studies; majority stored in bone tissue.	Can displace Ca in bone at high doses; treatment of osteoporosis.	[86,98]

Zinc has been known to be an essential element in the human body since 1961, when an Iranian male who subsisted on only bread, potatoes, and milk was discovered with anemia, hypogonadism, and dwarfism, symptoms of zinc deficiency [99]. Zn is essential toward many physiological functions, separated into catalytic, structural, and regulatory functions [100]. Due to the relatively high upper tolerance for human intake, as well as favorable mechanical properties mentioned earlier, the non-cytotoxic behavior of Zn and its alloys has been investigated in recent years. Li et al. [101] measured *in vitro* cytotoxicity of 100% extracts of pure Zn via the relative metabolic behavior of L929 fibroblasts in Dulbecco's modified Eagle's medium (DMEM) and Saos-2 osteoblasts in McCoy's 5A medium, finding that both tests were above 70% of the control, inferring non-cytotoxicity. Wang et al. [102] also investigated the potential cytotoxicity of pure Zn with umbilical vein endothelial cells in DMEM + 10% fetal bovine serum (FBS), observing non-cytotoxic behavior at 50% dilution. Good biocompatibility

of Zn is indicated by these published results and is good cause for further Zn alloy design and testing.

While Cu is known for its toxicity at high levels, it is an essential trace nutrient for humans and shows promise as a safe alloying element in Zn. It is a cofactor for redox enzymes, such as Ceruloplasmin, as well as a critical component for iron metabolism [67,103]. Zn-Cu binary alloys have been examined for cytotoxic behavior previously. Tang et al. [7] observed no *in vitro* cytotoxic behavior for 50% and 10% extracts of Zn-xCu alloys ( $x = 1 - 4$  wt.%) for EA.hy926 cells in DMEM + 10% FBS. Additionally, Zhou et al. [70] recently found no thrombosis, inflammatory response, or other cell damage effects during a 2 year *in vivo* implantation of a Zn-0.8Cu stent in porcine coronary arteries.

Oral ingestion of lithium is the standard treatment for bipolar disorder, and although the majority of patients report at least one minor, annoying side effect, they are generally associated with treatment nonadherence [104]. Zhao et al. [14] initially investigated Zn-Li binary alloys for stent, finding that Zn-0.1Li had satisfactory *in vivo* mechanical and corrosion behavior with only moderate inflammation and scar tissue formation. Yin et al. [105] further explored the excellent hemocompatibility of Zn-0.8Li, also confirming the potential of Li as an alloying element for BM applications.

Based on the average weight of stent devices and design criterion for product life, theoretical calculations can be completed to determine the maximum allowable mass percentage of a given element. The weight of a metal endovascular stent can vary with geometry and material from 0.15 – 0.24 g [106]. Given the conservative estimate of a 0.24 g stent with a short, 1 year lifetime and an ideal corrosion behavior, such as in Figure 4, in which all corrosion occurs

homogeneously during the last 6 months, only ~1.31 mg/day of material would be absorbed by the body. Based on Table 3, if the stent was entirely made of either Zn, Cu, or Li, the upper limit for elemental toxicity would not be reached. Therefore, an alloy comprised of a combination of these elements should have no detrimental toxic effects on the body.

## CHAPTER 3 – HYPOTHESIS AND RESEARCH OBJECTIVES

The primary objective of this study is to determine the feasibility of using Zn-Li-Cu alloys for developing, biodegradable medical device applications. Zn-alloys are a leading biodegradable material candidate due to their favorable mechanical stability and intermediate corrosion resistance. The current study focuses on the development and analysis of synthesis method, chemical and phase characterization, thermodynamic modeling, mechanical properties, corrosion behavior, and alloy substrate cytotoxicity.

Given the optimistic, available literature for the Zn, Zn-Li, and Zn-Cu systems, the proposed hypothesis for this study is: *A Zn-Li-Cu alloy exists that meets or exceeds all mechanical, biological, and degradation constraints for biomedical stent applications.*

The specific tasks of this research endeavor to validate the hypothesis are:

1. To select potential alloy chemistries within the Zn-Li-Cu ternary system for *in vivo* applications. The Zn-Li-Cu ternary phase diagram will be simulated and can be used as a predictor for thermodynamic favorability, phase fractions, and solid solution quantities.
2. To synthesize the selected alloys using melting, annealing, and hot-rolling methods. Samples will be characterized using ICP-OES, optical microscopy, SEM, EDS, and XRD in order to determine grain structure morphology, texture, phase equilibria, and element quantification.

3. To evaluate the mechanical stability of the studied alloys in ambient atmosphere through tensile and hardness testing methods. Mechanical properties such as ultimate tensile strength, yield strength, elongation to failure, Young's modulus, and Vickers hardness are determined for the alloys. Fracture surface micrographs can be used to analyze mechanical behavior during tension.
4. To simulate the degradation behavior of the alloys through *in vitro* immersion corrosion testing. Corrosion rate can be quantified based on weight loss after immersion, while corrosion resistance can be qualitatively measured using EIS. The degradation products will be characterized using SEM, EDS, FTIR, and XPS to determine compound identification and formation behavior.
5. To measure the *in vitro* cytotoxicity of selected Zn alloys in order to evaluate the ability for cellular and tissue growth on the alloy surface. Analysis of cell viability over 7 days and using 100 – 10% dilution of Zn extract will present evidence of any toxicity.

## CHAPTER 4 - EXPERIMENTAL METHOD

### 4.1 Melting and Annealing

Selected Zn-Li-Cu alloys were prepared from Zn shot (99.99 wt.%, Sigma-Aldrich), Li granules (99 wt.%, Sigma-Aldrich), and Cu powder (99.9 wt.%, Alfa Aesar). Raw materials were physically mixed before addition into the crucible to promote elemental homogenization. Melting was completed at approximately 700 °C in a graphite crucible under Ar atmosphere within a glovebox (2 – 3 mbar pressure, <0.1 ppm H<sub>2</sub>O, <1 ppm O<sub>2</sub>) to prevent unwanted oxidation, shown in Figure 8. The as-cast ingots were homogenized at 300 °C in Ar atmosphere for 15 h, followed by natural cooling to room temperature. The post-annealed ingots were approximately 10 mm in thickness.

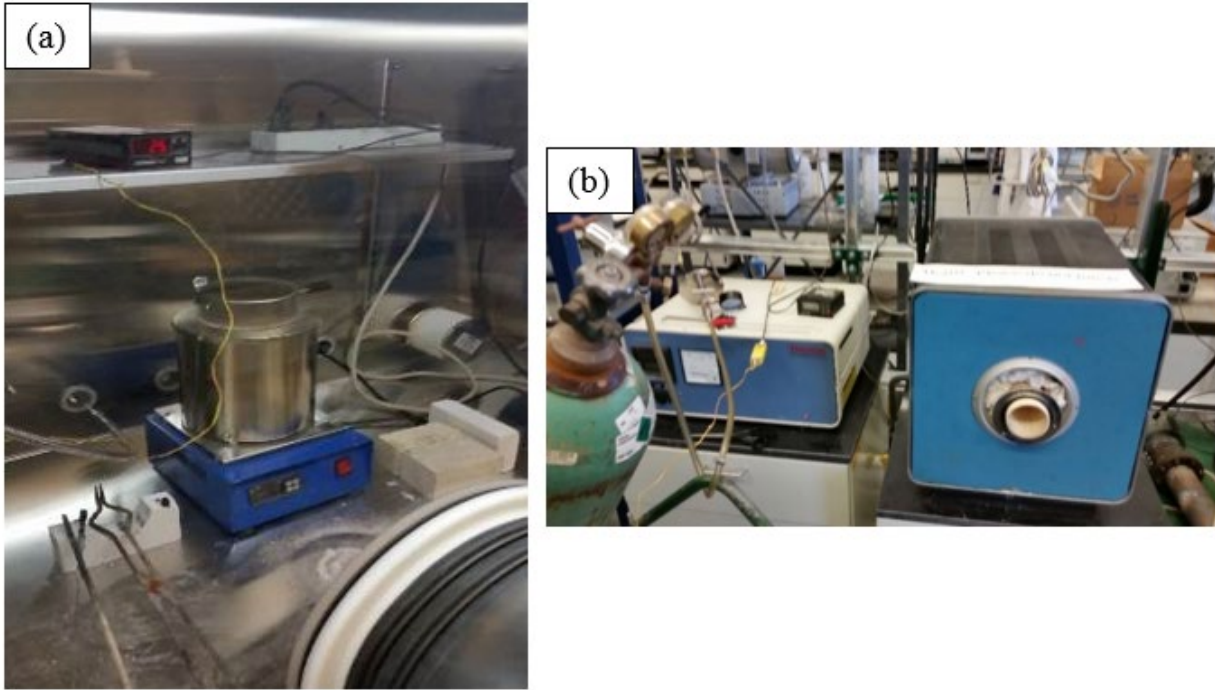


**Figure 8:** (a) Melting setup in inert atmosphere glovebox; (b) Annealing furnace with attached Ar gas line.

#### 4.2 Hot Rolling

To reduce the ingot thickness into a sheet geometry, hot rolling (Stanat TA-215) was utilized, presented in Figure 9. The as-cast ingots were initially soaked at 300 °C for 2 h in air, followed by alternating 0.3 mm thickness reductions and 5 min resoaking periods. The final reduction of each Zn-alloy sheet was approximately 80%, down to 1.5 – 2 mm.

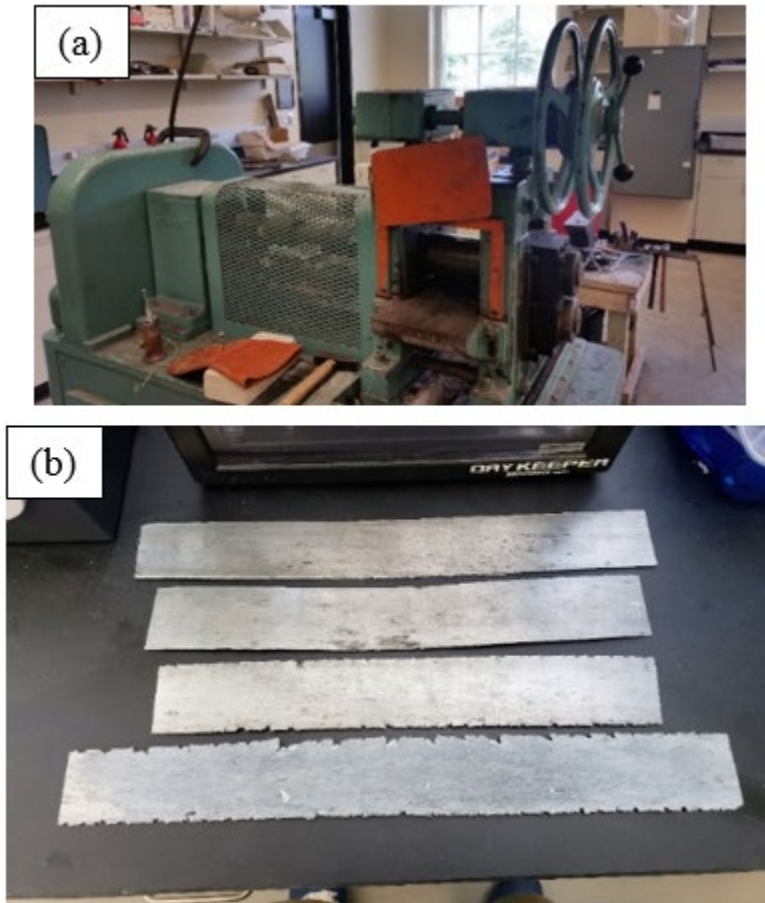


**Figure 9:** (a) Stanat hot rolling instrument; (b) Example hot-rolled metal sheets.

### 4.3 Characterization

Compositional analysis of the rolled sheets was completed using ICP-OES (Perkin Elmer Optima 4300 DV). Each sample solution comprised of approximately 30 mg of alloy dissolved in 20 ml of 35%  $\text{HNO}_3$ . The surface microstructure was observed using optical microscopy (Nikon Epiphot 200). Samples were ground with 240, 400, 600, 800, and 1200 grit SiC paper, polished with 1 and  $0.05 \mu\text{m}$   $\text{Al}_2\text{O}_3$  suspensions, and etched for 5 s with an acidic solution (100 ml distilled water, 10 g  $\text{CrO}_3$ , and 1.5 g  $\text{Na}_2\text{SO}_4$  [107]). Phase analysis was conducted using XRD (Bruker D8) with a Co  $K\alpha$  radiation source. Elemental composition of the alloys and

corrosion products was completed using SEM and EDS (JEOL 7000 & Apreo FE-SEM). Chemical compound analysis of the corrosion product was completed using FTIR (Perkin Elmer Spectrum 400) and XPS (Kratos Axis Ultra DLD, analytical chamber pressure  $10^{-10}$  torr, monochromatic Al K $\alpha$  X-ray source, binding energy calibrated with respect of the adventitious carbon C 1s peak at 284.8 eV).

#### 4.4 Immersion Corrosion Testing

*In vitro* immersion corrosion testing was carried out in HBSS (ThermoFisher #14025076), a human blood plasma simulant, at  $37 \pm 1$  °C according to NACE/ASTM TM1069/G31-12a [108]. A schematic of the immersion experiment is illustrated in Figure 10.

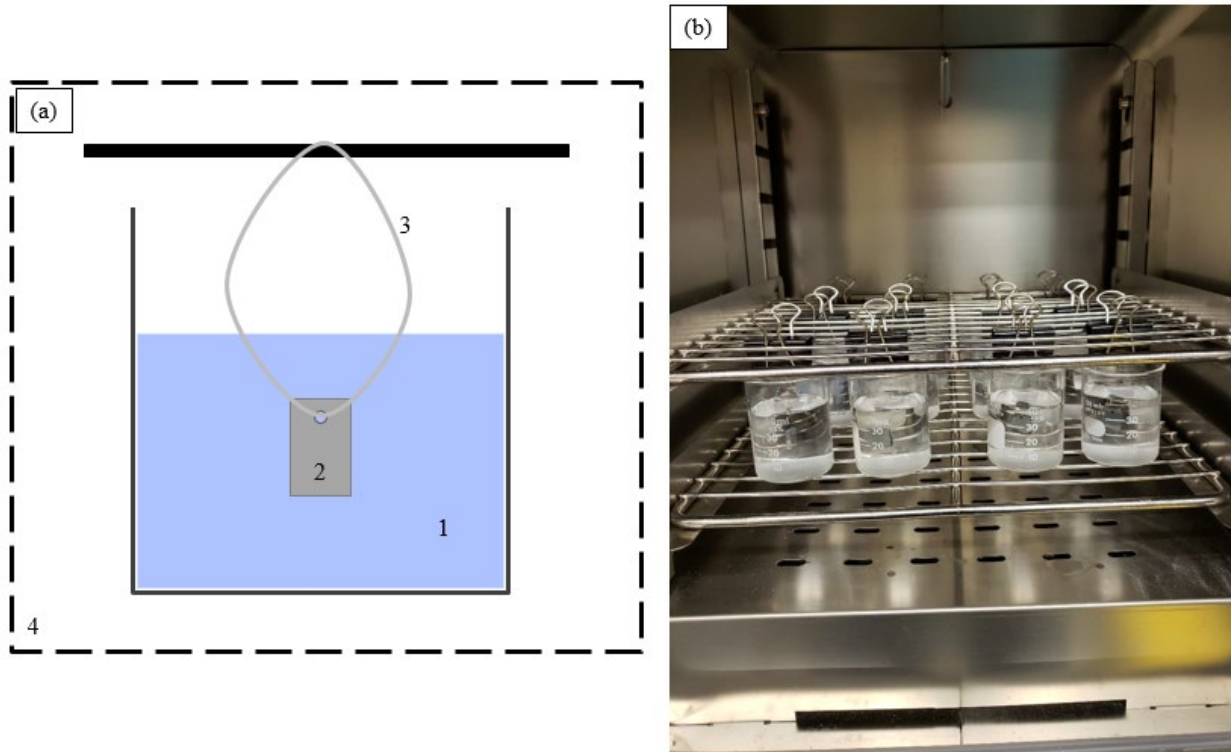


**Figure 10:** (a) Schematic of *in vitro* immersion corrosion experiment, where (1) HBSS, (2) hot-rolled alloy sample, (3) Nylon wire, (4) drying oven with air atmosphere; (b) Example long-term corrosion experiment setup.

The solution volume to sample surface area utilized was 20 ml/cm<sup>2</sup>. The samples were ground to 1200 grit using SiC paper and ultrasonically cleaned in acetone and distilled water for 5 minutes each. Each sample was suspended in HBSS using Nylon wire, which is virtually inert to saline water and does not react galvanically with metal. The HBSS was changed every 24 h to ensure a constant pH and solution chemistry throughout each experiment. After 5, 12, 21, 50, and 100 days, the samples were removed, rinsed with distilled water, and air dried. Corrosion product morphology was analyzed using SEM/EDS before and after water rinsing. The alloy corrosion surface was exposed using a CrO<sub>3</sub> solution for 2 – 3 s, followed by ultrasonic cleaning in distilled water for 2 min. The corrosion rate was calculated from the weight loss by Eq. 1:

$$CR = \frac{87.6 \cdot \Delta W}{A \cdot t \cdot \rho} \quad (1)$$

Where  $CR$  is the corrosion rate in mm yr<sup>-1</sup>,  $\Delta W$  is the weight change in mg,  $A$  is the surface area in cm<sup>2</sup>,  $t$  is immersion time in h, and  $\rho$  is sample density in g/cm<sup>3</sup>, and 87.6 is a unit proportionality factor [48].

#### 4.5 Electrochemical Impedance Spectroscopy Analysis

In order to assess the corrosion resistance associated with the corrosion product layer, EIS (Princeton Applied Research VersaSTAT 3) was completed. A two-electrode setup was used, where the reference and counter electrode was Pt foil and the working electrode was the Zn alloy sample. Nickel wire was used to connect the electrodes to the EIS instrument clamps. The test solution was HBSS at 37 °C and the distance between electrodes was 1 cm. Prior to each electrochemical test, a stable open circuit potential (OCP) was obtained after 30 min, followed

by EIS measurements at a frequency range from  $10^5$  to 1 Hz under 10 mV amplitude of perturbation signal at OCP.

#### 4.6 Cytotoxicity Assessment

The MTS test, through the indirect contact method according to ISO 19007:2018 [109], was utilized to evaluate the cytotoxicity of hot-rolled pure Zn, Zn-0.3Li-2Cu, Zn-0.3Li-3.5Cu, and Zn-0.3Li-5Cu. NIH3T3 fibroblast cell line was cultured in Dulbecco's Modified Eagle's Medium (DMEM) supplemented with 10% bovine calf serum and 1% penicillin streptomycin. Alloy extracts were prepared by adding media in the ratio of 1.25 cm<sup>2</sup>/1 ml media and incubated for 24 hr at 37 °C in a humidified 5% CO<sub>2</sub> atmosphere. After 24 hr, the media was collected and stored at 4 °C. Extract dilutions (10%, 50%, and 100%) were prepared by adding media to extract. Cells were added to a 96 well plate overnight to adhere. The cell media was removed the following day and 50 µl of extract dilutions were initially added and incubated, with an additional 50 µl added to the wells every two days. MTS assay was performed after 1, 4, and 7 days per ISO standard. Alloy extract dilutions were replaced with 100 µl of media and 20 µl of cell Titer 96<sup>®</sup> solution was added and incubated for 2 hr. Absorbance reading was then measured at 490 nm using a multimode microplate reader (FilterMax F5, Molecular Devices). Images of the cells were captured using an Olympus IX83 microscope with a spinning disc. Cell viability was determined according to the following equation:

$$Viability (\%) = [Absorbance\ of\ sample / Absorbance\ of\ control] \cdot 100\% \quad (2)$$

## 4.7 Mechanical Testing

Tensile testing (Instron 5581) was completed using a 50 kN load cell according to ASTM E8/E8M-16a [110], shown in Figure 11.



**Figure 11:** Tensile testing setup of Zn alloy dogbone-shaped sample with extensometer attached. Subsize dogbone-shaped specimens, shown in Figure 12, were prepared from the hot-rolled sheets using waterjet cutting. The average sample thickness for all alloys was  $1.508 \pm 0.055$  mm. An initial strain rate of  $10^{-3} \text{ s}^{-1}$  was utilized during each test.

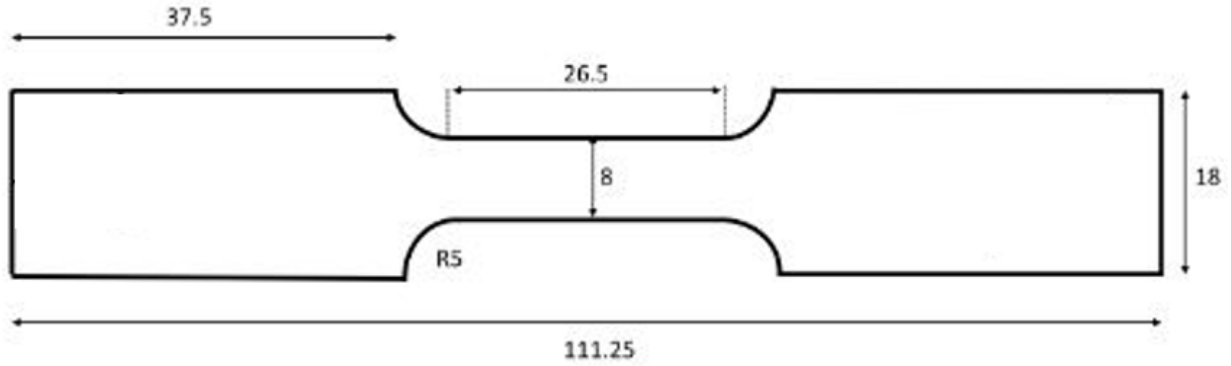


**Figure 12:** Tensile test sample dimensions; all measurements in mm.

Vickers hardness testing (Buehler 1600-6100) was completed per ASTM E384 [111] using 200 gf and 10 s load duration with 15 indentations per alloy sample. Samples were ground with 240, 400, 600, 800, and 1200 grit SiC paper and polished with 1 and 0.05  $\mu\text{m}$   $\text{Al}_2\text{O}_3$  suspensions to ensure a smooth surface for clean indentations. Vickers hardness was calculated by:

$$HV = \frac{1.8544 \cdot P}{d_1 \cdot d_2} \quad (3)$$

Where  $HV$  is in  $\text{kg}/\text{mm}^2$ ,  $P$  is the applied force which is 0.2 kgf,  $d_1$  and  $d_2$  are diagonal indentation lengths in mm, and 1.8544 is a geometrical factor due to pyramid shape of indenter.

## CHAPTER 5 – RESULTS AND DISCUSSION

### 5.1 Alloy Characterization

#### 5.1.1 Chemical and Phase Analysis

Nominal alloy compositions using Li and Cu were chosen during materials selection based on positive attributes of Zn-Li and Zn-Cu binary alloys reported in literature. Lithium was found to greatly increase mechanical strength and slightly heighten ductility up to approximately 0.35 wt.% in Zn, followed by sudden loss in ductility with further additions of Li [12]. For this study, 0.3 wt.% Li was chosen to maximize the strengthening behavior while leaving a safety factor for small variances in composition so >0.35 wt.% Li was not observed locally. Copper was reported to significantly enhance the elongation to failure up to 4 wt.% with minor benefits to tensile strength. Since there was not a change in trend in mechanical properties in Zn-Cu binary alloys up to 4 wt.% Cu, values of 2, 3.5, and 5 wt.% were chosen for this study to investigate the effect of Cu in the ternary alloy. Ideally, alloying effects of Li and Cu should be cooperative, where Zn-Li phases enhance strength and Zn-Cu phases enhance ductility simultaneously. No phase interactions, detrimental or otherwise, between Li and Cu are expected. Compositions of pure Zn, Zn-0.3Li, and Zn-3.5Cu were chosen as comparable control samples to identify processing and experimental differences to previously reported literature. The chemical composition of the Zn-based alloy samples was characterized using ICP-OES to compare the actual alloy chemistry to the nominal compositions, listed in Table 4.

**Table 4:** Nominal and experimental alloy compositions from ICP-OES.

<b>Alloy (nominal)</b>	<b>Li (wt.%)</b>	<b>Cu (wt.%)</b>	<b>Zn (wt.%)</b>
Zn	0	0	100
Zn-0.3Li	0.31 ± 0.01	0	99.69 ± 0.01
Zn-3.5Cu	0	3.34 ± 0.26	96.66 ± 0.26
Zn-0.3Li-2Cu	0.35 ± 0.02	1.85 ± 0.21	97.8 ± 0.23
Zn-0.3Li-3.5Cu	0.28 ± 0.02	3.53 ± 0.14	96.19 ± 0.16
Zn-0.3Li-5Cu	0.27 ± 0.02	5.07 ± 0.21	94.66 ± 0.23

Small variations from the nominal compositions are attributed to higher vapor pressures of Zn and Li compared to the low Ar atmospheric pressure within the glovebox during melting, illustrated in Figure 13. When a liquid substance has a higher vapor pressure than the surrounding atmosphere, the liquid will evaporate, such as water boiling at 100°C in air. Additionally, during the latter stages of melting, white Zn vapor visibly came off the melt surface as evidence of the melt loss. Small mass losses also occurred from metal sticking to the crucible wall during pouring. Since cooling will start at the melt/crucible interface and progress toward the center of the liquid metal mass, the metal at the bottom can solidify before the entire melt is poured. After each pour, minor amounts of leftover metal and slag were present at the bottom of the crucible. While additional superheat during melting could prevent leftover metal in the crucible, evaporation of Zn would accelerate due to the increased vapor pressure differential. Trace impurities from the raw materials, such as Fe, Mg, Ni, and Ca, were also observed in the final alloy at < 0.01 wt.% from ICP-OES analysis.

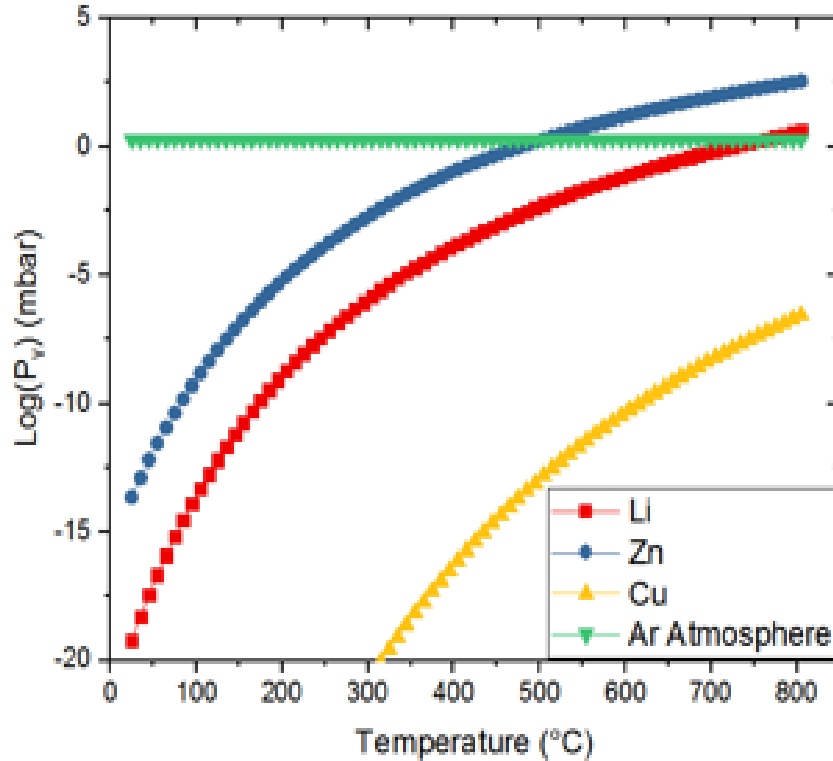


**Figure 13:** Theoretical vapor pressures of Li, Zn, and Cu compared to Ar atmosphere vs. temperature [112].

XRD studies were completed to determine the phases present in each alloy after hot-rolling, presented in Figure 14. Primary  $\eta$ Zn phase peaks are present in all samples. Additions of Li and Cu promote a multiphase structure, where peaks corresponding to  $\alpha/\beta$ LiZn<sub>4</sub> and  $\epsilon$ CuZn<sub>5</sub> secondary phases are present. These peaks overlap with one another at many angles due to a similar crystal structure, therefore accurate Rietveld analysis is difficult. Peak broadening is observed at these overlap angles (e.g. (100) peak at 48°). No binary or ternary phases containing both Li and Cu are observed. Reduction of the (002) Zn peak at 42° and heightening of the (101) peak at 50° highlights a change in texture due to influence of binary phases during hot rolling.

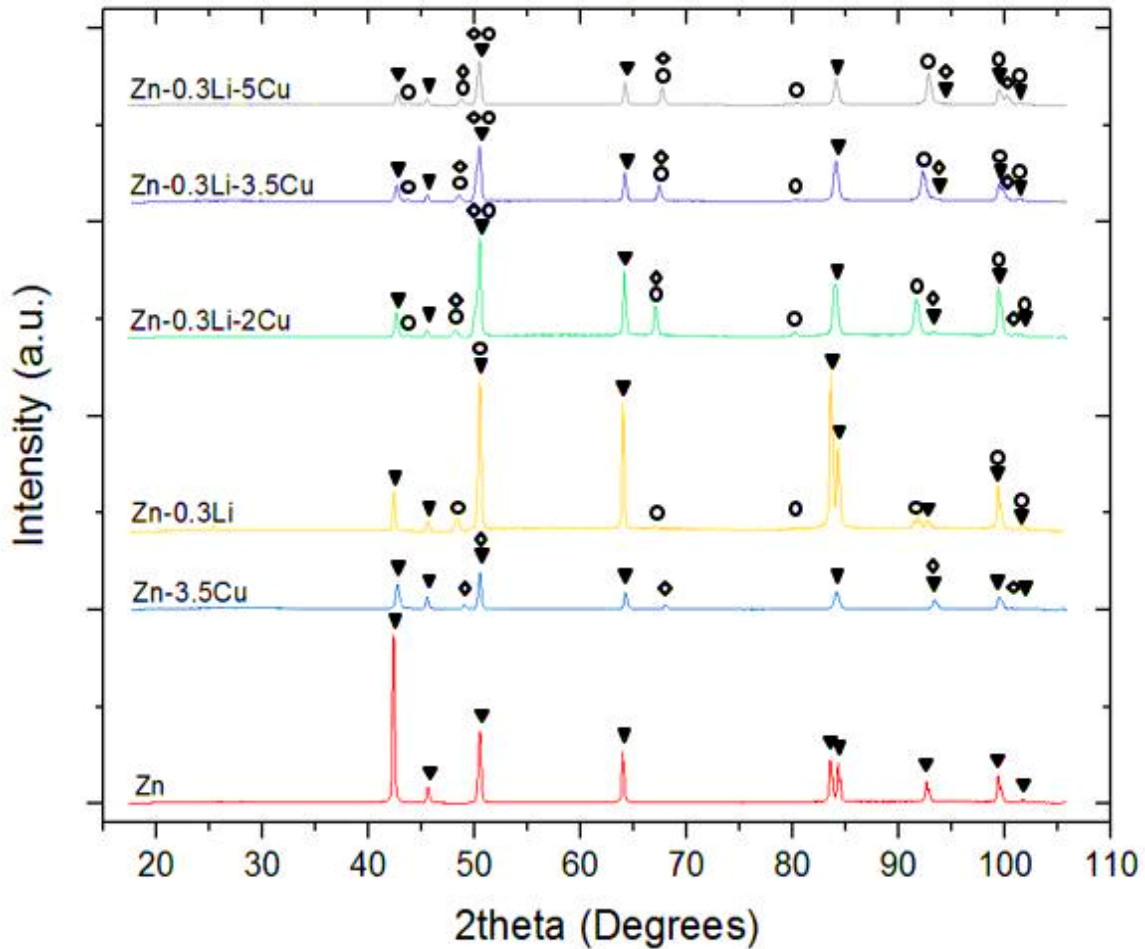


**Figure 14:** XRD patterns of hot-rolled Zn-based alloys, where ▼ = Zn, ○ =  $\alpha\text{LiZn}_4$ , and ◇ =  $\epsilon\text{CuZn}_5$ .

### 5.1.2 Optical Microscopy

Optical micrographs parallel to the hot-rolling direction of alloy sheets are shown in Figure 15. Pure Zn consists of larger, equiaxed grains, while the multiphase alloys are more elongated in the rolling direction, evidence of a texture change. Zn-0.3Li presents irregularly-shaped dendritic sections of  $\alpha\text{LiZn}_4$  (pinkish-white regions), approximately 22.7%, surrounded by a fine  $\eta\text{Zn}$  matrix. For Zn-3.5Cu, the white sections correspond to  $\epsilon\text{CuZn}_5$ , with an area fraction, estimated using imaging software, of approximately 27.5%. Additions of both Li and Cu in Figure 15d-f promote the formation of both  $\text{CuZn}_5$  and  $\text{LiZn}_4$  surrounded by a Zn matrix,

where both intermetallic phases are etched as darker regions. Since both intermetallic phases etch similarly, distinguishing between  $\text{CuZn}_5$  and  $\text{LiZn}_4$  in the same sample is difficult with optical microscopy. As Cu content increases from 2-5 wt.%, the  $\text{CuZn}_5 + \text{LiZn}_4$  combined phase fraction increases to 33.4%, 39.4%, and 44.8%, respectively. These phase fractions measured by volume and contrast difference compare well with theoretical phase percentages (Table 7, section 5.3.1) from the Zn-Li-Cu phase diagram. Additionally, the intermetallic phases become more elongated and interconnected as Cu content increases.

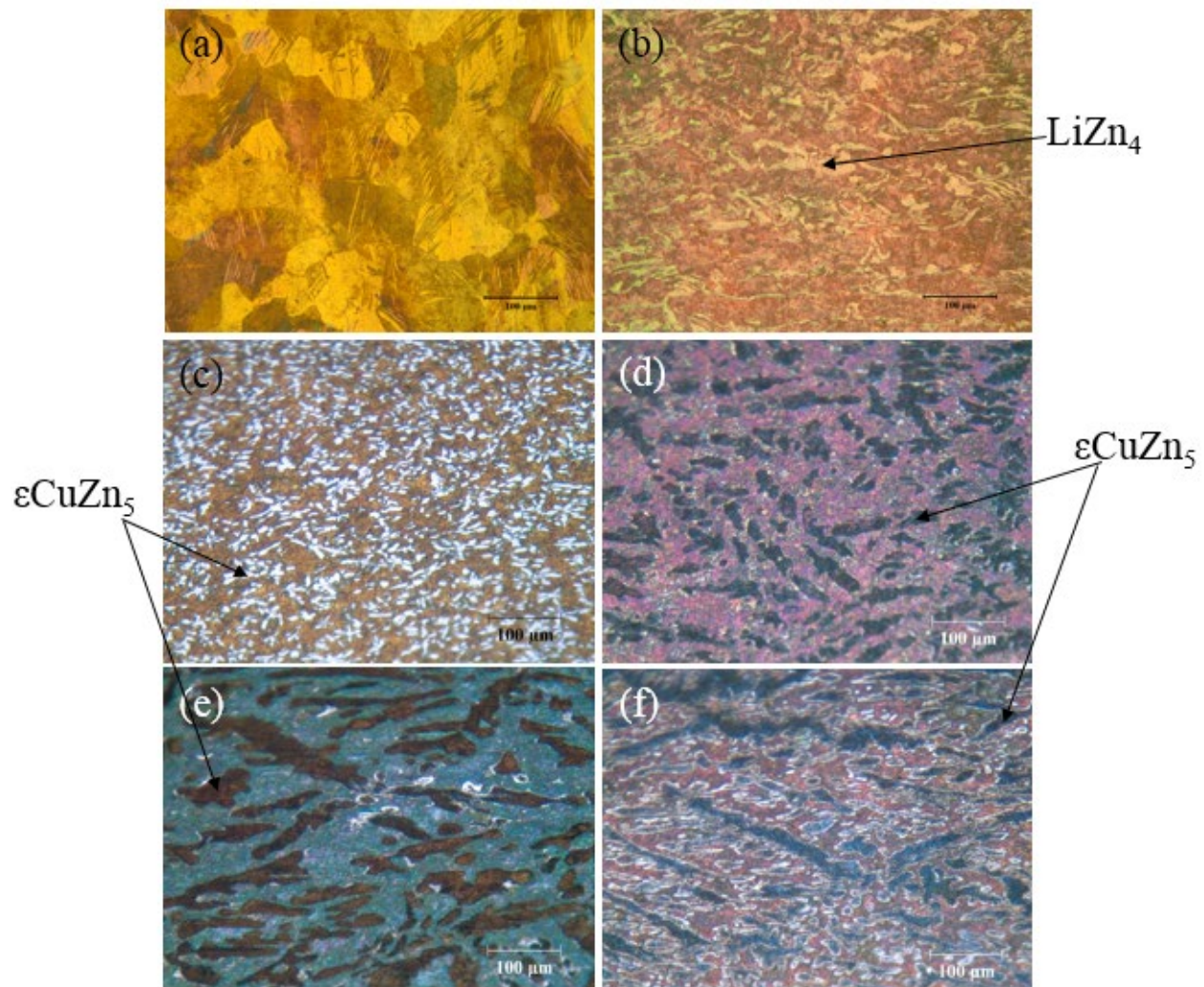


**Figure 15:** Optical micrographs of hot-rolled (a) Zn, (b) Zn-0.3Li, (c) Zn-3.5Cu, (d) Zn-0.3Li-2Cu, (e) Zn-0.3Li-3.5Cu, and (f) Zn-0.3Li-5Cu.

### 5.1.3 Phase Diagram Modelling

Phase diagrams are a common tool used in order to predict the phase fractions at a given composition and temperature. In addition to the XRD and optical characterization methods, a CALPHAD approach to phase diagram modelling was utilized to generate the previously unreported ternary Zn-Li-Cu phase diagram. Reported thermodynamic data for the Li-Zn [72], Cu-Li [113], and Cu-Zn [114,115] binary systems was compiled into a single data set to be used in PANDAT modelling software for this study. No ternary phases involving Zn, Li, and Cu are mentioned in thermodynamic literature nor in the ICDD crystallographic database. The full TDB (thermodynamic database) file is provided in Appendix II. The three binary phase diagrams were generated in PANDAT and compared well to their corresponding literature sources, shown in Figures 16 – 18.

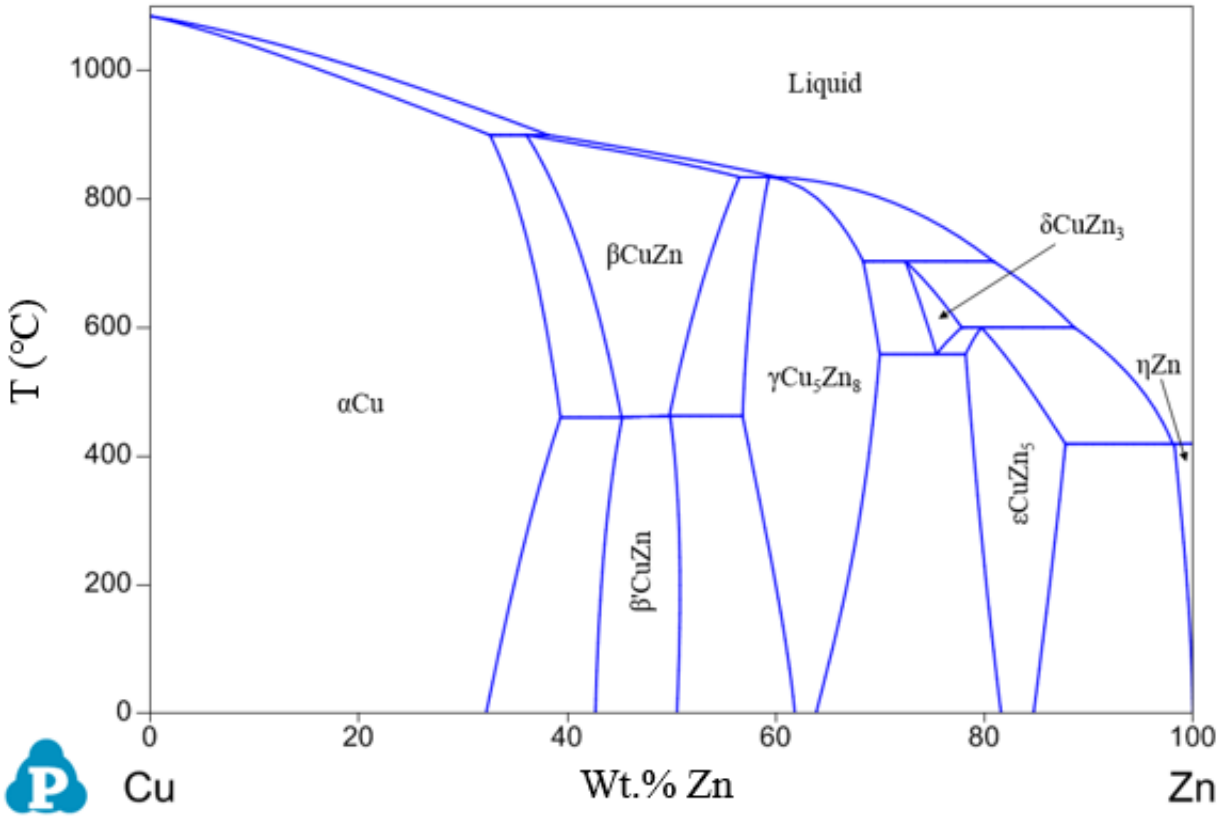


**Figure 16:** Binary phase diagram of Cu-Zn modeled in PANDAT using a CALPHAD approach.

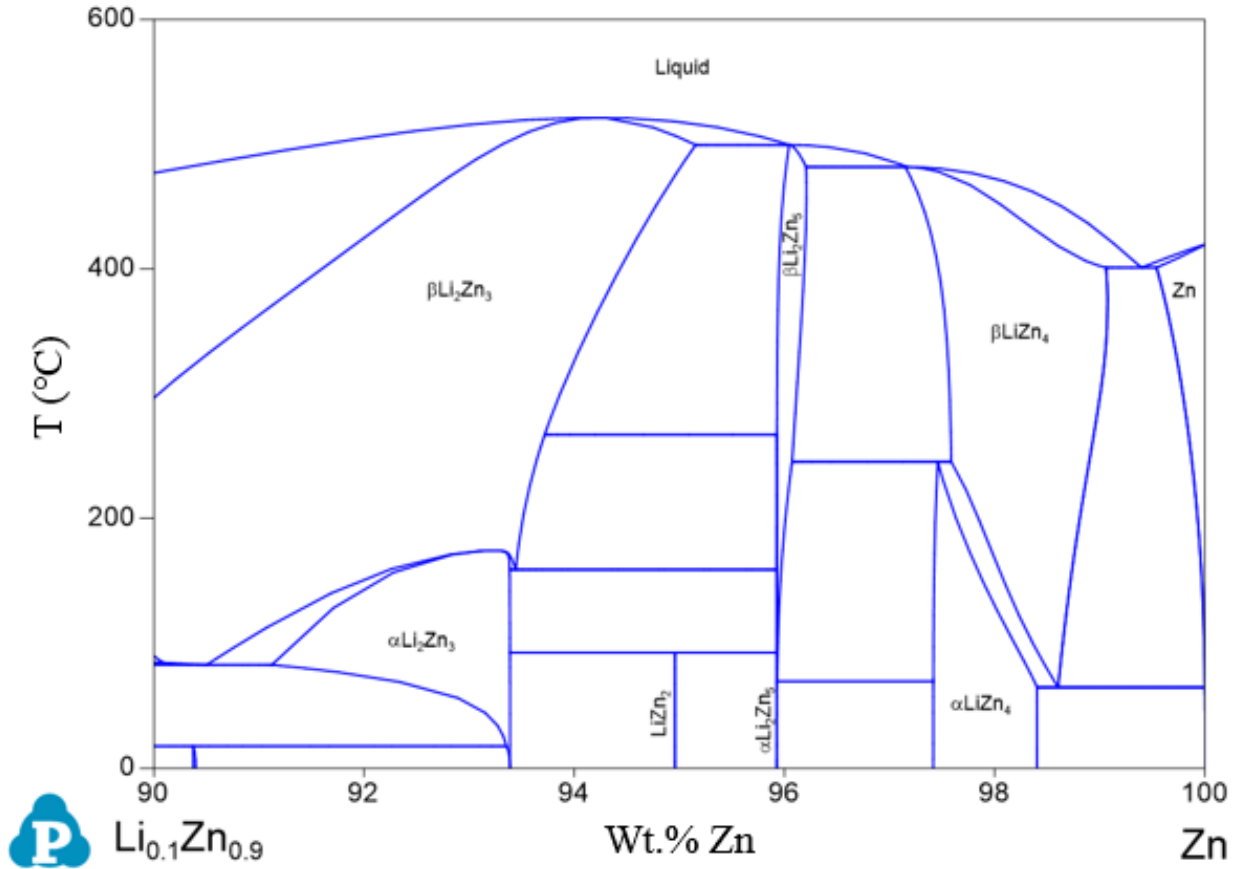


**Figure 17:** Abbreviated binary phase diagram of Li-Zn modeled in PANDAT using a CALPHAD approach.

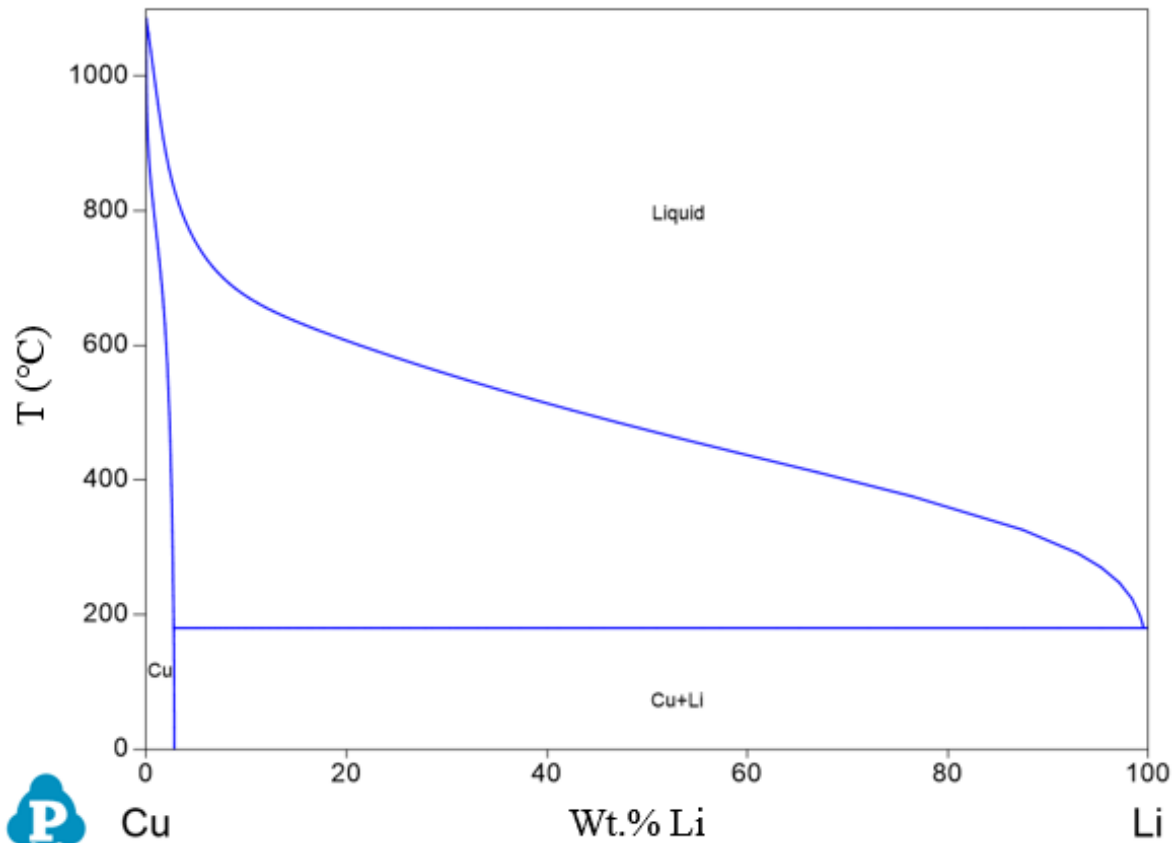


**Figure 18:** Binary phase diagram of Cu-Li modeled in PANDAT using a CALPHAD approach. Given the good accuracy of the modeled binary phase diagrams, the Zn-Li-Cu ternary phase diagram was generated using the reported thermodynamic data. The section of the ternary phase diagram relevant to this study is presented in Figure 19. The red star labels correspond to the selected alloy chemistries of this study. At 37 °C and 1 atm pressure, this diagram illustrates the equilibrium composition of the selected chemistries at approximate working conditions inside the human body. The expected equilibrium phases present according to the ternary phase diagram are  $\eta\text{Zn}$ ,  $\alpha\text{LiZn}_4$ , and  $\varepsilon\text{CuZn}_5$ , comparing completely with XRD analysis in Figure 14.

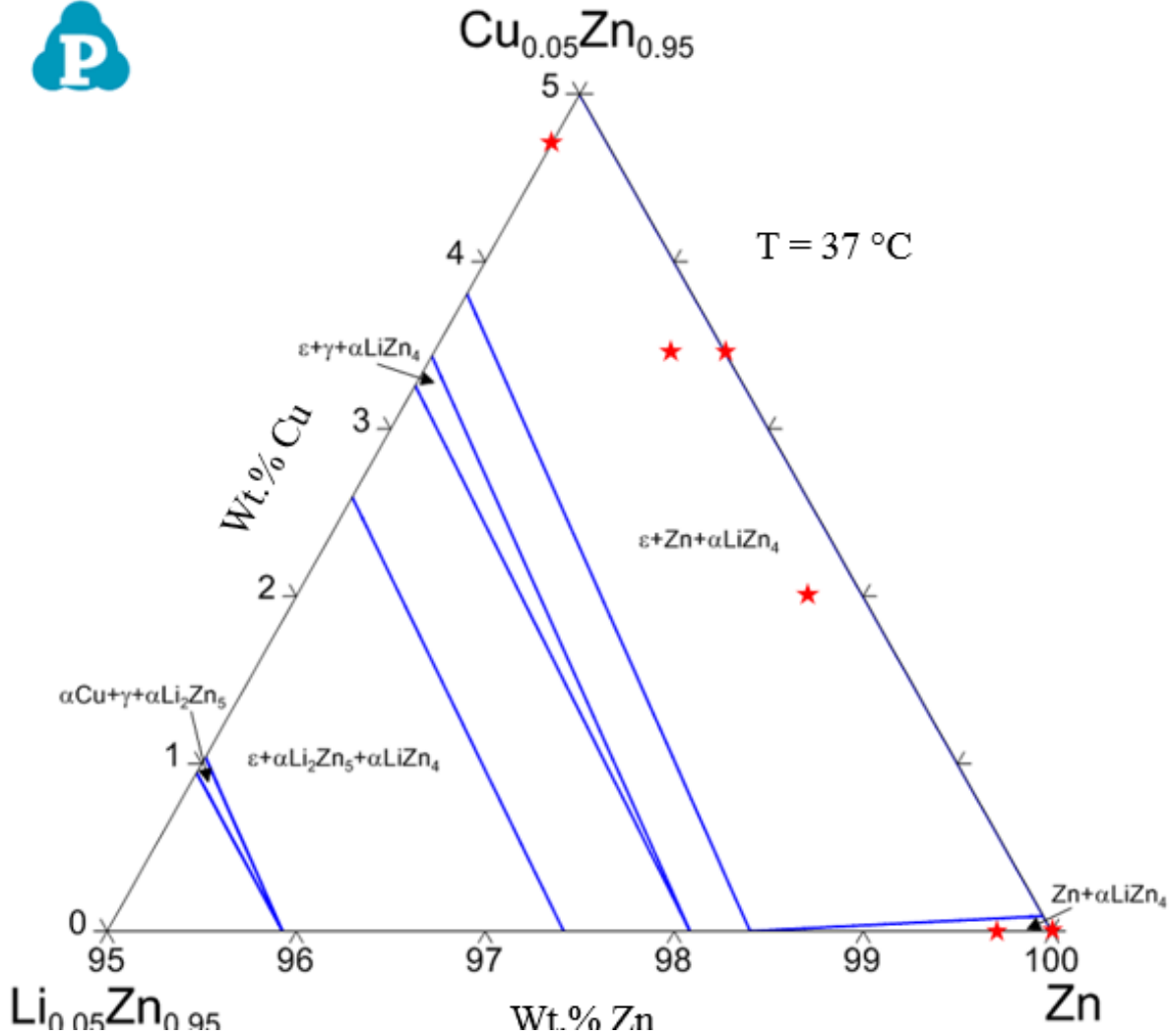


**Figure 19:** Abbreviated ternary Zn-Li-Cu phase diagram modeled with PANDAT using a CALPHAD approach. Studied chemistries are marked with red stars.

Phase projection of each alloy composition can be modeled using the thermodynamic data in order to assist towards identifying proper annealing and hot-rolling temperatures. An example phase projection diagram is shown in Figure 20, illustrating the phase fractions of Zn-0.3Li-3.5Cu. At  $>500\text{ }^{\circ}\text{C}$ , the metal is entirely liquid. The metal was poured at approximately  $700\text{ }^{\circ}\text{C}$  in order to have sufficient superheating to pour the entire mass before solidification. The phase fraction at ambient temperature is the equilibrium phase composition assuming sufficient time for complete atom mobility.

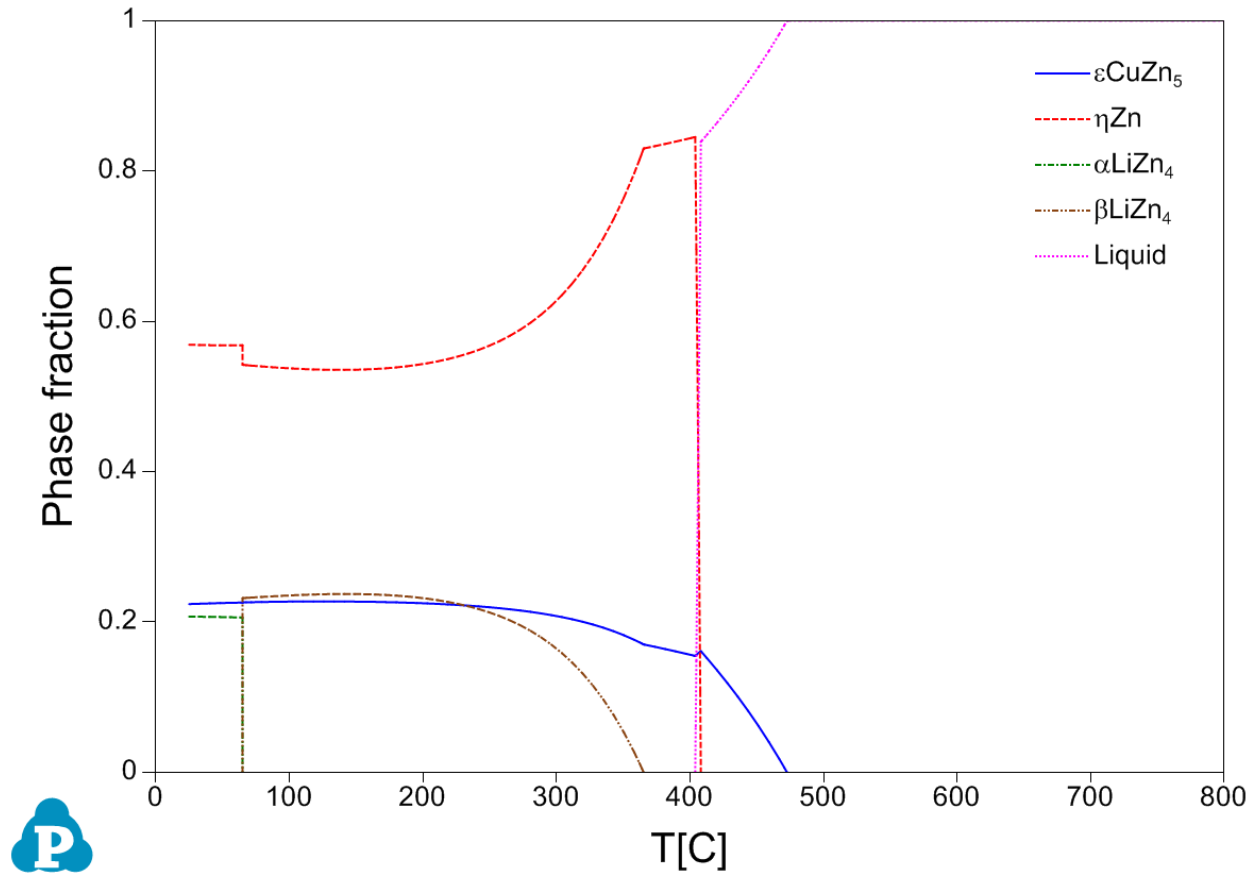


**Figure 20:** Solidification diagram of Zn-0.3Li-3.5Cu.

A Gulliver-Scheil solidification diagram can be used to calculate the fraction solid ( $f_s$ ) and liquid with respect to temperature. The Gulliver-Scheil approach follows three basic rules: 1) local equilibrium at the solid-liquid interface; 2) liquid atomic homogeneity; 3) zero atomic diffusion in solid phases [116]. Insight into the cooling behavior using these rules in conjunction with the phase equilibrium diagram can be gained in order to better optimize process parameters. As an example, the Gulliver-Scheil diagram for Zn-0.3Li-3.5Cu is shown in Figure 21.

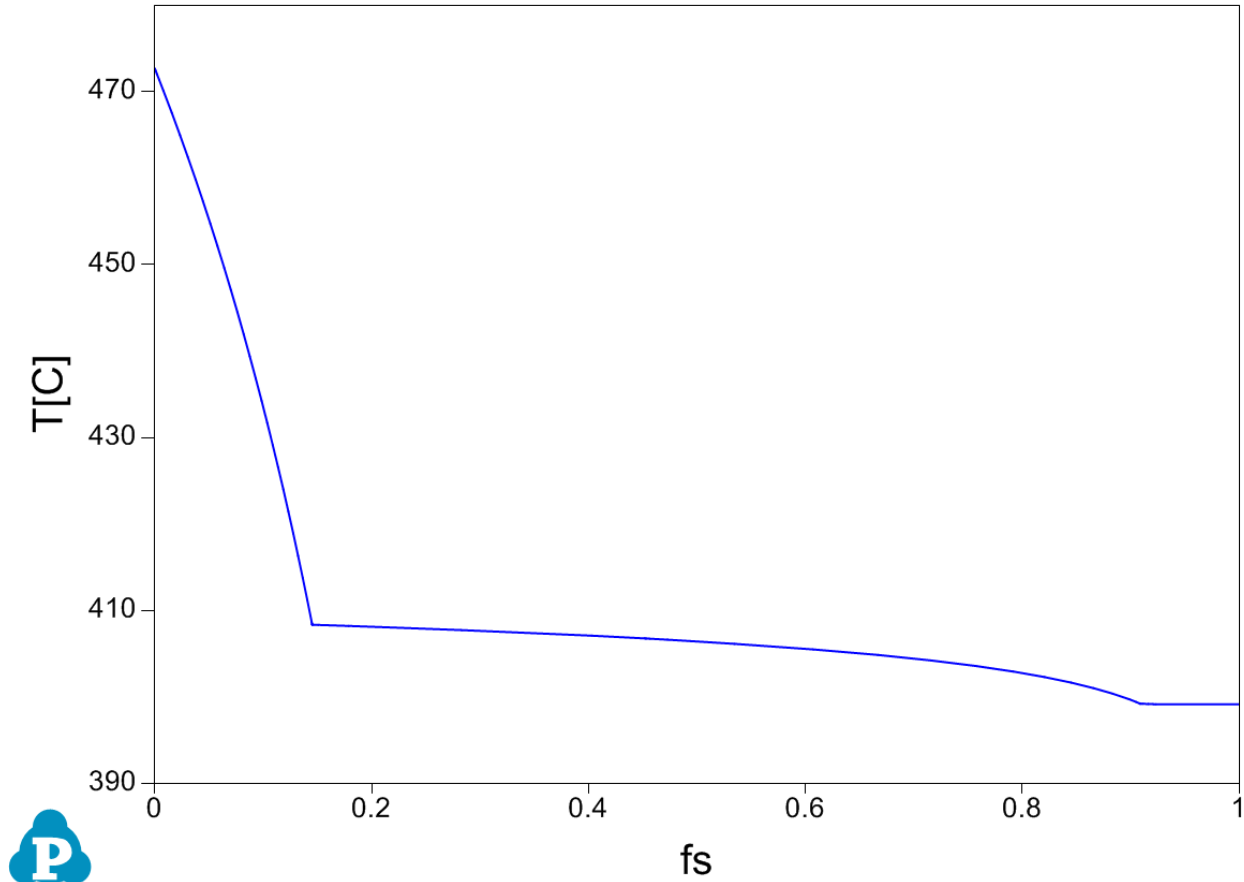


**Figure 21:** Gulliver-Scheil solidification diagram for Zn-0.3Li-3.5Cu.

The phase projection diagram predicts the equilibrium composition given sufficient time and energy for complete phase and atomic arrangement. For Zn-0.3Li-3.5Cu at 25 °C, the equilibrium composition is 56.9%  $\eta$ Zn, 20.7%  $\alpha$ LiZn<sub>4</sub>, and 22.4%  $\epsilon$ CuZn<sub>5</sub>. From a practical viewpoint of the cooling behavior, the entirety of the alloy is solid at approximately 400 °C, before any LiZn<sub>4</sub> has formed. Since solidification only takes 5 – 10 s after pouring, total atom mobility is low while the ingot solidifies in the mold and one can assume zero LiZn<sub>4</sub> actually forms as there is not sufficient time or energy to reach the equilibrium state. Phase prediction at 375 °C, a temperature between full solidification and nucleation of LiZn<sub>4</sub>, suggests the entirety of the Li content is in solid solution with  $\eta$ Zn. The Zn-Li phase diagram confirms that the solid solubility limit of Li in Zn increases with higher temperatures. Therefore, annealing is required

to provide the necessary time and energy for  $\text{LiZn}_4$  to precipitate from the supersaturated and metastable  $\eta\text{Zn-Li}$  phase.

An annealing temperature of 300 °C was chosen due to the phase fraction similarities to room temperature while still allowing for sufficient atom mobility for homogenization. While annealing between 300 – 400 °C is possible without liquid forming, the equilibrium phase fraction of  $\text{LiZn}_4$  decreases with temperature. A temperature of 300 °C was similarly chosen for hot-rolling due to phase fraction similarities to room temperature. Additionally, optimizing the hot-rolling process was of an iterative nature and processing temperatures below 300 °C were found to promote physical defects that would be detrimental to mechanical properties (e.g. cracking). While the phase fractions of each alloy differ in magnitude, the general trend of the solidification behavior for all alloys is similar to the example of Zn-0.3Li-3.5Cu. Therefore, the same processing parameters were utilized for all alloys for ease of comparability during mechanical testing.

## 5.2 Corrosion Testing

### 5.2.1 *In vitro* Immersion Corrosion Analysis

Immersion corrosion testing was completed to determine the degradation behavior and *in vitro* corrosion rate of the selected Zn-based alloys. The representative corrosion morphology of the alloys after *in vitro* immersion corrosion in HBSS is shown in Figure 22. A compact, large-grained corrosion product layer is formed on the surface of each alloy after only 5 days of immersion time. The morphology of the corrosion product is consistent regardless of the alloy composition. The plate boundaries of the product layer exist as cracks throughout the entire layer that extend to the alloy surface. Due to air drying for microscopy preparation, the plate cracks are

enlarged in some areas from dehydration of absorbed water. Example evidence of this can be observed in Figure 22b, where a white agglomeration is split cleanly in half after separation of the plate crack. These agglomerations of white nanoparticles are also observed precipitating on the entirety of product layer surface. The quantity of nanoparticle agglomerations increases with immersion time, implying continued deposition.

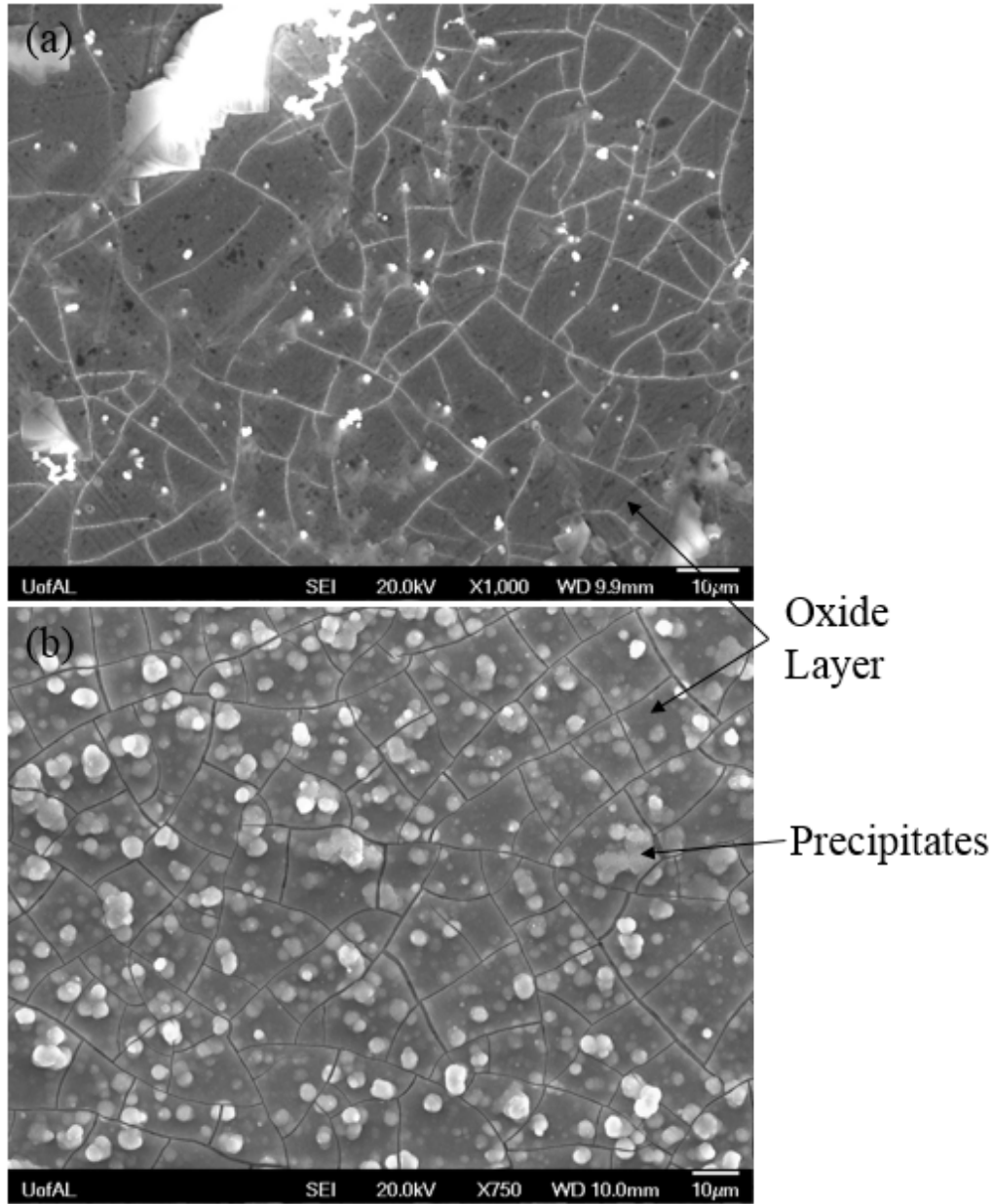


**Figure 22:** Representative morphologies of the corrosion products from Zn alloys after (a) 5 days and (b) 21 days.

EDS analysis in Figure 23 shows that the plated layer is primarily composed of Zn and O, while the white agglomerations contain Zn, O, P, Ca, C, Na, and Cl. Possible compounds the corrosion products comprise of are ZnO, Zn(OH)<sub>2</sub>, Zn<sub>3</sub>(PO<sub>4</sub>)<sub>2</sub>, Ca<sub>3</sub>(PO<sub>4</sub>)<sub>2</sub>, ZnCO<sub>3</sub>, and NaCl [79,117–119]. Similar corrosion product morphologies have been observed by Vojtěch et al. [117] for AZ91HP and Zn-1.5Mg alloys, as well as Xiao et al. [120] for Zn-0.05Mg, both in simulated body fluid solution.

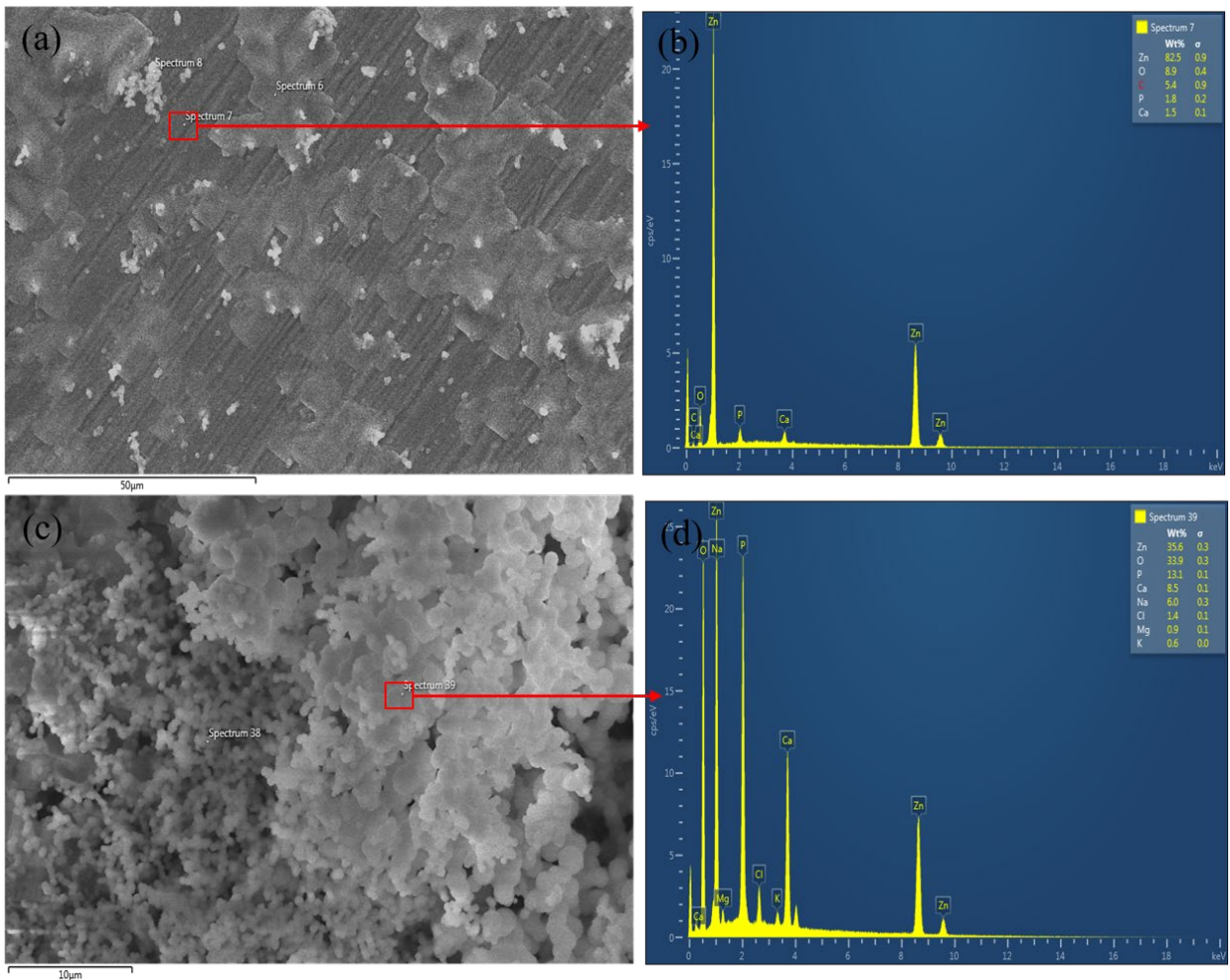


**Figure 23:** (a) SEM micrograph of 5-day corrosion of Zn; (b) EDS of oxide layer; (c) SEM micrograph of corrosion precipitate agglomerate after 21 days; (d) EDS of agglomerate.

The corrosion agglomerates were further characterized using FTIR, shown in Figure 24. The PO<sub>4</sub><sup>3-</sup> peaks can be observed at 1000-1180 cm<sup>-1</sup> and 600 cm<sup>-1</sup>, corresponding to symmetric and

antisymmetric stretching of various groups [121,122]. A series of bands in the range 1390-1500  $\text{cm}^{-1}$  and 1540-1620  $\text{cm}^{-1}$  represents the apatitic substitution of the  $\nu_3$  group of  $\text{CO}_3^{2-}$  [12]. A minor peak at 870-880  $\text{cm}^{-1}$  is the  $\nu_2$  mode of  $\text{CO}_3^{2-}$  [123]. Retained water within the corrosion layer is represented by the broad absorbed  $\text{H}_2\text{O}$  band from 2600-3600  $\text{cm}^{-1}$  and the minor peak for  $\text{OH}^-$  liberation at 630  $\text{cm}^{-1}$  [122]. The carbonate and phosphate bands compare well with EDS results as well as with previous literature, further suggesting that corrosion products of Zn alloys contain zinc (calcium) phosphate, zinc (calcium) carbonate, and zinc hydroxide compounds [118,124].

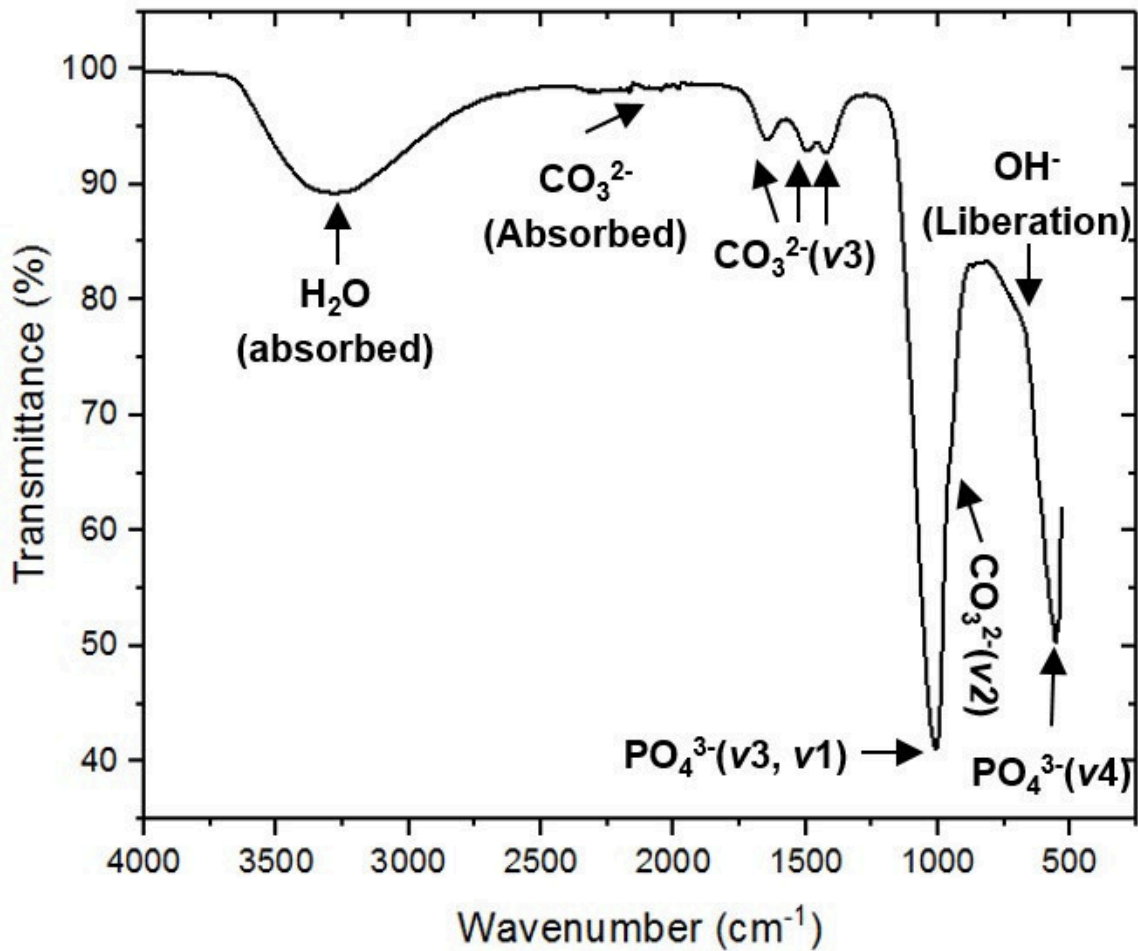


**Figure 24:** FTIR analysis of corrosion product agglomerates after *in vitro* immersion in HBSS.

Additional characterization of compound bond energies using XPS was utilized to corroborate with the EDS and FTIR data. Figure 25 presents the surface scan after Ar sputtering for 20 min for pure Zn and Zn-0.3Li-3.5Cu after 50 days of *in vitro* immersion corrosion. Since the sputtering time is low, primarily opportunistic impurities from the atmosphere are removed, leaving only the nanoparticle agglomerates and top surface of the dense corrosion layer to be measured. The binding energy spectra observed are not significantly different between the two samples tested, which is consistent with the similar observed corrosion product microstructure from SEM images. The spectra indicate the presence of C, O, Ca, S, P, Zn, Na, N, Mg, and Al.

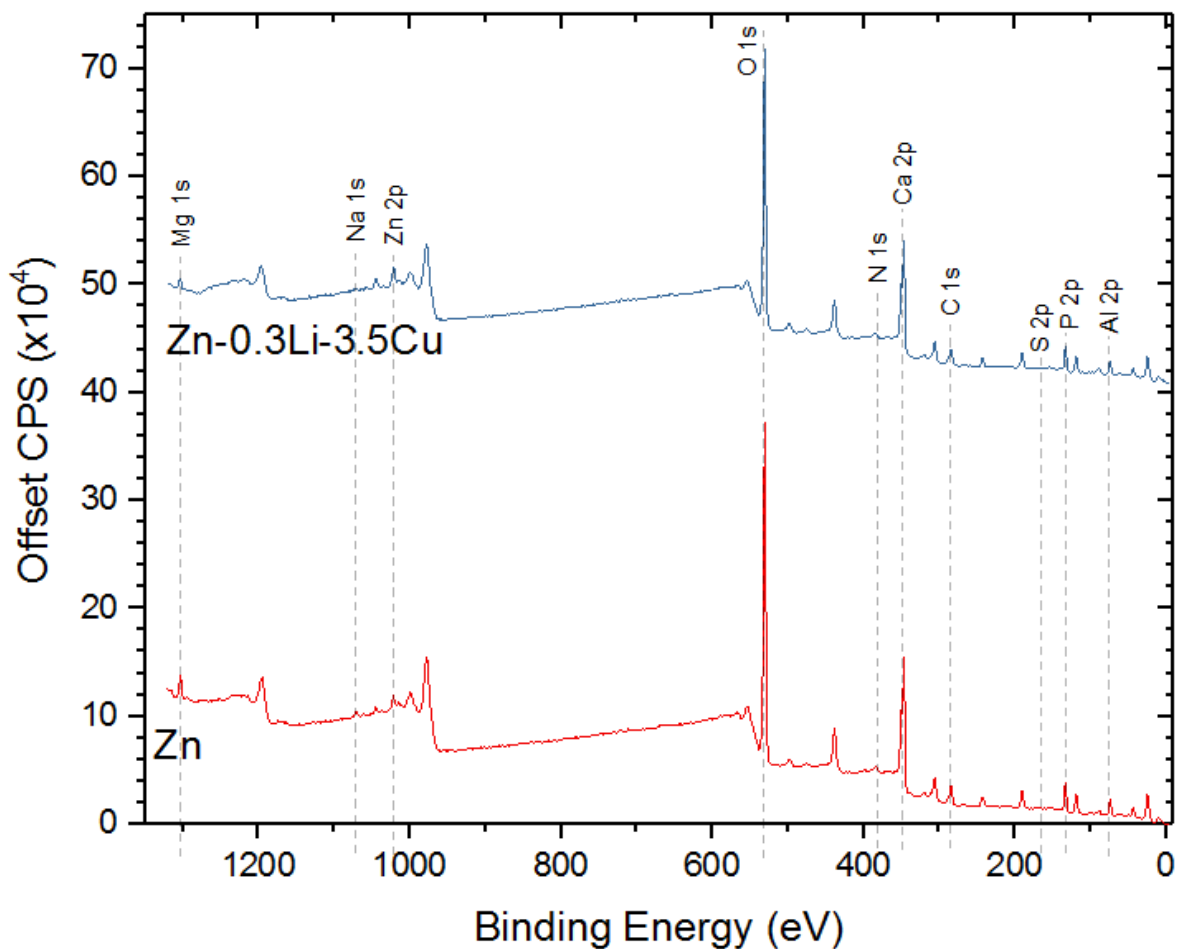


**Figure 25:** XPS spectra of Zn and Zn-0.3Li-3.5Cu corrosion product after 50 days *in vitro* immersion.

The small Al content present, represented at 74.31 eV and 74.75 eV (Al 2p) is assumed as sample contamination from previous polishing with Al<sub>2</sub>O<sub>3</sub> solution for cross-section analysis and will not be considered as part of the corrosion product or alloy [125]. The high resolution spectrum peak of carbon at 284.80 eV (C 1s) is attributed to C-C bonds or to hydrocarbon bonds (C<sub>x</sub>H<sub>y</sub>), representative of adventitious carbon [126–128]. The smaller carbon peak at 289.55 eV (C 1s) represents the presence of CO<sub>3</sub><sup>2-</sup> species [126,127]. A large spectrum peak at 530.80 eV (O 1s) highlights the significant presence of one or more oxygen-containing species, such as carbonates, oxides, or hydroxides [126,129]. Since a mixture of these compounds is likely and the binding energy shifts between them are small, it is difficult to differentiate between these species. Peaks at 347.35 eV and 350.93 eV (Ca 2p) signify the presence of calcium phosphates and/or carbonates [127,130]. Zn species binding energies are observed at 1021.94 eV and 1045.06 (Zn 2p), which commonly represents Zn-O bond. Zn metal bonds are normally present at lower energies, 1019 eV and 1042 eV, while oxides represent the energies observed in this study [131]. An additional minor peak at 89 eV (Zn 3p) is seen, likely indicating the presence of Zn<sub>3</sub>(PO<sub>4</sub>)<sub>2</sub> [132]. Evidence of phosphate species is seen by P peak at 134.23 eV (P 2p). Trace magnesium sulfate precipitates from the HBSS solution are present on the surface of the corrosion product, identifiable by the Mg peak at 49.8 eV (Mg 2p) and S peak at 170 eV (S 2p) [129]. A higher binding energy peak for associated with MgO or Mg(OH)<sub>2</sub> is observed at 1303.8 eV (Mg 1s) [129,133]. Finally, a small Na energy peak is visible at 1071.85 eV (Na 1s), traditionally representative of NaCl [134]. While no Cl species binding energy peaks were identified, EDS analysis observed Cl in the precipitate agglomerate product in Figure 23. Cl-containing compounds are likely present below the maximum XPS scan depth, due to

precipitation of or reaction with salt species (NaCl, KCl, CaCl<sub>2</sub>, MgCl<sub>2</sub>) in the HBSS saline solution.

In order to analyze the growth rate of the oxide product layer, sample cross-sections after immersion were prepared, shown in Figure 26. Careful grinding and specimen mounting were critical so as not to remove the attached corrosion layer near the ground surface. A continuous corrosion layer is formed on the alloy surface after only 5 days of immersion, exhibited in Figure 22a, and continues to grow in thickness through 50 days. No porosity is observed within each plate and the entire layer is consistent in thickness for each cross-sectional sample. The cracks separating each oxide plate run through the entire oxide layer to the metal surface, clearly observed in Figure 26c. This infers that HBSS continues to be in contact with alloy, promoting further metal dissolution and corrosion product formation.

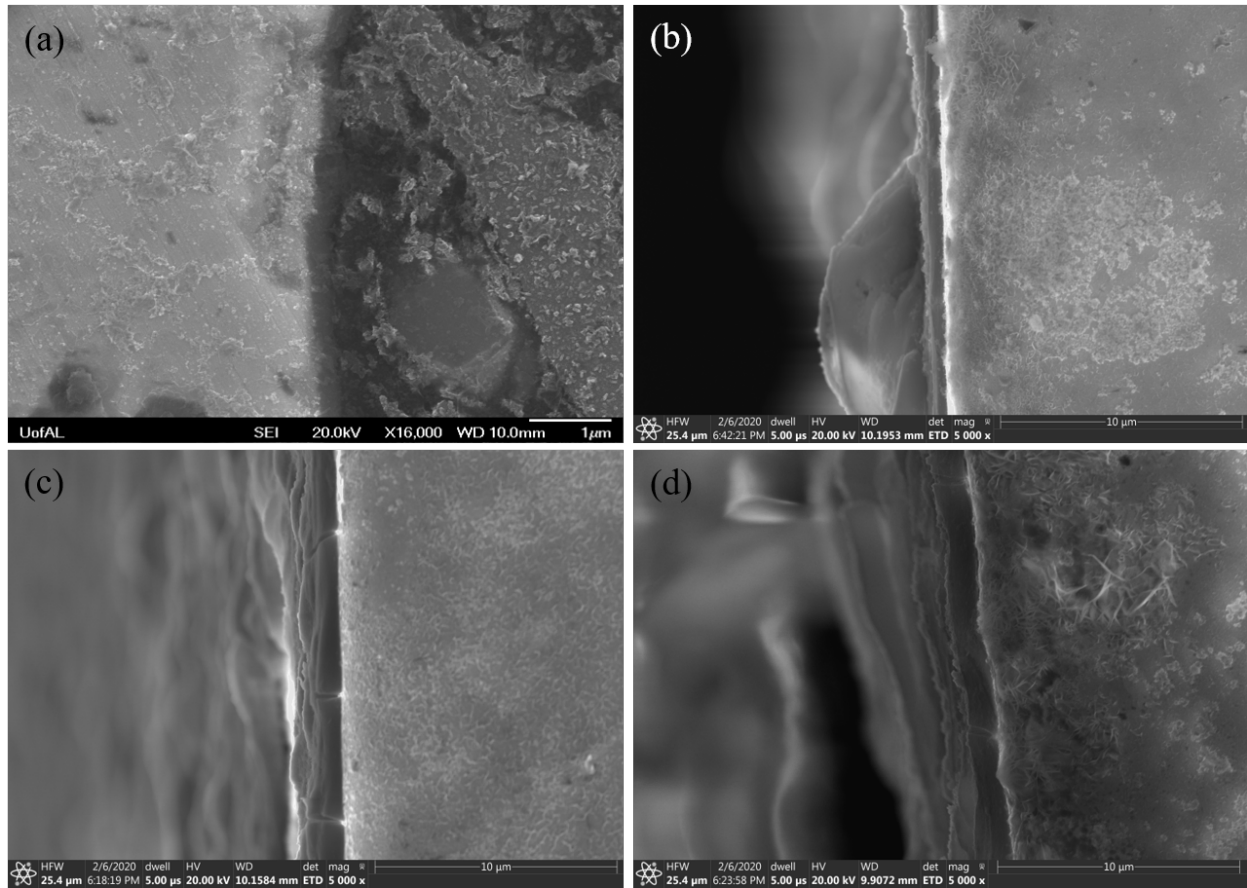


**Figure 26:** Cross-section SEM micrographs of pure Zn after (a) 5 days, (b) 12 days, (c) 21 days, and (d) 50 days of immersion corrosion.

After 100 days of *in vitro* immersion, the plated oxide layer (dark grey) is observed to be partially detached from the underlying alloy surface (light grey), shown in Figure 27.

Additionally, large pits on the metal surface are observed. Absence of oxide layer on the cross-sections of the 100 day corrosion samples also confirm the surface layer degradation. Pitting corrosion of varying severity has been commonly observed in Zn-containing biodegradable alloy systems, such as Zn-Li [135], Zn-Li-(Mg, Ag) [136], Zn-Cu-Mg [11], and Mg-Zn-Ca [137].

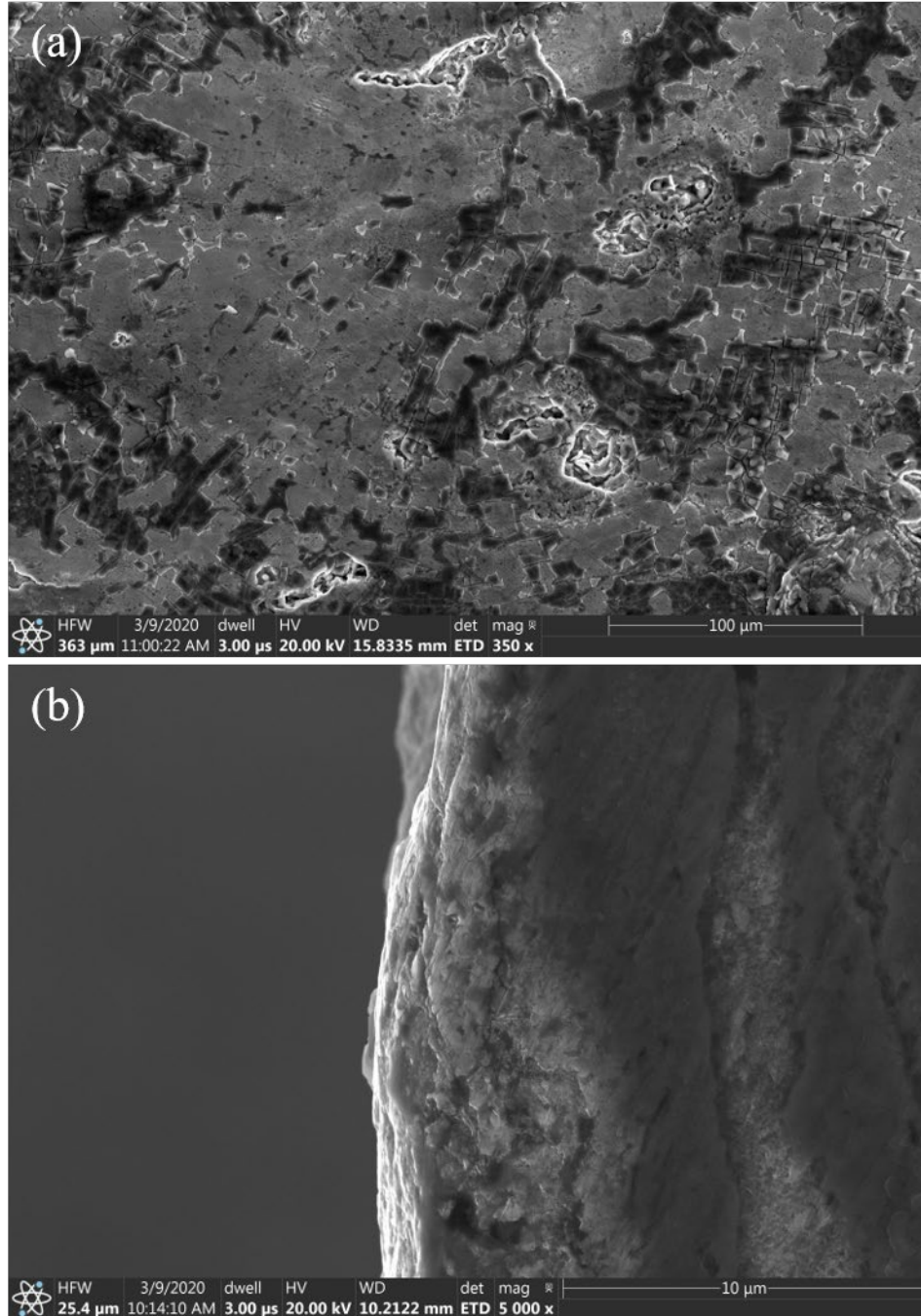


**Figure 27:** SEM micrographs of (a) surface and (b) cross-section of Zn-0.3Li-3.5Cu after 100 days of immersion corrosion.

To evaluate the rate of change in corrosion product growth, the oxide layer thickness was measured from SEM micrographs using ImageJ software and compiled in Figure 28. The initial condition samples that have not undergone corrosion can be assumed to have a 0 μm layer

thickness. Additionally, both of the 100-day samples are assumed to have effective thicknesses of 0  $\mu\text{m}$  since the absence of oxide product on the majority of the surface is a similar state to the pre-corrosion sample. In general, the plated product layer increases in thickness through the first 50 days and possibly beyond, but breaks down between 51 and 100 days of immersion. The ternary alloy was found to have a statistically thicker oxide layer than pure Zn, likely due to increased reactivity.

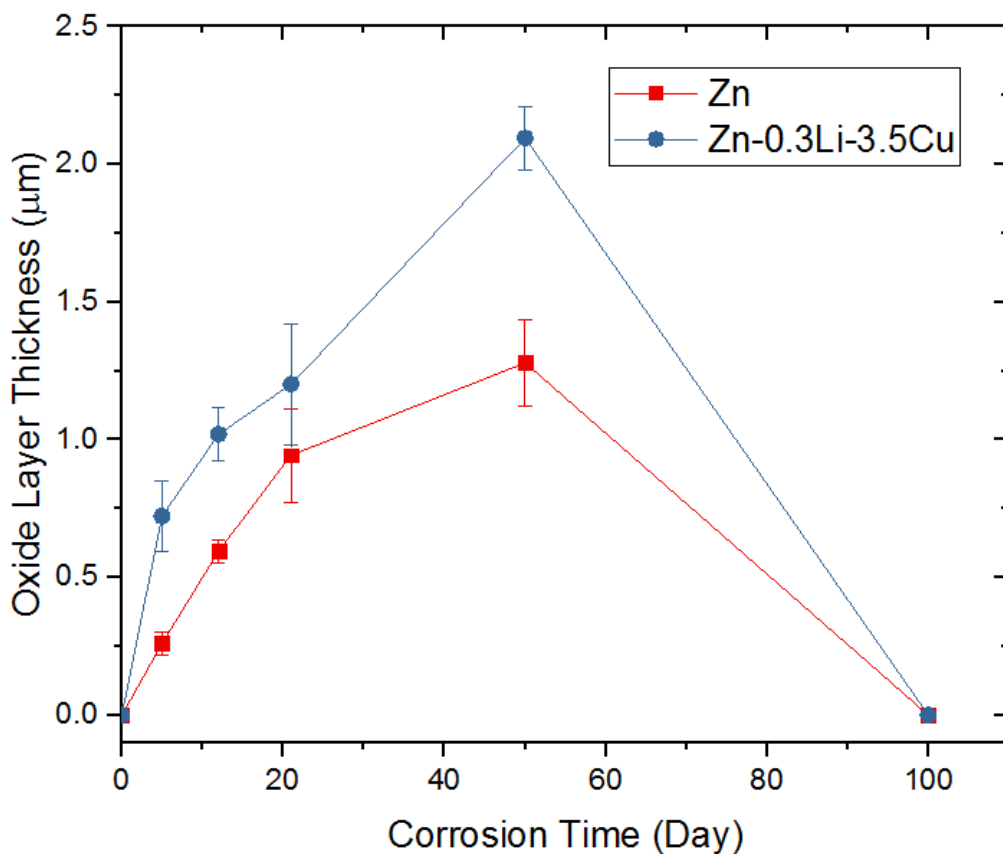


**Figure 28:** Oxide layer thickness with respect to *in vitro* immersion duration for pure Zn and Zn-0.3Li-3.5Cu samples.

Immersion corrosion rate was calculated according to Eq. 1 based on the sample weight loss after removal of corrosion products, summarized in Figure 29. An example calculation of corrosion rate is provided in Appendix III. The corrosion rate decreases over the first 12 days to approximately  $0.01 \text{ mm yr}^{-1}$  and stabilizes up to day 21 for all selected Zn-based alloys. The

initial decreasing trend is attributed to the formation of the dense corrosion product layer on the surface of the alloys (Figures 22 & 26), which inhibits the diffusion of metal into the solution. Slight differences between Zn and its alloys can be linked to competing galvanic corrosion effects and Cu nobility [138]. The corrosion rate can be predicted to increase between 51 and 100 days due to the observed product layer breakdown and progressive pitting behavior (Figure 27a). Zhao et al. [14] observed the *in vivo* corrosion rate to increase after 9 months, attributed to the loosening and dissolution of a passive film and rapid pitting.

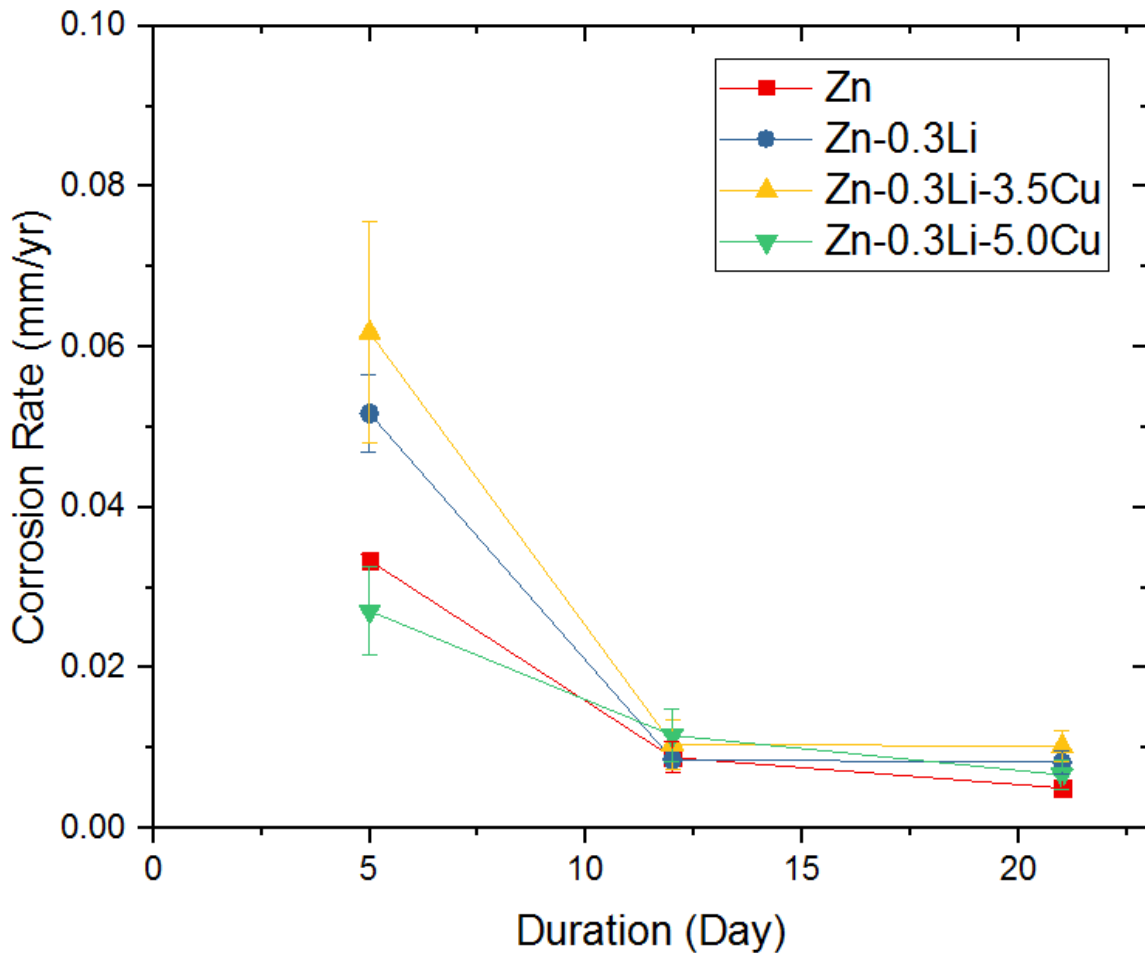


**Figure 29:** *In vitro* corrosion rate in HBSS of selected Zn-based alloys after 21 days.

The human body is an environment where fluids are constantly moving, therefore non-static *in vitro* testing was completed to determine any differences of *in vitro* corrosion rate and verify the

previous static testing results. A magnetic stir bar stirring at 60 rpm was utilized to simulate the non-static conditions within the human body. All other testing parameters were identical to non-stir immersion tests. A comparison of the corrosion rates of pure Zn with and without stirring is shown in Figure 30. The corrosion rates of stirring and no stirring of Zn are not statistically different ( $p > 0.05$ ), therefore one can assume stirring at 60 rpm for all of the studied alloys should also provide similar results. Ultimately, Zn-0.3Li-xCu alloys possess corrosion rates below the maximum criterion for stents in HBSS.

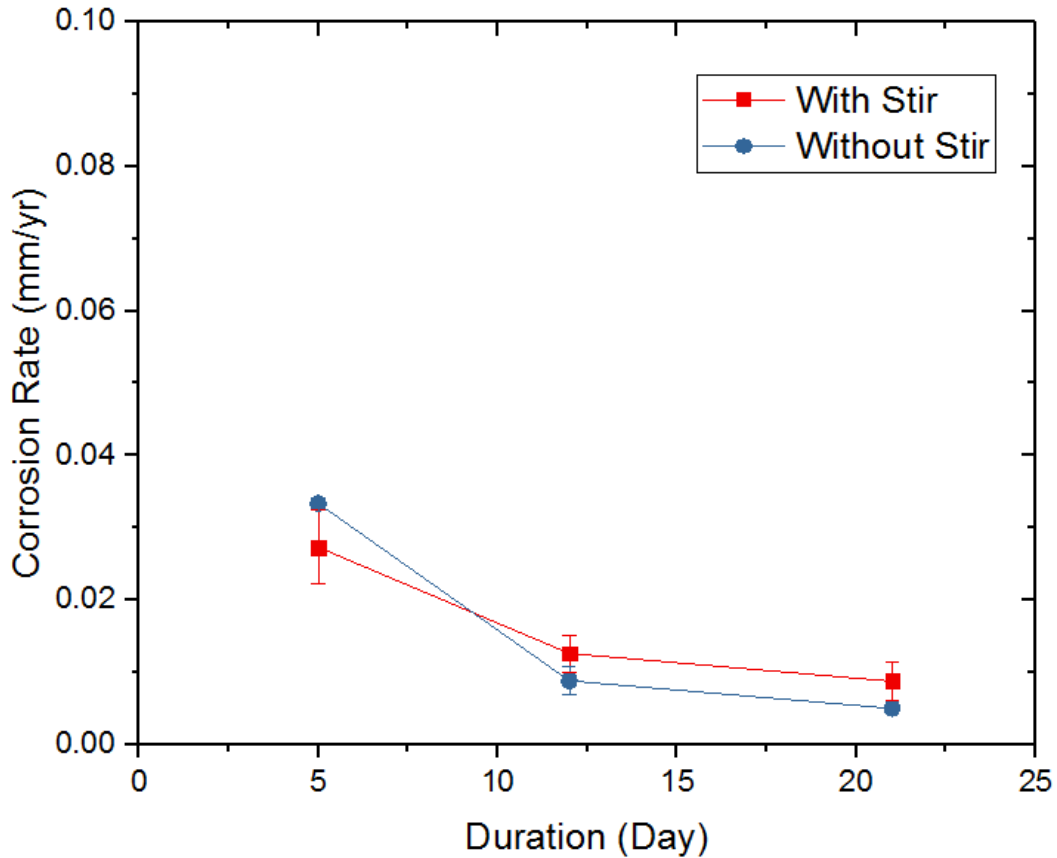


**Figure 30:** Comparison of *in vitro* corrosion rate of pure Zn in HBSS with and without solution stirring.

### 5.2.2 Electrochemical Impedance Spectroscopy Analysis

Electrochemical impedance spectroscopy (EIS) was carried out as an additional method to quantify corrosion resistance of the Zn alloy and corrosion product layer. Nyquist plots, a plot of the real ( $Z_r$ ) and imaginary ( $Z_i$ ) parts of complex impedance, are a common tool for analyzing resistance characteristics of electrochemical systems. The shape of the different arcs from the Nyquist curves are indicative of possible governing polarization mechanisms. The Nyquist plot for Zn-0.3Li-3.5Cu after *in vitro* immersion corrosion for 0 – 100 days is shown in Figures 31 and 32. Impedance values have been normalized with respect to sample surface area, thus  $Z/A$  is used for each axis.

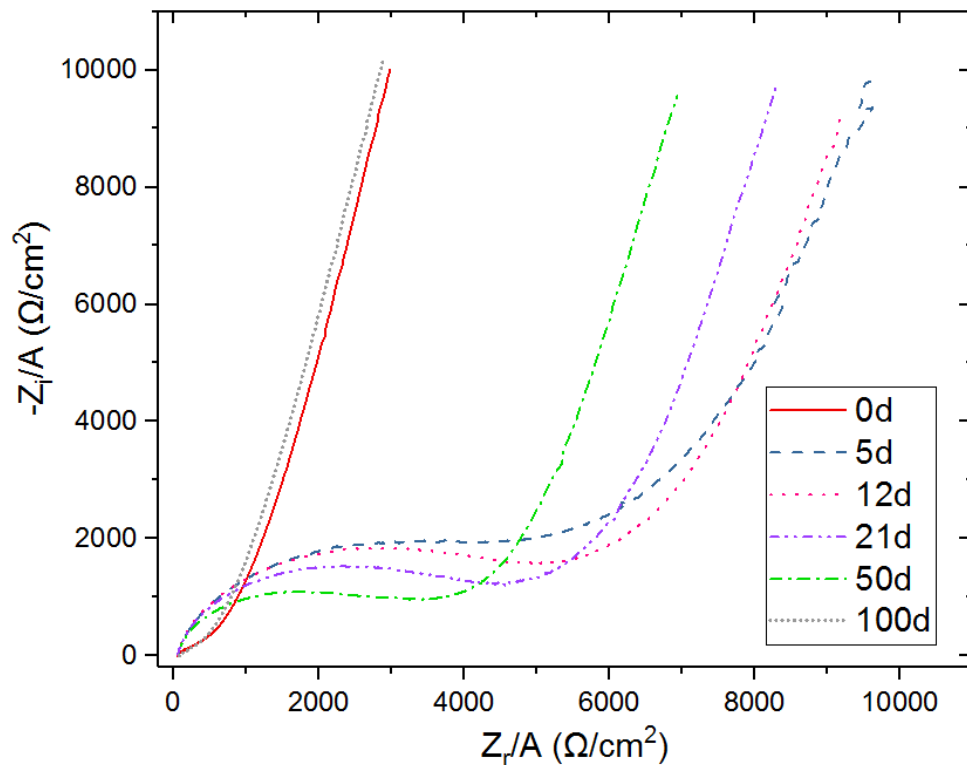


**Figure 31:** Nyquist plot of EIS measurement of Zn-0.3Li-3.5Cu after *in vitro* corrosion.

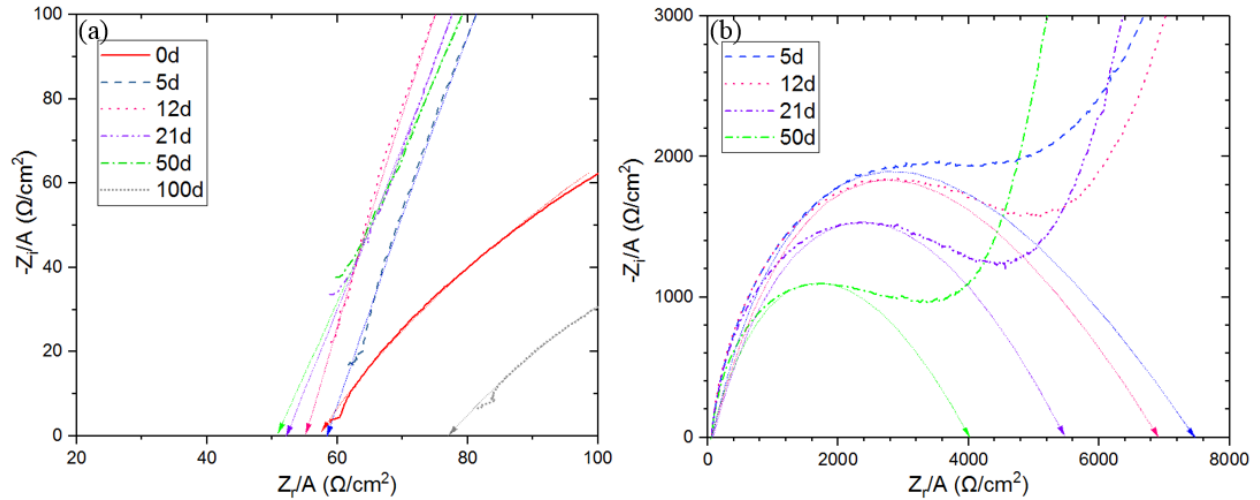


**Figure 32:** Extrapolated curve lines associated with (a)  $R_{\text{bulk}}$  and (b)  $R_{\text{CT}}$  from Nyquist plot of Zn-0.3Li-3.5Cu after *in vitro* corrosion.

The initial portion of the Nyquist plot can be defined as a large inductance loop, shown in Figure 32. The intersections of this arc on the  $Z_r$  x-axis corresponds to bulk series resistance ( $R_{\text{bulk}}$ ) (Fig. 32a) and charge transfer resistance ( $R_{\text{CT}}$ ) (Fig. 32b) [139]. The extrapolated resistances from Figure 32 are listed in Table 5 below.  $R_{\text{bulk}}$  normally consists of the internal resistance from the electrodes, lead wires, and electrolyte. Since the electrodes and wires are metal, which traditionally has very low resistance, one can assume  $R_{\text{electrolyte}} = R_{\text{bulk}}$ . The alloy and the electrolyte are assumed constant factors in each EIS experiment, therefore  $R_{\text{bulk}}$  expectantly does not vary significantly.

**Table 5:** Extrapolated  $R_{\text{bulk}}$  and  $R_{\text{CT}}$  of Zn-0.3Li-3.5Cu after *in vitro* corrosion.

Immersion duration (days)	$R_{\text{bulk}}$ ( $\Omega/\text{cm}^2$ )	$R_{\text{CT}}$ ( $\Omega/\text{cm}^2$ )
0	57	0
5	58	7416
12	55	6867
21	52	5440
50	51	3952
100	76	0

$R_{\text{CT}}$  is a measure of the difficulty for the passage of ions to perform certain redox reactions [140]. For example, simple charge transfer for a metal immersed and corroding in an electrolyte

would involve electrons entering the metal and metal ions diffused into the electrolyte simultaneously. From the Nyquist plot, the alloy before corrosion (0 day sample) and the 100 day sample do not have a  $R_{CT}$  loop ( $R_{CT} = 0 \Omega$ ), while  $R_{CT}$  is significant for 5, 12, 21, and 50 days corrosion. The buildup of the corrosion product with increasing immersion duration, observed in SEM, is correlated to  $R_{CT}$ . Before corrosion, the Zn alloy does not have a product surface layer, therefore charge transfer of ions between the alloy and electrolyte is not inhibited. When  $R_{CT} > 0$ , the thickness of the product layer is inversely proportional to  $R_{CT}$ . The plated layer in contact with the alloy is primarily composed of ZnO, which is known to be promising room-temperature semiconducting material [141]. When ZnO initially forms, the thickness is small and may be porous, inhomogeneous, or noncrystalline, where crystal structure defects can cause an increase in resistance. As corrosion progresses, ZnO continues to build and becomes a more homogeneous and crystalline layer, reducing  $R_{CT}$ . Eventually, the corrosion product is broken down and removed from the surface, observed in the 100 day sample, and the re-exposed alloy surface is directly in contact with the HBSS solution, similar to the initial condition.

### 5.2.3 Corrosion Product Formation

The general mechanism of Zn corrosion and product formation can be determined from the sample SEM micrographs, product characterization using FTIR and EDS, and corrosion resistance behavior from EIS. A schematic of the corrosion mechanism of pure Zn in HBSS is shown in Figure 33.

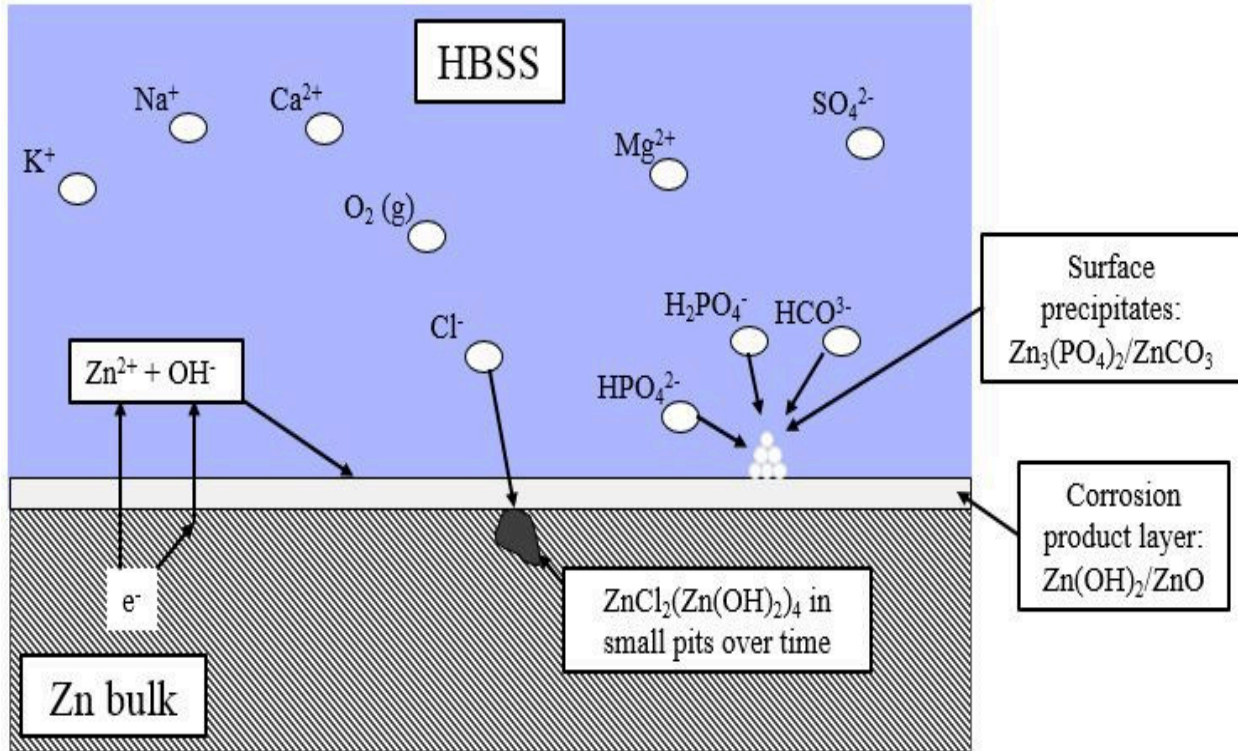


**Figure 33:** Schematic of the corrosion mechanism of pure Zn in HBSS.

The formation of the complex corrosion layer can be broken down into several steps. Given a primarily pure Zn bulk material and HBSS solution,  $Zn^{2+}$  ions and electrons diffuse into the surrounding solution. Free electrons combine with dissolved  $O_2$  and  $H_2O$  to form  $OH^-$  ions, which bond with  $Zn^{2+}$  to form  $Zn(OH)_2$  on the surface of the bulk Zn.  $Zn(OH)_2$  further dehydrates into  $ZnO$  as part of the plated layer observed on the surface of the alloy in Figures 22 and 26. As corrosion progresses over time, phosphate and carbonate compounds (e.g.  $Zn_3(PO_4)_2$ ,  $ZnCO_3$ ,  $CaCO_3$ ) in combination with metal ions precipitate from the solution as nanoparticle agglomerations on the surface of the oxide layer.

The small pits observed on the metal surface below the product layer is evidence of pitting corrosion. Initial pit formation is attributed to localized galvanic corrosion at the interfaces between the Zn matrix and secondary intermetallic phases, causing an accumulation of  $Zn^{2+}$  ions.

Acceleration of pit formation and growth is due to the migration of  $\text{Cl}^-$  ions from the HBSS into the thin cracks of the oxide layer and galvanic corrosion sites in order to have charge neutrality, where the exposed metal surface is the anodic site while the surrounding passive regions act as a cathode [142]. A high concentration of  $\text{ZnCl}_2$  within the pit reacts with water to produce  $\text{HCl}$  and  $\text{H}^+$  ions, locally lowering pH, which further accelerates pit corrosion [143]. The eventual breakdown and removal of the corrosion-resistant oxide layer occurs by pitting corrosion due to the formation of zinc chloride hydroxide monohydrate ( $\text{Zn}_5(\text{OH})_8\text{Cl}_2 \cdot \text{H}_2\text{O}$ ), a naturally occurring, water-insoluble, crystalline material commonly given as a nutritional supplement for animals [144,145]. The degradation of the oxide layer was experimentally observed after 100 days of *in vitro* immersion in Figure 19 as well from EIS experiments. The chemical reactions and their thermodynamic favorability are summarized below [6,12,146]. While the Gibbs energy of reaction for  $\text{Zn}_5(\text{OH})_8\text{Cl}_2 \cdot \text{H}_2\text{O}$  is unavailable, detailed synthesis and characterization was performed by Tanaka et al. [147], describing the spontaneous hydrolysis of  $\text{ZnO}$  nanoparticles in  $\text{ZnCl}_2$  solution over 48h.

*Basic anodic reaction:*  $\text{Zn} \rightarrow \text{Zn}^{2+} + 2\text{e}^-$  ( $\Delta G_{37^\circ\text{C}} = -147 \text{ kJ}$  [148])

*Basic cathodic reaction:*  $\text{O}_2 + 2\text{H}_2\text{O} + 4\text{e}^- \rightarrow 4\text{OH}^-$  ( $\Delta G_{37^\circ\text{C}} = -146.891 \text{ kJ}$  [148])

*Hydroxide formation:*  $\text{Zn}^{2+} + 2\text{OH}^- \rightarrow \text{Zn}(\text{OH})_2$  ( $\Delta G_{37^\circ\text{C}} = -94.388 \text{ kJ}$  [148])

*Oxide formation:*  $\text{Zn}(\text{OH})_2 \rightarrow \text{ZnO} + \text{H}_2\text{O}$  ( $\Delta G_{37^\circ\text{C}} = -4.327 \text{ kJ}$  [148])

*Carbonate formation:*  $\text{H}_2\text{O} + \text{CO}_2 \leftrightarrow \text{H}_2\text{CO}_3 \leftrightarrow \text{HCO}_3^- + \text{H}^+$  (Thermodynamic favorability is based on acid/base ratio [149,150])

$\text{ZnO} + \text{CO}_2 \rightarrow \text{ZnCO}_3$  ( $\Delta G_{37^\circ\text{C}} = -14.645 \text{ kJ}$  [148])

*Phosphate formation:*  $3\text{Zn}^{2+} + 2\text{H}_2\text{PO}_4^- + 4\text{OH}^- \rightarrow \text{Zn}_3(\text{PO}_4)_2 + 4\text{H}_2\text{O}$  ( $\Delta G_{37^\circ\text{C}} = -289.783$  kJ [148])

*Dissolution of corrosion layer from Cl<sup>-</sup> buildup in chloride solution:*

$5\text{Zn}^{2+} + 2\text{Cl}^- + 8\text{OH}^- + \text{H}_2\text{O} \rightarrow \text{Zn}_5(\text{OH})_8\text{Cl}_2 \cdot \text{H}_2\text{O}$  ( $\Delta G_{37^\circ\text{C}}$  not available)

The additions of Cu and Li can introduce possible complexities to the basic Zn corrosion mechanism and should be considered. Cu can readily form Cu<sub>2</sub>O in the presence of water and oxygen. The excess H<sup>+</sup> ions from oxidation as well as pitting corrosion will spontaneously reduce the Cu<sub>2</sub>O to pure Cu and water. *In vitro* immersion corrosion of pure Cu in body fluids was investigated by Fattah-Alhosseini et al. [151], Gholami et al. [152], and Mora et al. [153] who summarized Cu corrosion by the following two reactions:

*Oxide formation:*  $8\text{Cu} + 2\text{H}_2\text{O} + \text{O}_2 \rightarrow 4\text{Cu}_2\text{O} + 4\text{H}^+ + 4\text{e}^-$  ( $\Delta G_{37^\circ\text{C}} = -117.333$  kJ [148])

*Oxide breakdown:*  $\text{Cu}_2\text{O} + 2\text{H}^+ \rightarrow 2\text{Cu}^{2+} + \text{Cu} + \text{H}_2\text{O}$  ( $\Delta G_{37^\circ\text{C}} = -22.715$  kJ [148])

Additionally, pure Li is known to readily and quickly oxidize in atmospheric conditions by the following reaction:

*Oxide formation:*  $4\text{Li} + \text{O}_2 \rightarrow 2\text{Li}_2\text{O}$  ( $\Delta G_{37^\circ\text{C}} = -1119.332$  kJ [148])

Given that Cu is more noble than Zn, it is fair to assume that CuZn<sub>5</sub> intermetallic phase is more noble than the surrounding ηZn matrix [48]. Zhao et al. [14] postulates that LiZn<sub>4</sub> is nobler than the ηZn matrix as well. When solutes are more noble than the matrix and are distributed finely and homogeneously, an “enveloping effect” that increases corrosion resistance has been noted to occur in some binary systems, including Zn-Cu by Osório et al. [138]. This effect seems to

mitigate the majority of galvanic corrosion induced by phases with different cell potentials, based on the relatively consistent corrosion rates of the selected Zn alloys of this study.

### 5.3 Mechanical Properties

#### 5.3.1 Tensile Testing

Uniaxial tensile testing was accomplished to assess the basic mechanical properties of the hot-rolled Zn-Li-Cu alloys. Figure 34 shows representative stress versus strain curves for each of the studied materials observed by tensile tests. Ultimate tensile strength can be determined from the peak engineering stress experienced by the sample. Yield strength is taken at the 0.02 strain offset on the curve using the slope of the initial elastic region (i.e. modulus of elasticity). The elongation to failure is the extent of strain at fracture or 10% of ultimate tensile strength in the case of extreme necking behavior [110]. Young's modulus, or modulus of elasticity, is taken from the slope of the initial linear portion of the elastic region starting at zero stress and strain. Perfectly linear behavior of the data in terms of linear regression means that  $R^2 = 1$ , where  $R^2$  is a goodness of fit term that expresses the fraction of unexplainable error. There was no perfectly linear portion of the stress-strain curve, so the linear region was defined in this study as the portion of data where  $R^2 \geq 0.998$ , which allowed for at least 10 data points per curve. The calculated modulus is very sensitive to the amount of data points used and value of  $R^2$ , so the resulting modulus values have significant standard deviations of ~5-10%.

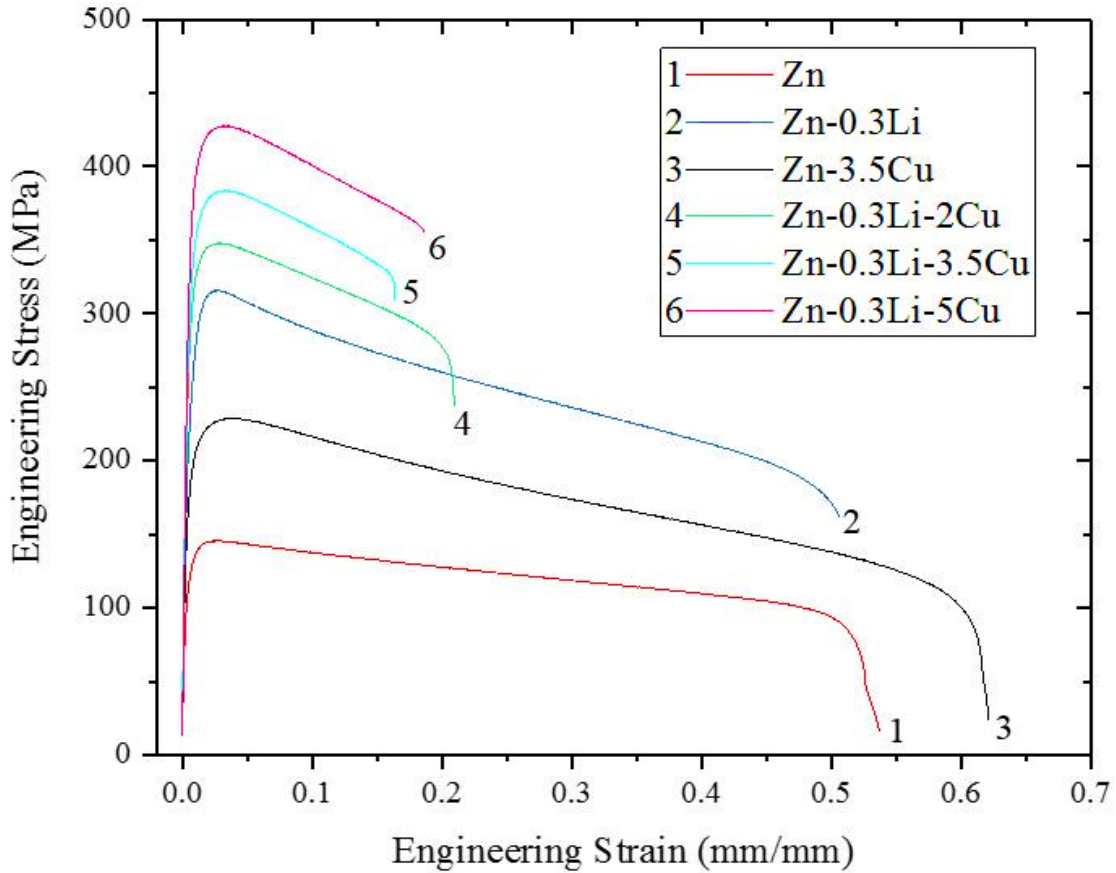


**Figure 34:** Representative engineering stress vs. engineering strain curves of hot-rolled Zn-based alloys.

Traditionally, as-cast pure Zn has low strength and ductility attributed to large grain size, minimal work hardening, and inherent defects from casting [45]. The hot-rolled pure Zn sample expectedly has inferior strength compared to the studied alloys, while attaining a large amount of plasticity, similar to wrought zinc [45,154]. The behavior of Zn-0.3Li and Zn-3.5Cu binary alloys have heightened ultimate tensile and yield strengths, along with a similar large plastic region to the pure Zn. This observation is in good agreement with the previous work by Zhao et al. [12] and Niu et al. [10]. The novel Zn-Li-Cu alloys further increase mechanical strength comparatively as Cu content rises. This comes at the expense of plasticity as a smaller elongation to fracture is observed.

Young's modulus, a measure of material stiffness, is 70 GPa for as-cast and rolled pure Zn [155]. Modulus is insensitive to microstructure, processing conditions, or defects, and is primarily a function of composition. As-cast pure Zn is also naturally weak and brittle, while wrought Zn has an increased strength and amount of plasticity before fracture. Adding Li and Cu alloying elements increases the modulus compared to pure Zn, inferring that  $\alpha\text{LiZn}_4$  and  $\epsilon\text{CuZn}_5$  have a higher modulus than  $\eta\text{Zn}$ . The average tensile properties of the studied alloys in the rolling direction, as well as similar previously reported materials, are summarized in Table 6.

**Table 6:** Mechanical properties of hot-rolled Zn-based alloys from this study and selected Zn alloys from literature. \*Data extrapolated from figures in literature.

Alloy	Ultimate tensile strength (MPa)	Yield strength (MPa)	Elongation to failure (%)	Young's Modulus (GPa)
Cast Zn* [155,156]	18	10	0.32	70
Rolled Zn* [155]	126	-	65	70
Zn-0.35Li* [12]	443	426	14	-
Zn-3Cu* [7]	257	214	47	-
Zn	145.89 ± 1.85	99.01 ± 7.29	52.19 ± 4.72	54.44 ± 4.01
Zn-0.3Li	316.15 ± 3.62	197.28 ± 5.60	51.80 ± 9.78	69.35 ± 3.74
Zn-3.5Cu	223.83 ± 3.47	142.74 ± 2.86	59.32 ± 14.69	69.63 ± 4.73
Zn-0.3Li-2Cu	333.49 ± 12.38	226.55 ± 16.47	26.00 ± 7.71	74.91 ± 7.18
Zn-0.3Li-3.5Cu	382.80 ± 5.29	231.63 ± 5.66	18.33 ± 6.03	92.91 ± 7.49
Zn-0.3Li-5Cu	427.92 ± 9.87	272.87 ± 12.55	19.30 ± 3.42	76.88 ± 5.14

ANOVA and Tukey testing ( $\alpha = 0.05$ ) was utilized to analyze statistically significant differences between alloys for each mechanical property in Table 6. ANOVA tests an alternative hypothesis (i.e. one or more samples are different) against the null hypothesis (all samples are equal), where the confidence level,  $\alpha$ , is generally 95% or higher [157]. If the p-value, the probability of having a test result as or more extreme given the null hypothesis is true, is less than  $\alpha$ , then the null hypothesis is rejected. For all four properties,  $p \approx 0$  when  $\alpha = 0.05$ , therefore the alternative hypothesis is accepted, where a difference exists between one or more alloys for each property.

The Tukey test, a subsequent test to ANOVA given that the alternative hypothesis is accepted, is used to find all possible differences between each pair of sample means [157]. For both ultimate tensile strength and yield strength, all six alloys are statistically different from one another.

Elongation to failure was separated into two statistically similar grouping, where Zn, Zn-0.3Li, and Zn-3.5Cu had better ductility than the three selected ternary alloys. Finally, Zn had the lowest modulus, while Zn-0.3Li-3.5Cu had the highest. The mean differences between the other four alloys were statistically insignificant. It is likely that a greater sample size or more accurate measurement method could lower variance and capture smaller differences in elongation and modulus means.

While as-cast pure Zn is weak and brittle, the hot-rolling method induces dynamic recrystallization, a process which allows for new strain-free grains to grow and elongate in dislocation-dense regions, illustrated in Figure 35.

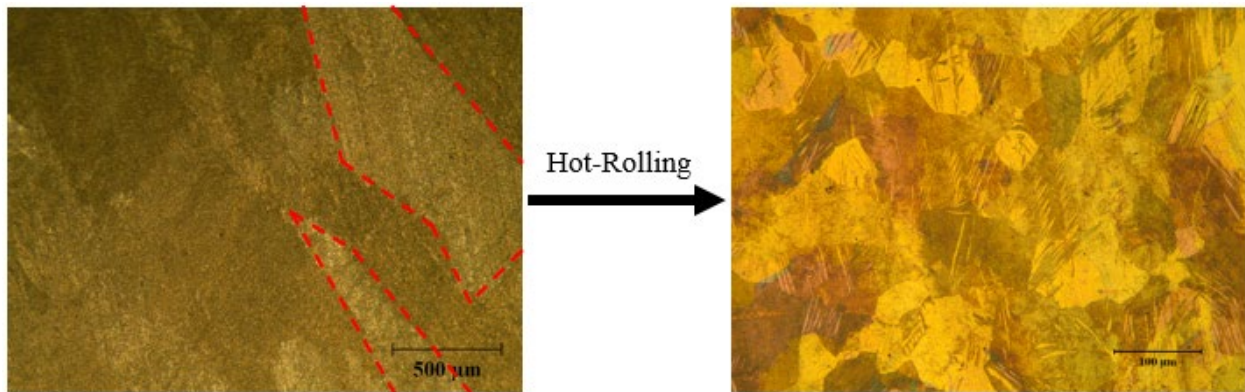


**Figure 35:** Change in grain size for pure Zn after hot-rolling. Dotted lines highlight large grains in as-cast Zn.

Grain size reduction is linked to yield strength through the Hall-Petch relationship (Eq. 4):

$$\sigma_y = \sigma_0 + \frac{k_y}{\sqrt{D}} \quad (4)$$

where  $\sigma_y$  is the yield stress in MPa,  $\sigma_0$  is a material constant relating to the resistance of dislocation motion within the lattice in MPa,  $k_y$  is a material-dependent strengthening constant in MPa m<sup>1/2</sup>, and  $D$  is the grain size in m [33]. Ultimately, hot-rolling causes grain refinement, grain boundary strengthening, and an overall observance of increased mechanical properties [35]. The Zn samples from this study observe superior strength and ductility attributed to hot-rolling compared to as-cast Zn.

Further strengthening of hot-rolled Zn occurs by alloying with Li and Cu, observed in Table 6. Small regions of solid solubility exist within the Zn-rich portions of the Zn-Li [73] and Zn-Cu [69] binary phase diagrams, meaning a temperature dependent amount of Li and Cu can exist in solution of the  $\eta$ Zn phase. The equilibrium solute composition of the  $\eta$ Zn for Zn-0.3Li-3.5Cu from the simulated Zn-Li-Cu phase diagram predicts 1.24 wt.% Cu and 0.32 wt.% Li at 350 °C, decreasing down to 0.07 wt.% Cu and 6.5E-4 wt.% Li at room temperature, illustrated in Figure 36. Therefore, solid solution effects are expected to be a small contribution to strengthening from alloying, where Cu and Li solutes act as lattice distortions in the  $\eta$ Zn phase that impede dislocation movement and require greater stress to enable plastic deformation. One can also expect the contribution of solid solution strengthening to decrease if the  $\eta$ Zn phase fraction decreases since there is no solubility of Li in  $\epsilon$ CuZn<sub>5</sub> or Cu in  $\alpha$ LiZn<sub>4</sub> or  $\beta$ LiZn<sub>4</sub>.

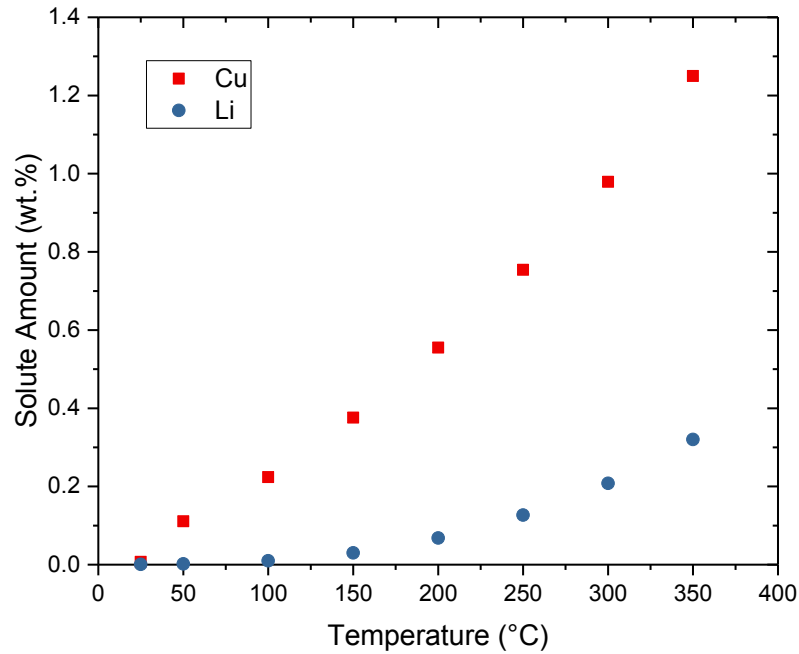


**Figure 36:** Amount of Cu and Li solutes within the  $\eta$ Zn phase from 25 – 350 °C for Zn-0.3Li-xCu ( $2 \leq x \leq 5$ ).

The formation of secondary phase precipitates is also responsible for the strength increase in hot-rolled alloys compared to pure Zn. From optical microscopy in Figure 15, hot-rolling is observed to break up and disperse the  $\alpha$ LiZn<sub>4</sub> and  $\epsilon$ CuZn<sub>5</sub> phases as elongated particles and regions, parallel with the hot-rolling direction, surrounded by the  $\eta$ Zn matrix. The small particles act as dislocation sliding barriers and require either cutting through or bowing around each particle, based on particle radius, for continuation of dislocation movement [158]. Cutting through particles introduces new particle-matrix interfaces and an increased surface energy. Bowing around particles leaves residual dislocation loops around particles. Both mechanisms increase the energy (i.e. stress) required for further deformation. As Cu content increases in the ternary alloys, the CuZn<sub>5</sub> particle content increases, providing additional dislocation barriers and increased strength.

The significant decrease in elongation to failure of the ternary alloys compared to hot-rolled Zn, Zn-0.3Li, and Zn-3.5Cu can be associated with the change in volume fraction of the ductile  $\eta\text{Zn}$  phase, observed to have an extensive plastic range in this study. Based on the Zn-Li-Cu simulated phase diagram in Figure 19, the volume fraction of each phase is predicted, listed in Table 7. The combined volume fraction of  $\alpha\text{LiZn}_4 + \epsilon\text{CuZn}_5$  is comparable to the experimental area fraction measurements from optical micrographs in Figure 15. Based on measured tensile properties, a critical amount of  $\eta\text{Zn}$ , between 0.771 and 0.666 volume fraction, is assumed necessary to preserve bulk sample ductility and keep elongation at  $>50\%$ .

**Table 7:** Simulated equilibrium volume fraction of phases at 25 °C for studied Zn-based alloys.

Alloy	$\eta\text{Zn}$	$\alpha\text{LiZn}_4$	$\epsilon\text{CuZn}_5$
Zn	1	0	0
Zn-0.3Li	0.793	0.207	0
Zn-3.5Cu	0.771	0	0.229
Zn-0.3Li-2Cu	0.666	0.207	0.127
Zn-0.3Li-3.5Cu	0.569	0.207	0.224
Zn-0.3Li-5Cu	0.472	0.207	0.321

One can approximate the Zn-Li-Cu ternary alloys as multi-phase aggregates, similar to a composite material, where  $\eta\text{Zn}$  is a soft matrix material and  $\alpha\text{LiZn}_4$  and  $\epsilon\text{CuZn}_5$  phases are stronger reinforcing materials with a combined, significant volume fraction. In general, the ductility of composite materials decrease as the volume fraction of the secondary phase increases, experimentally observed for Cu composites by Edelson and Baldwin [159] and for aged Al alloys by Liu et al. [160]. This behavior is true regardless of if the secondary phase is in the form of particles or large constituents, although constituents have a more detrimental effect on ductility [160].

Large particles or regions of a stiff second phase act as barriers to matrix slip, resulting in elevated stress concentrations at the second phase during tensile load [161]. Strain energy, a form of potential energy, is stored as stress concentrations increase, based on Eq. 5 for materials in uniaxial stress:

$$U = \frac{1}{12G} 2\sigma^2 \quad (5)$$

where U is total strain energy density in  $\text{J m}^{-3}$ , G is shear modulus in MPa, and  $\sigma$  is applied stress in MPa [162]. The strain energy is released when cracks are formed. Griffith [163] proposed that for completely brittle materials (e.g. glass) when the stored potential energy is greater than the energy increase from increased surface area due to crack propagation, a crack will grow by Eq. 6:

$$U \geq 2\gamma_s \quad (6)$$

where  $\gamma_s$  is surface energy in J [164]. Therefore the stress required for crack propagation given no change in total system energy is presented in Eq. 7:

$$\sigma = \left( \frac{2E\gamma_s}{\pi c} \right)^{1/2} \quad (7)$$

where E is elastic modulus in GPa and c is crack length in nm [165]. Orowan later suggested that plastic deformation increases the required stress for crack propagation due to crack tip blunting by Eq. 7:

$$\sigma = \left[ \frac{2E(\gamma_s + \gamma_p)}{\pi c} \right]^{1/2} \quad (7)$$

where  $\gamma_p$  is the plastic work in J required to extend the crack surface [165].

By approximating hot-rolled Zn-Li-Cu alloys as composites, the elongated  $\epsilon\text{CuZn}_5$  and  $\alpha\text{LiZn}_4$  intermetallic phases act as rigid, lamellar “fibers” while surrounded by a more ductile  $\eta\text{Zn}$  matrix. Stress concentrations build up in the intermetallic second phases, which favors crack propagation at a certain stress level. The  $\eta\text{Zn}$  matrix allows for a large amount of plastic deformation to occur, blunting the cracks and increasing the stress needed for crack growth. In the binary alloys, the volume fraction of  $\eta\text{Zn}$  is large enough that ductile failure occurs before the brittle failure of the intermetallic phase due to extreme plastic deformation. Evidence of this is observed by the twinning behavior in pure Zn in Figure 15a. As the volume fraction of  $\eta\text{Zn}$  decreases past a critical point in the ternary alloys, it is easier to make a continuous crack path through the more rigid secondary phases, ultimately decreasing the elongation to failure.

### 5.3.2 Vickers Hardness

Vickers hardness testing was utilized to determine the hot-rolled alloys’ resistance to permanent deformation through indentation. Figure 37 presents the hardness for the studied alloys. An example calculation of Vickers hardness is provided in Appendix IV.

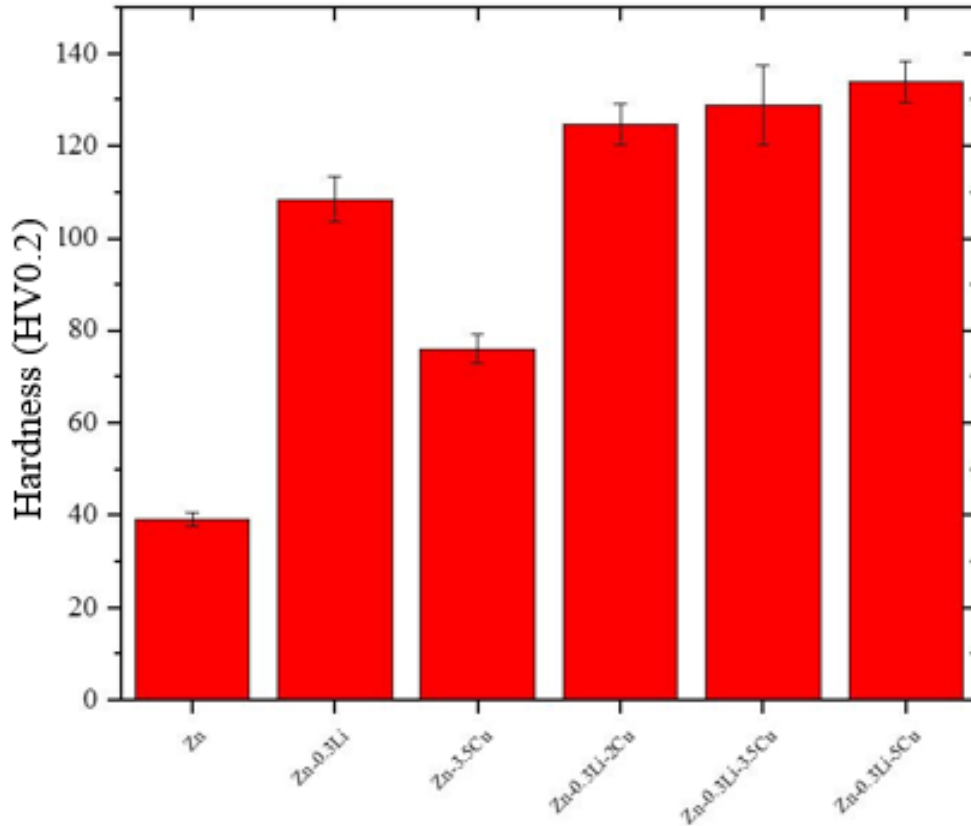


**Figure 37:** Vickers hardness of hot-rolled Zn-based alloys.

Hot-rolled pure Zn exhibits a low hardness of  $39.16 \pm 1.49$  HV0.2, an expected behavior based on the suboptimal tensile strength properties. It is evident that alloying with separately with Li and Cu both increase the hardness of Zn. One can hypothesize that  $\alpha\text{LiZn}_4$  is harder than both  $\epsilon\text{CuZn}_5$  and  $\eta\text{Zn}$  based on pure Zn and binary alloys. The hardness of worked  $\text{CuZn}_5$  is 45-125 HV [166,167], while the hardness of  $\text{LiZn}_4$  has not been reported. Additions of Li and Cu simultaneously further increase the hardness, but to a lesser extent. The effects of each alloying element are not purely additive based on only marginal hardness increases as Cu content is increased. ANOVA analysis observed a p-value  $\approx 0$ , meaning that one or more differences between alloy sample means exist. Tukey testing found that for all pairs of sample hardness

means, with the exception between Zn-0.3Li-2Cu and Zn-0.3Li-3.5Cu, there exists a significant difference between them.

Methods of augmenting hardness are closely related to the basic strengthening methods of metals mentioned previously. While as-cast Zn only has a hardness of 30 HV [168], hot-rolled Zn is ~30% higher due to grain boundary strengthening from the hot-rolling process. During deformation, dislocations can pileup near grain boundaries of two grains with different orientations. There is a resistive force to further deformation associated with the dislocation pileup based on the stress concentration at the boundary, represented by the parameter  $(d/4r)^{1/2}$ , where  $d$  is dislocation density and  $r$  is grain radius [158]. Therefore, as grain size decreases, it takes a smaller dislocation density to achieve the same stress concentration and a higher applied stress to activate flow. This behavior is summarized by Eq. 4, the Hall-Petch relationship [158].

Hardening due to solid solution interactions is a primary reason why the alloys are harder than pure Zn. Since the amount of Li and Cu in Zn is past their respective solute saturation limits, there is a significant amount of interaction energy present between the solute atoms and dislocations generated from applied stress. Solute atom type can either be substitutional or interstitial based on the size difference between the host and solute atoms. The atomic radii of Zn (139 pm) [169] and Cu (140 pm) [170] are similar, while Li (182 pm) [171] is significantly larger. As Cu and Li are both greater in size than Zn, substitutional solid solution is expected. Since Li is much larger than Zn compared to Cu, Li is a more effective strengthening alloying element, observed in the tensile and hardness data. Substitutional solute atoms generate an elastic interaction based on their attractive or repulsive stress fields in relation to edge dislocation cores, depending on their orientation and lattice distortion geometry [172]. These stress fields increase

the applied stress necessary for dislocation motion and deformation. The change in shear stress of a solid solution can be determined by Eq. 9:

$$\Delta\tau = Gb\varepsilon^{3/2}c^{1/2} \quad (9)$$

where  $b$  is the length of the Burger's vector in Å,  $\varepsilon$  is solute lattice strain, and  $c$  is concentration of solute atoms in mol m<sup>-3</sup> [173]. Vickers hardness is also traditionally linearly related to strength for work-hardened materials ( $H_v \approx 3\sigma$ ), which is approximately observed in this study [174]. Therefore, the amount of hardening is proportional to the misfit of the solute atom, experimentally observed by an increased hardness and atomic radius in Zn-0.3Li compared to Zn-3.5Cu.

Small secondary phase precipitates of  $\varepsilon\text{CuZn}_5$  and  $\alpha\text{LiZn}_4$  dispersed in the  $\eta\text{Zn}$  matrix also contribute to the observed hardening effect in alloys, although not to the same extent as the major, elongated phase regions. Similarly to the effect of precipitates on strength, dislocation motion is impeded by small precipitates. Dislocations must either shear through or circumvent second phase particles based on their size and average spacing. At a particular particle radius, there is a critical resolved shear stress required for dislocation movement past a particle [172]. When particle radius is small, the shear stress for a dislocation to cut through is given by Eq. 10:

$$\tau = CG\gamma^{3/2} \sqrt{\frac{fr}{b}} \quad (10)$$

where  $\gamma$  is effective interface energy in J,  $C$  is solute atom concentration in mol m<sup>-3</sup>,  $f$  is volume fraction of precipitates, and  $r$  is particle radius in m [175]. The stress required for a dislocation to instead circumvent a particle, generating a dislocation loop, is the Orowan stress, given by Eq.

11:

$$\tau = \frac{Gb}{\ell - 2r} \quad (11)$$

where  $\ell$  is average particle spacing ( $\ell = \frac{r}{\sqrt{f}}$ ) [175]. Nature will choose the most favorable process, so the applied shear stress to bypass a particle of a given radius will be dependent on whichever of Eq. 10 or 11 is a lower energy magnitude.

Since there exist large regions of the secondary phases in both the binary and ternary alloys, these materials can be classified as multi-phase aggregates. These elongated intermetallic phase regions are the primary contribution to strengthening from alloying. The microstructure of the phases in an aggregate can be textured, where the extremes are expressed in two cases, shown in Figure 38.

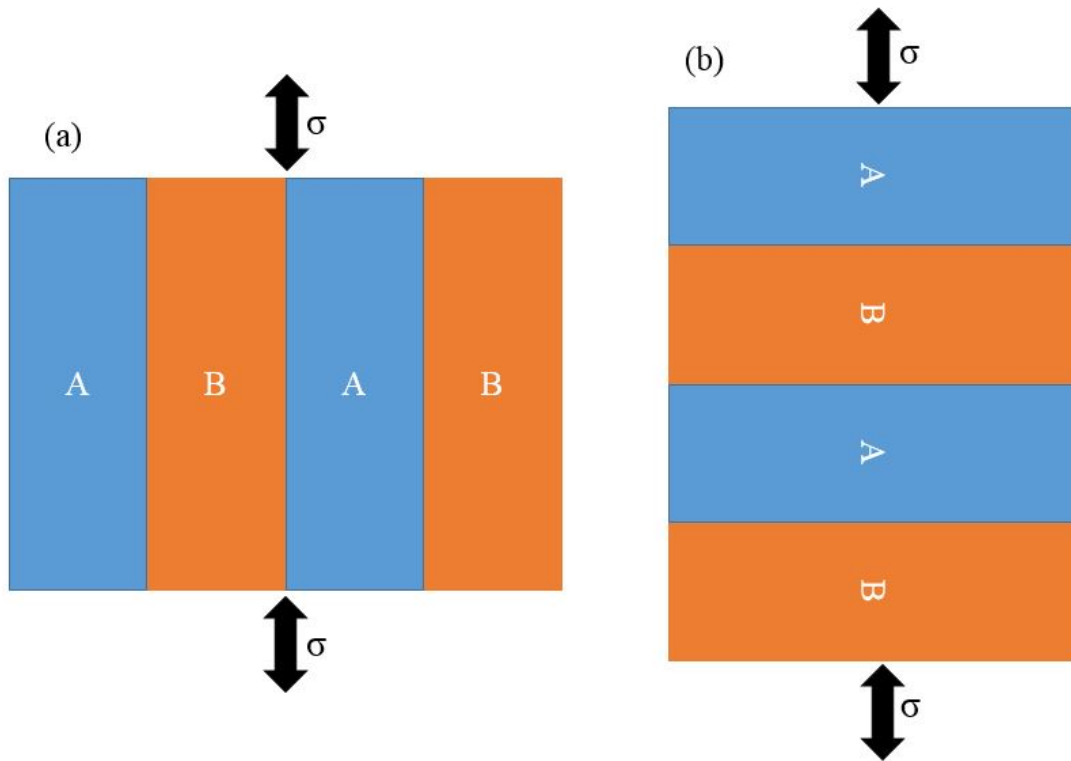


**Figure 38:** Schematic diagram of (a) upper bound iso-strain model and (b) lower bound iso-stress model for an alloy composed of phases A and B.

These two models form the upper bound (Reuss approximation) and lower bound (Voigt approximation) property extremes of the mixture rule considering either uniform strain or stress of all phases. Therefore, the hardness can be related to the phase fractions, based on the mixture rule, given by Eq. 12 (upper bound) and 13 (lower bound) [176]:

$$\overline{HV}_{up} = \sum_{i=1}^n HV_i f_i \quad (12)$$

$$\overline{HV}_{low} = [\sum_{i=1}^n (f_i / HV_i)]^{-1} \quad (13)$$

Regardless of the texture of the alloy, adding a harder second phase to a softer matrix material will increase the overall hardness of the alloy within the bounds of Eq. 12 and 13. Evidence of this is observed experimentally in Zn-0.3Li-xCu as the hardness increases when the Cu content and the harder CuZn<sub>5</sub> phase fraction increases in relation to the softer Zn matrix.

### 5.3.3 Fracture Surface Morphology

Scanning electron microscopy (SEM) was utilized to characterize the fracture surface morphology after tensile testing and to compare to the measured mechanical properties in Table 6. Tensile testing results emphasized two statistically different groups of materials based on elongation to failure. Pure Zn and the binary alloys had >50% elongation, while the ternary alloys possessed ~20% elongation to failure. By observing the fracture surfaces of each material, a stark difference in fracture mechanism is detected between the two groups. The nucleation of microvoids is very clearly observed in Figures 39 and 40, traditionally associated with ductile fracture and a high elongation to failure.

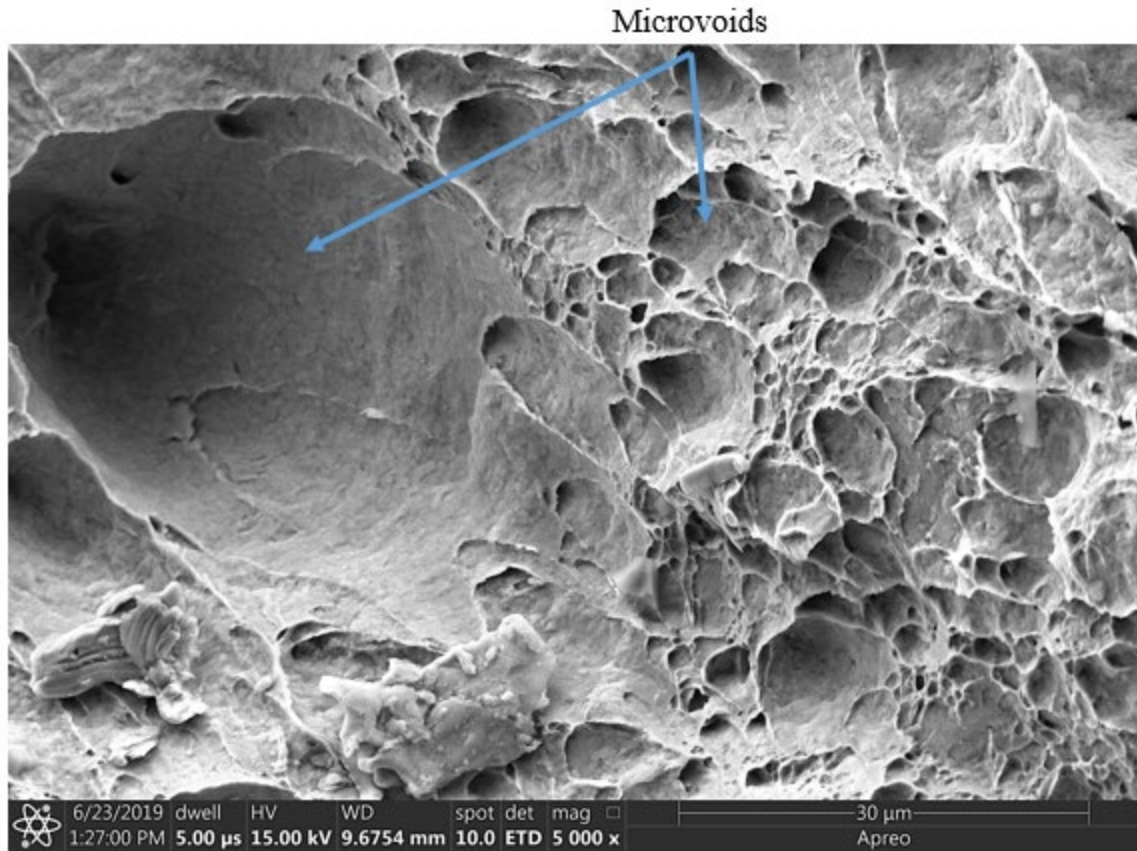


**Figure 39:** SEM fracture micrographs of Zn.

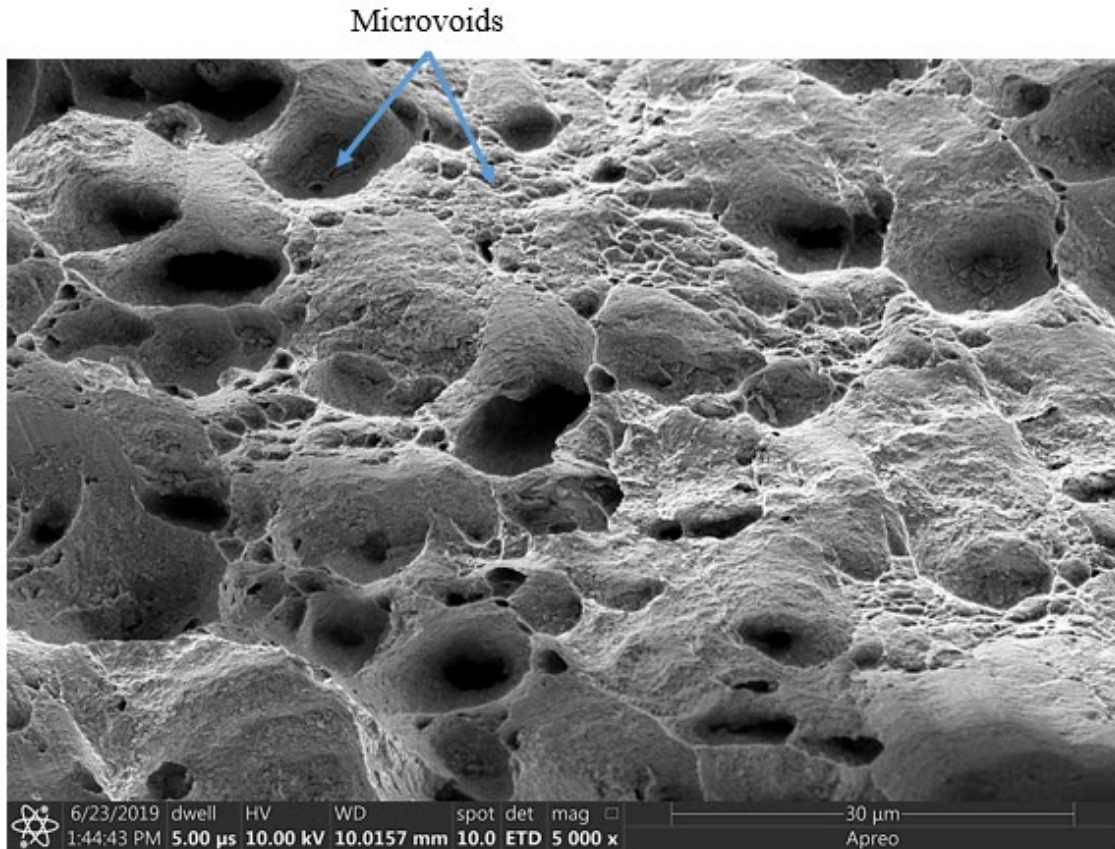


**Figure 40:** SEM fracture micrograph of Zn-3.5Cu.

Void nucleation in pure metals is hypothesized to occur due to vacancy condensation at dislocation dense sites, such as dislocation cell boundaries or lamellar cell block boundaries [177]. In alloys, voids nucleate at inclusions or second phase particles by decohesion or cracking [178]. Regardless of the nucleation process, void coalescence will induce internal microcracks, which grow due to an increased localized plastic strain by an applied tensile stress and eventually lead to ductile tearing [179]. As the voids coalesce and grow, the ligaments between voids thin and eventually locally fracture, forming small, cup-like ridges, the primary feature of ductile rupture [165]. The fracture surface observed in Figures 39 and 40 for pure Zn and Zn-3.5Cu is clearly ductile rupture, based on the dimpled surface and large, cup-like depressions. Dimples that are large are a result of enhanced ductility and severe plastic deformation [180].

While Zn-0.3Li exhibited similar ductile fracture and large elongation to failure, the fracture structure in Figure 41 is less pronounced compared to Zn and Zn-3.5Cu.

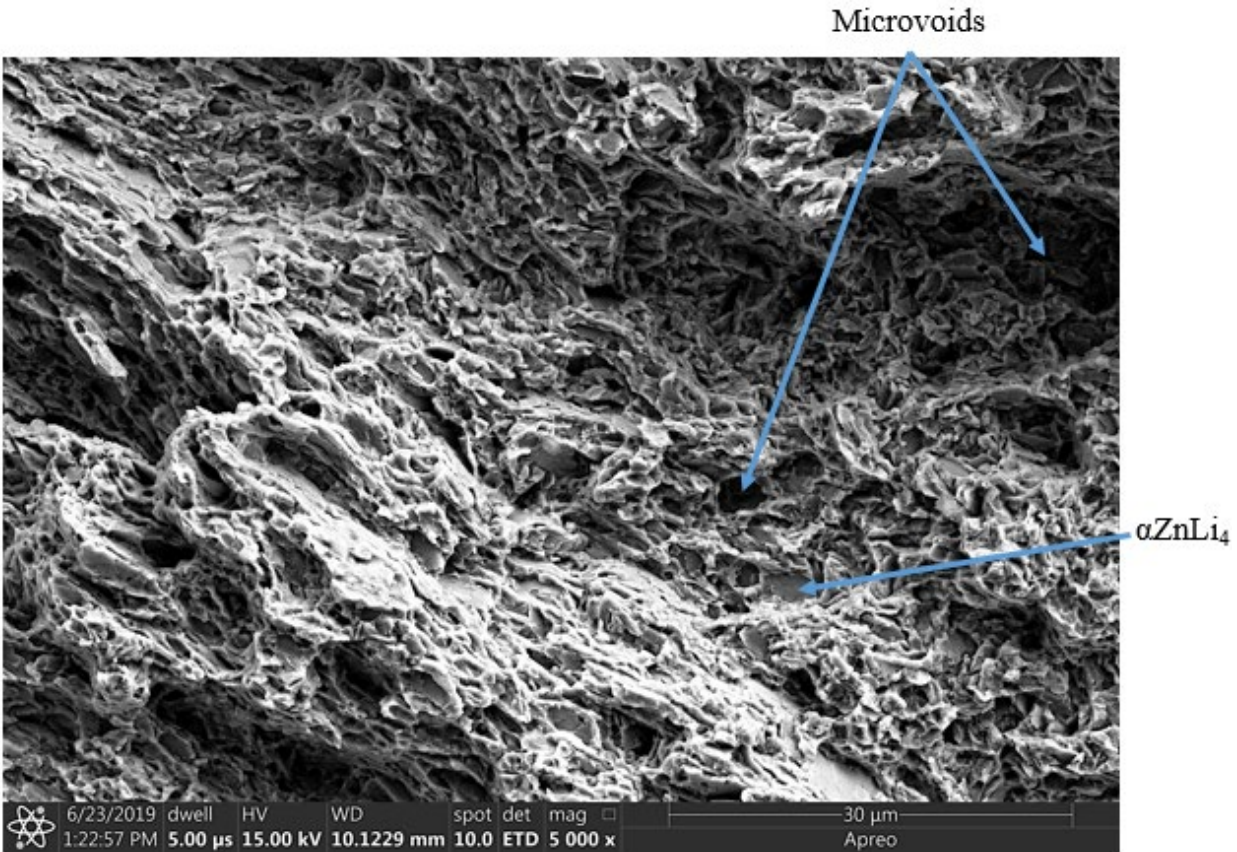


**Figure 41:** SEM fracture micrograph of Zn-0.3Li.

Konovalenko et al. [181] categorized dimple size into three types: individual small dimples, large dimples with smooth walls, and large dimples with small dimples covering the surface. The fracture structure of Zn-0.3Li is primarily made up of large dimples, the surface of which is covered by small dimples that are angled toward the direction of crack growth during fracture. Qin et al. [180] found that dimple size,  $D_d$ , is directly proportional to grain size,  $D$ , by  $D_d \propto D^{1/2}$ . By this relationship, small dimple formation can be attributed to the  $\alpha\text{LiZn}_4$  phase that is finely distributed throughout the  $\eta\text{Zn}$  matrix, observed in Figure 15. The  $\eta\text{Zn}$  phase is still a large

volume fraction compared to the studied ternary alloys, so large dimples, similarly observed in Figures 39 and 40, will form during plastic deformation.

A significant reduction in elongation was observed when both Li and Cu are added as alloying elements, which is highlighted by a stark change in deformation behavior and fracture structure, shown in Figure 42.

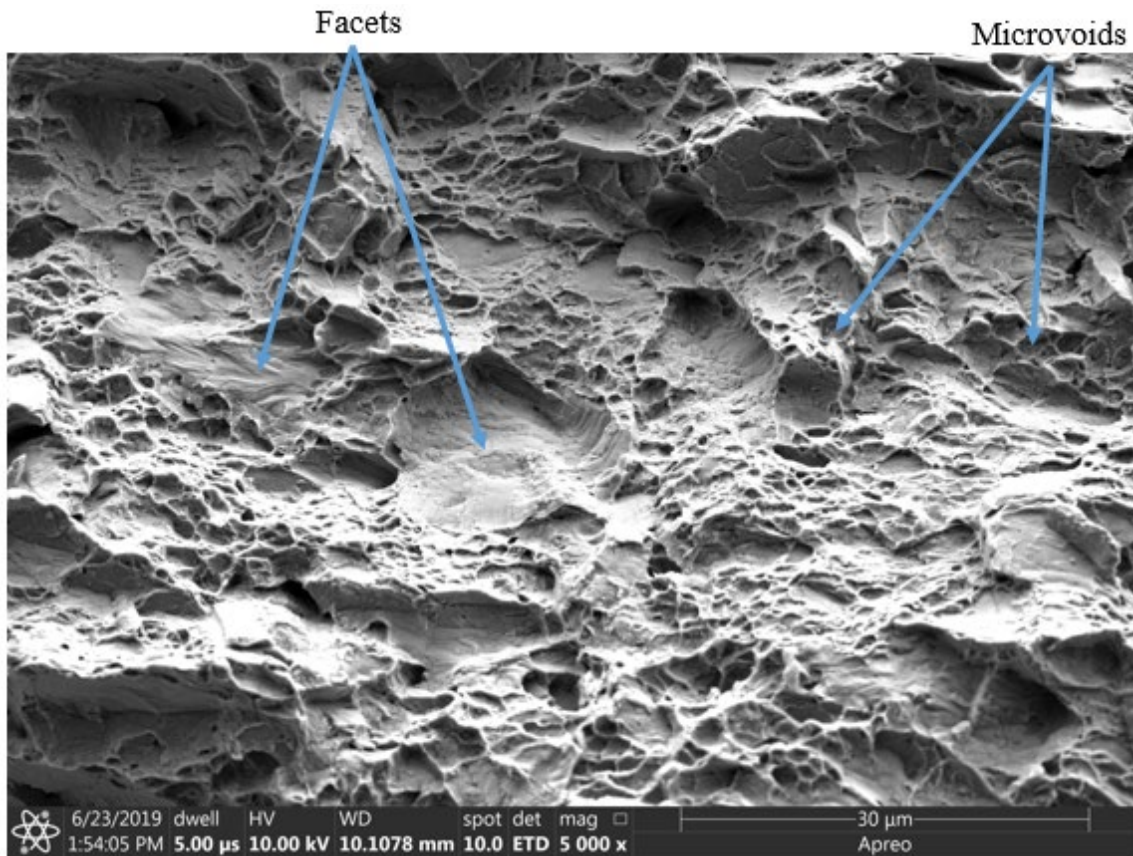


**Figure 42:** SEM fracture micrograph of Zn-0.3Li-2Cu.

The Zn-0.3Li-2Cu alloy exhibited small-sized dimples, representative of ductile rupture, as well as large flat regions. Flat facets with “river marking” or striations after fracture is traditionally a sign of transgranular brittle failure [165]. Transgranular fracture occurs when a crack grows through grains of different orientations along a particular slip plane due to limited allowable

plastic deformation. The “river markings” are formed when a crack crosses a grain boundary, as the crack tends to propagate on multiple planes in the new grain [182]. For hcp lattices, cleavage typically occurs on the (0001) basal plane in order to minimize shear strain, which has a high packing density and small interplanar spacing, although other planes are possible [182]. As the Cu content increases to 3.5 and 5 wt.%, the fracture mechanism continues to evolve, shown in Figures 43 and 44.

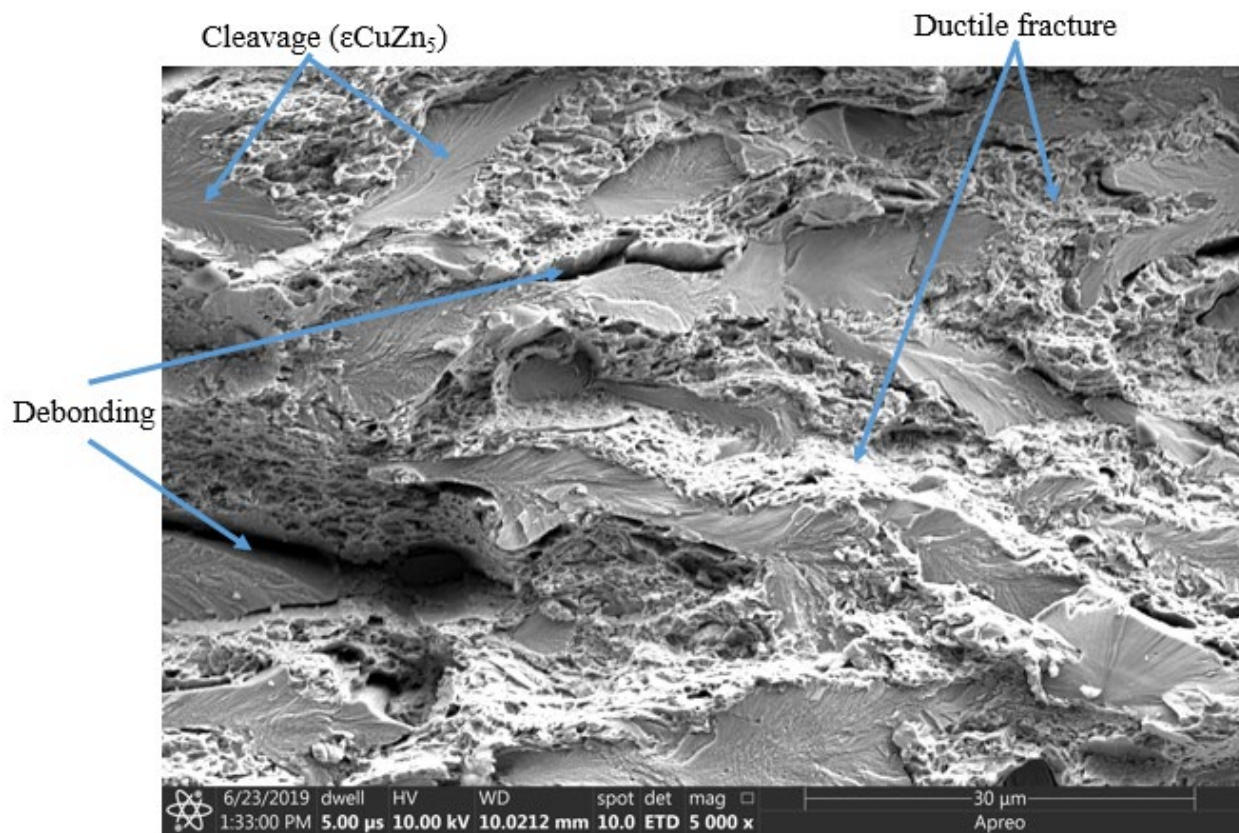


**Figure 43:** SEM fracture micrograph of Zn-0.3Li-3.5Cu.

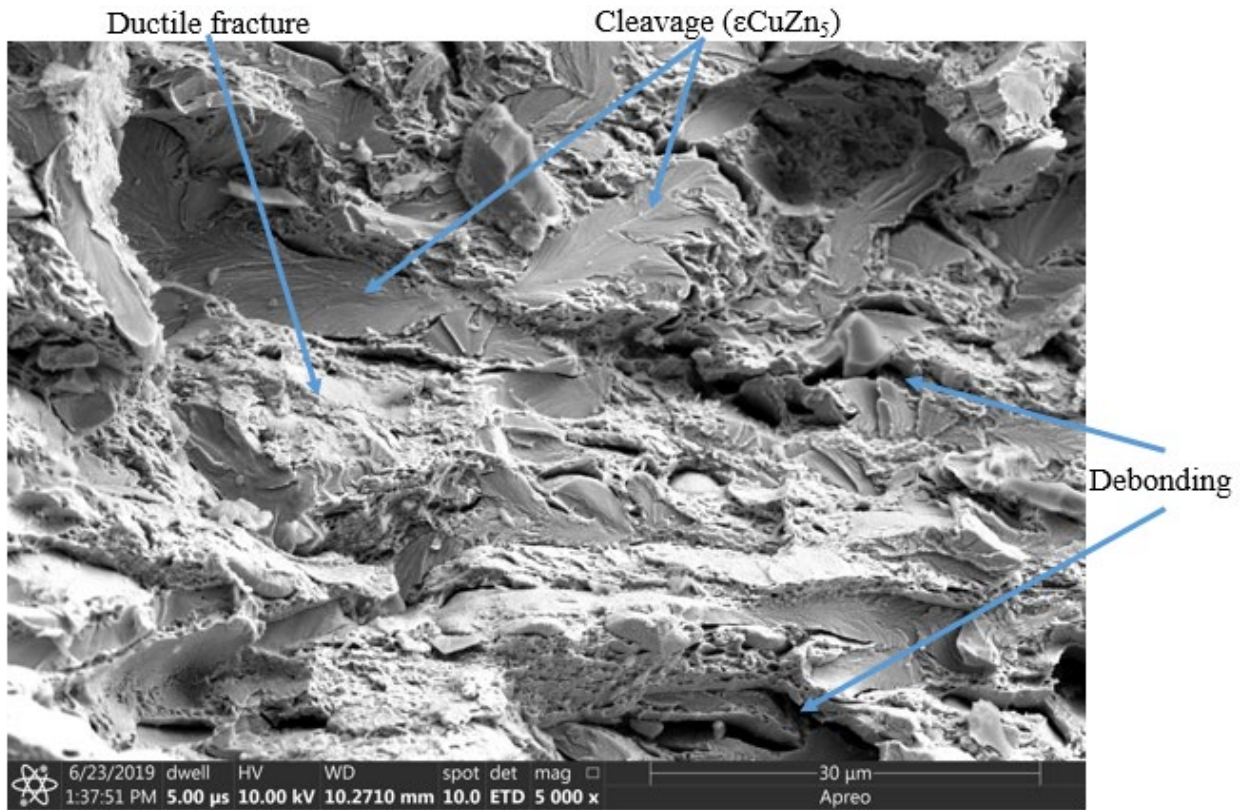


**Figure 44:** SEM fracture micrograph of Zn-0.3Li-5Cu.

After fracture in ternary alloys with elevated Cu content, the fracture mechanism is distinctly divided by phase region. The region with intergranular brittle fracture is the  $\epsilon\text{CuZn}_5$  phase, while the ductile dimpled region is a combination of  $\alpha\text{LiZn}_4$  and  $\eta\text{Zn}$ . This is confirmed through selective EDS analysis for Cu in Figure 45, where the Cu content (pink region) is segregated wholly within the brittle fracture facets. The teal regions are Zn, which is expectedly everywhere, while Li is not detectable with EDS. Nevertheless, one can assume that Li is present where Cu is not, since there is no chemical interaction between Li and Cu based on the phase diagram.

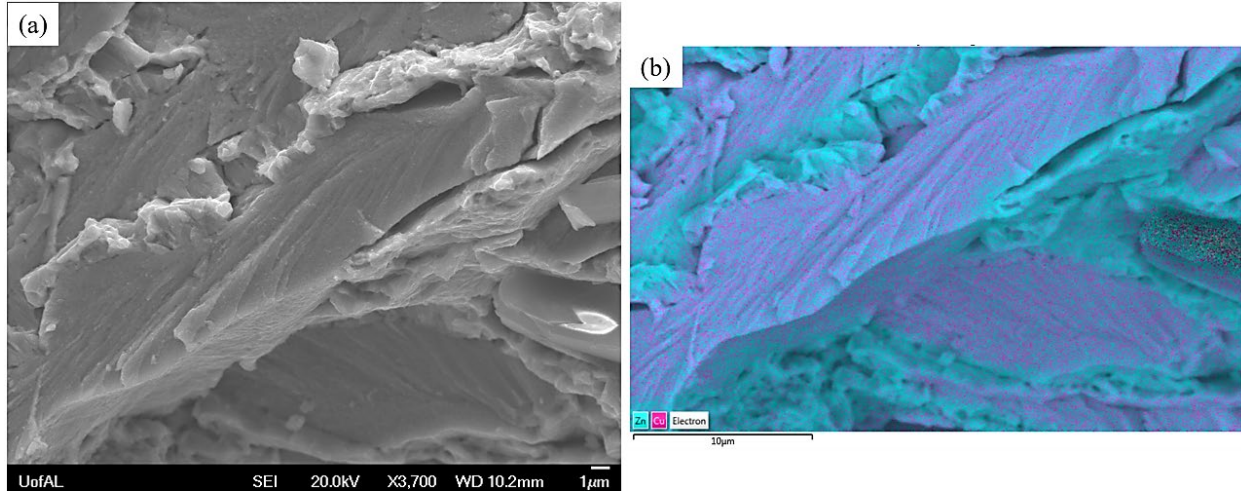


**Figure 45:** (a) SEM micrograph and (b) EDS analysis of Zn and Cu content of Zn-0.3Li-5Cu phase regions.

The overall change in mechanical behavior and fracture mechanism can be linked to crack propagation behavior and plastic deformation availability. Slip and twinning are the primary mechanisms of plastic deformation in ductile phases (i.e.  $\eta\text{Zn}$  and  $\alpha\text{LiZn}_4$ ). Based on tensile test results and fracture microstructure, when both Zn and  $\text{LiZn}_4$  are present, the  $\epsilon\text{CuZn}_5$  phase is brittle and the ability to slip is significantly reduced. Since plastic deformation is observed to be hindered in  $\epsilon\text{CuZn}_5$  for ternary alloys, cracks must only be able to either go through or around the  $\epsilon\text{CuZn}_5$  phase. Gall et al. [183] observed that in Al-Si alloys, small cracks will propagate differently based on the magnitude of the crack tip driving force, where driving force is proportional to the applied stress, illustrated in Figure 46. For particles or phase regions that are parallel to the direction of microcrack growth, the crack will travel along the interface of the matrix and second phase at a crack tip driving force below some critical magnitude. Since driving force is low, the elastic strain energy required to fracture large cross-sections of the brittle phase is not available. At a high driving force, the crack will fracture through the second phase as local strain energy increases. When the phase is aligned perpendicular to crack growth, the crack will go through regardless of driving force magnitude.

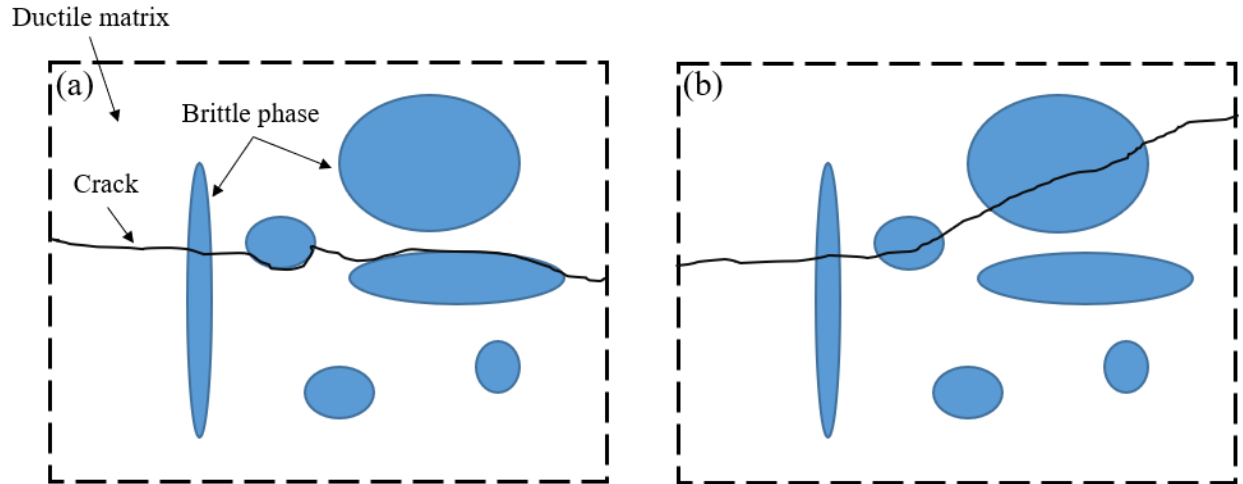


**Figure 46:** Schematic of crack propagation through two phase alloy with ductile matrix and brittle second phase with (a) low and (b) high crack tip driving force.

Since the samples were hot rolled, the majority of the  $\text{CuZn}_5$  regions are approximately parallel to the crack propagation direction observed during testing. As a tensile stress is first applied to the ternary alloy sample, the driving force is assumed to start at a low magnitude and crack propagation behavior will follow Figure 46a. Debonding between the  $\text{CuZn}_5$  and  $\text{Zn/LiZn}_4$  regions is evidence of this crack growth regime. Debonding and void coalescence by ductile rupture can be considered indistinguishable mechanisms during monotonic loading [183]. Therefore, debonding between  $\epsilon\text{CuZn}_5$  and  $\eta\text{Zn}$  will contribute to and accelerate the ductile rupture of the  $\eta\text{Zn}$  matrix. As voids coalesce and elastic strain increases due to decreased stress-affected cross-sectional area, the crack tip driving force will reach a critical magnitude. Cracking and transgranular brittle failure will initiate through the  $\text{CuZn}_5$  phase, illustrated in Figure 46b, ultimately leading to sudden catastrophic failure with minimal necking and lower elongation to failure since the  $\text{CuZn}_5$  phase comprises of 10-30% of the effective sample volume.

## 5.4 Cytotoxicity Testing

To evaluate the biocompatibility of Zn-Li-Cu alloys, the metabolic activity of NIH3T3 fibroblast cells were measured through indirect MTS testing for up to 7 days with different extract concentrations. Fibroblasts are a type of cell typically found in connective tissue and responsible for the repair of wounded tissue through synthesis of the extracellular matrix and collagen [184]. Results from the *in vitro* cytotoxicity testing of Zn, Zn-0.3Li-2Cu, Zn-0.3Li-3.5Cu, and Zn-0.3Li-5Cu are shown in Figure 47.

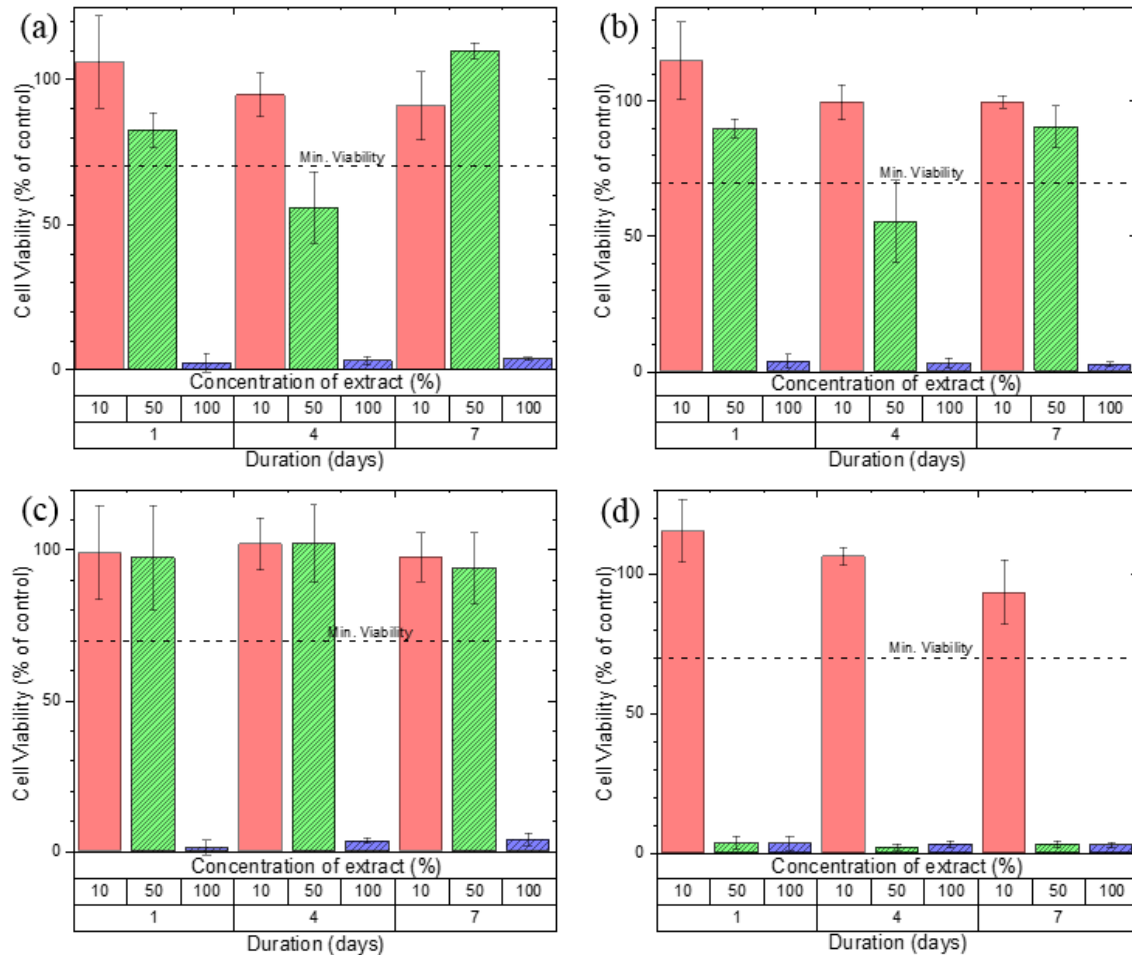


**Figure 47:** Cell viability of NIH3T3 cells on (a) pure Zn, (b) Zn-0.3Li-2Cu, (c) Zn-0.3Li-3.5Cu, and (d) Zn-0.3Li-5Cu substrate with respect to extraction concentration and duration.

Nontoxicity is defined as a cell viability greater than 70% with respect to the control sample. All selected alloys were found to be nontoxic at 10% extract concentration regardless of duration. At 50% concentration, Zn, Zn-0.3Li-2Cu, and Zn-0.3Li-3.5Cu are found generally nontoxic up to 7 days, while Zn-0.3Li-5Cu observed near complete cell death. The undiluted extracts of Zn and all ternary alloys can be considered toxic due to minimal cell viability below 10%. It is common for biodegradable metals to exhibit cytotoxicity at higher extract concentrations. A 100% extract test simulates the alloy in a static environment, which is unrealistic in the human body. Body fluid will normally flow, reducing any local concentration increase of dissolved metal ion from the alloy.

Optical micrographs of NIH3T3 fibroblast cells after incubation are compiled in Appendix V. Healthy fibroblasts normally exhibit a flat and elongated spindle shape when they are attached to a substrate during testing, which is observed for samples where nontoxicity is observed, in agreement with the negative control group [185]. For samples where near-zero cell viability was measured, only sparse circular-shaped cells are seen. Dead fibroblast cells have lost their shape, becoming spherical, and are not adhered to anything, floating in the incubated media [101].

Cell death is known to occur at critical concentrations for particular metal ions [186]. The assumption can be made that the majority of metal ions released into the extract are  $Zn^{2+}$  based on the corrosion work in this study. Additionally, Kubásek et al. [80] mentioned  $Zn^{2+}$  ion limitations of 80  $\mu M$  and 120  $\mu M$  for similar L929 and U-2 OS cell lines. Given the decrease in cell viability for all samples with increase of concentration from 50% to 100%, NIH3T3 has a similar sensitivity to Zn ion concentration. Similarly, Fowler et al. [187] reported a  $Cu^{2+}$  ion sensitivity at  $>9 \times 10^{-5}$  g/mL for MC3T3 osteoblast cells. Based on the viability decrease

observed between 3.5 and 5 wt.% Cu alloys at 50% extract concentration, a similar Cu ion sensitivity relationship likely exists for NIH3T3 cells.

With regard to comparability of these results, the majority of previous studies for Zn-Cu and Zn-Li alloys have exhibited acceptable cell viability at all extract concentrations, while some contrarily show toxicity at certain dilutions. Tang et al. [7] observed nontoxicity of EA.hy926 cell line for Zn-xCu (x = 1-4 wt.%) for 50% and 10% extracts, while 100% was toxic. Similarly, Zhou et al. [70] found good *in vivo* biocompatibility of Zn-0.8Cu in porcine coronary arteries up to 24 months. Initial *in vitro* and *in vivo* studies of Zn-Li by Zhao et al. [12,14] showed promising results of Zn-0.1Li after implantation in rat abdominal aorta. Zhang et al. [90] found nontoxic behavior of bone marrow mesenchymal stem cells for Zn-0.5Li at all dilutions after 5 days incubation. Alternatively, recent results on Zn-Li system by Guo et al. [188] and Li et al. [135] find significant cytotoxicity effects on the L929 cell line at various extraction concentrations. Although the ISO standard is used for cytotoxicity evaluation, differences between studies, especially for the Zn-Li system, highlight that results are likely significantly affected by cell line choice and alloy composition effecting the ion release behavior. While this study compares reasonably to the Zn-Cu and some Zn-Li studies and shows favorable cell viability at lower extract concentrations, further *in vitro* tests on Zn-Li-Cu alloys with other cell lines may be needed for a complete comparison and analysis.

## CHAPTER 6 - CONCLUSIONS

### 6.1 Feasibility Determination of Zn-Li-Cu Alloys

Through a casting and hot rolling method, novel Zn-0.3Li- $x$ Cu ( $x = 2, 3.5, 5$  wt. %) alloys were synthesized and evaluated for biodegradable medical device applications. XRD/EDS analysis and a simulated Zn-Li-Cu phase diagram both confirm the presence of  $\alpha$ LiZn<sub>4</sub> and  $\epsilon$ CuZn<sub>5</sub> with added Li and Cu content, respectively. No interactions or phases composed of both Li and Cu were observed. Optical microscopy revealed a texture parallel with the rolling direction from elongated intermetallic phases. From mechanical tensile tests, the selected ternary alloys observed an increase in yield strength to 273 MPa, ultimate tensile strength to 428 MPa, and hardness to 134 HV0.2, while elongation to failure was lowered to ~20% compared to pure Zn, Zn-0.3Li, and Zn-3.5Cu at ~51-59%. The heightened strength and hardness compared to an as-cast Zn is primarily attributed to grain boundary strengthening from hot-rolling and composite strengthening from formation of fiber-like intermetallic regions, with small contributions from solid solution and precipitation strengthening. Ductility was reduced in the ternary alloys due to reduction past a critical amount of  $\eta$ Zn between 0.771 and 0.666 phase fraction, promoting cracking through the stronger, more brittle intermetallic phases. The ternary alloys observed a distinct mixed ductile ( $\eta$ Zn and  $\alpha$ LiZn<sub>4</sub>) and brittle ( $\epsilon$ CuZn<sub>5</sub>) fracture mechanism from fracture surface micrographs. Catastrophic failure of the ternary alloys occurred near 20% elongation due to debonding and void coalescence at the interfaces between  $\epsilon$ CuZn<sub>5</sub> and the  $\eta$ Zn/ $\alpha$ LiZn<sub>4</sub> regions, promoting accelerated ductile rupture of the  $\eta$ Zn matrix, reaching to a critical crack tip

driving force and crack growth through the brittle  $\epsilon\text{CuZn}_5$  phase. The ductile  $\eta\text{Zn}$  phase fraction is theorized as a key parameter towards the amount of plastic deformation before fracture allowed in the bulk alloy.

*In vitro* immersion corrosion in HBSS showed a minimal difference between Zn and Zn-0.3Li-xCu alloys, where the weight loss corrosion rate decreased to below  $0.02 \text{ mm yr}^{-1}$  after 21 days. The probable corrosion products observed from EDS, FTIR, and XPS data include ZnO, Zn(OH)<sub>2</sub>, ZnCO<sub>3</sub>, Zn<sub>3</sub>(PO<sub>4</sub>)<sub>2</sub>, Zn<sub>5</sub>(CO<sub>3</sub>)<sub>2</sub>(OH)<sub>6</sub>, CaCO<sub>3</sub>, and Zn<sub>5</sub>(OH)<sub>8</sub>Cl<sub>2</sub>-H<sub>2</sub>O. Corrosion product species including Li or Cu were not observed, indicating preferential corrosion of the  $\eta\text{Zn}$  matrix during the first 100 days. The corrosion rate is inhibited by the formation of a plated zinc oxide layer on the surface of the alloy, with additional phosphate and carbonate compounds precipitating as agglomerates on the surface of the oxide layer. The oxide plate boundaries act as cracks, allowing for continual contact between the alloy and HBSS medium, promoting a continual diffusion of metal ions. While the oxide layer inhibited ion charge transfer quantified by EIS, the charge transfer resistance decreased with increasing thickness of ZnO, attributed to the natural semiconducting capabilities of zinc oxides. Evidence of pitting corrosion of the alloys was observed below the oxide layer, attributed to galvanic interactions between phases stimulated by the buildup of Cl<sup>-</sup> ions. After 100 days of *in vitro* immersion, the oxide layer had partially broken down, significantly revealing the underlying alloy surface. EIS results confirmed that after 100 days, there was no charge transfer resistance, a comparable state to the initial 0-day condition. It can be assumed that the corrosion rate would increase to  $\geq 0.03 \text{ mm yr}^{-1}$  based on the 5 day samples, mimicking the corrosion behavior when no resistive oxide layer is present.

The cytotoxicity tests of Zn-Li-Cu alloys show no cytotoxicity for 10% extract concentrations up to 7 days. Alloys with 2 and 3.5 wt.% Cu exhibit good biocompatibility at 50% extract, while an

increase to 5 wt.% Cu observed toxic cell behavior. All alloys were found to be cytotoxic when the extract was undiluted. Changes to cell viability are attributed to changes of released metal ion concentrations which is highly related to corrosion behavior of the alloy in body fluid solution. The results were comparable to most similar studies of Zn-Cu and Zn-Li binary alloys, although choice of cell line is a key factor towards cytotoxicity quantification.

Ultimately, these preliminary results show promise for the Zn-Li-Cu system based on good mechanical properties and low, stable corrosion behavior. The Zn-0.3Li-3.5Cu alloy met or exceeded all tested design requirements and is recommended for further study and optimization for stent applications. This work also highlights the importance of using a systematic approach for materials selection and development of stent alloys. While many literatures suggest alloy compositions and state general property trends, the fundamentals behind why alloys are favorable or not for each material property are often not discussed in detail. These fundamentals are critical for understanding what makes a particular alloy feasible for stent applications and gives good insight into future optimization and improvement.

## 6.2 Future Work

With regard to alloy synthesis optimization, improvements to the melting technique and nominal chemistry accuracy should include limiting vapor mass loss through environment control as well as development of quicker pouring techniques to reduce solid waste. The hot rolling method could be improved through better hot soaking temperature homogenization with a larger horizontal furnace, as well as faster rolling passes to reduce temperature loss while rolling and allow for more passes between soaking. These revisions would provide a more repeatable, controlled synthesis process and lower mechanical property and compositional variability.

While basic tests regarding strength and ductility were performed and met the given criteria, additional studies can be done to further optimize and improve the Zn-Li-Cu system. Tensile testing in the non-rolling direction can provide insight into the homogeneity of the alloy mechanical properties. High resolution XRD or EBSD can be completed to quantify changes in texture due to hot-rolling, as well as with alloying. Also, the mechanical properties of the LiZn<sub>4</sub> phase are unreported in literature; nanoindentation studies could provide useful mechanical data towards the strengthening and hardening contributions of LiZn<sub>4</sub>. Tensile tests post-immersion corrosion should be investigated to quantify the rate of change in mechanical behavior until complete mechanical degradation. Testing would require significant modifications to sample shape, size, and volume of solution. Additionally, current stent devices in the body not only undergo tensile stresses, but also strain hardening during implantation and use. Measuring strain hardening effects on thin samples (e.g. wires, stents, etc.) would establish a more complete analysis of mechanical behavior during implantation and balloon angioplasty.

While this study investigated corrosion behavior qualitatively after 21 days, additional long duration immersion corrosion studies could be completed in order to quantify the mass loss-based corrosion rate at 50 and 100 day time steps. The expected behavior based on this work would be an increase in corrosion rate between 50 and 100 days. This would help to confirm the proposed mechanisms as well as act as a comparison to other long-term studies.

The corrosion behavior is also related to the released ion concentration in extract medium during MTS cytotoxicity testing. Since ion concentration sensitivity is a key parameter toward the cell growth behavior, additional quantitative analysis could be helpful in optimizing alloy concentrations. Additionally, *in vitro* analysis of other cell lines, such as L929, can provide further comparison of biocompatibility to similar alloy studies. *In vivo* testing in animals

according to testing standards would also provide a greater level of confidence towards the feasibility of Zn-Li-Cu biodegradable alloys as it's a closer testing environment to the human body.

Finally, additional ternary chemistries should be pursued in order to optimize the studied properties. A critical amount of  $\eta$ Zn phase is hypothesized to exist between 0.666 and 0.771 volume fraction in a Zn-Li-Cu ternary alloy where ductility remains near 50% while strength is sufficient. Using the simulated phase diagram to find satisfactory chemistries and testing them will verify this theory and determine the maximum strength given a required elongation to failure. Due to the limitations of EDS, atom probe tomography can also be done to map the location of Li within the alloy (solid solubility in phases), providing additional insight to mechanical behavior and phase quantification. High resolution transmission electron microscopy could also be utilized to investigate the extent of substitutional solid solution behavior of Li and Cu in  $\eta$ Zn and compare to PANDAT calculations.

## REFERENCES

- [1] Y.F. Zheng, X.N. Gu, F. Witte, Biodegradable metals, *Mater. Sci. Eng. R Reports*. 77 (2014) 1–34.
- [2] M.I.Z. Ridzwan, S. Shuib, A.Y. Hassan, A.A. Shokri, M.N.M. Ibrahim, Problem of stress shielding and improvement to the hip implant designs: a review, *J. Med. Sci.* 7 (2007) 460–467.
- [3] G. Manivasagam, D. Dhinasekaran, A. Rajamanickam, Biomedical implants: corrosion and its prevention—a review., *Recent Patents Corros. Sci.* 2 (2010) 40–54.
- [4] M. Esmaily, J.E. Svensson, S. Fajardo, N. Birbilis, G.S. Frankel, S. Virtanen, R. Arrabal, S. Thomas, L.G. Johansson, Fundamentals and advances in magnesium alloy corrosion, *Prog. Mater. Sci.* 89 (2017) 92–193.
- [5] H. Li, Y. Zheng, L. Qin, Progress of biodegradable metals, *Prog. Nat. Sci. Mater. Int.* 24 (2014) 414–422.
- [6] G. Katarivas Levy, J. Goldman, E. Aghion, The prospects of zinc as a structural material for biodegradable implants—A review paper, *Metals (Basel)*. 7 (2017) 402.
- [7] Z. Tang, J. Niu, H. Huang, H. Zhang, J. Pei, J. Ou, G. Yuan, Potential biodegradable Zn-Cu binary alloys developed for cardiovascular implant applications, *J. Mech. Behav. Biomed. Mater.* 72 (2017) 182–191.
- [8] P.K. Bowen, J. Drelich, J. Goldman, Zinc exhibits ideal physiological corrosion behavior for bioabsorbable stents, *Adv. Mater.* 25 (2013) 2577–2582.
- [9] P. Trumbo, A.A. Yates, S. Schlicker, M. Poos, Dietary reference intakes: vitamin A, vitamin K, arsenic, boron, chromium, copper, iodine, iron, manganese, molybdenum, nickel, silicon, vanadium, and zinc, *J. Acad. Nutr. Diet.* 101 (2001) 294.
- [10] J. Niu, Z. Tang, H. Huang, J. Pei, H. Zhang, G. Yuan, W. Ding, Research on a Zn-Cu alloy as a biodegradable material for potential vascular stents application, *Mater. Sci. Eng. C*. 69 (2016) 407–413.
- [11] Z. Tang, H. Huang, J. Niu, L. Zhang, H. Zhang, J. Pei, J. Tan, G. Yuan, Design and characterizations of novel biodegradable Zn-Cu-Mg alloys for potential biodegradable implants, *Mater. Des.* 117 (2018) 67–79.

- [12] S. Zhao, C.T. McNamara, P.K. Bowen, N. Verhun, J.P. Braykovich, J. Goldman, J.W. Drelich, Structural characteristics and in vitro biodegradation of a novel Zn-Li alloy prepared by induction melting and hot rolling, *Metall. Mater. Trans. A.* 48 (2017) 1204–1215.
- [13] W. Yuan, D. Xia, Y. Zheng, X. Liu, S. Wu, B. Li, Y. Han, Z. Jia, D. Zhu, L. Ruan, others, Controllable biodegradation and enhanced osseointegration of ZrO<sub>2</sub>-nanofilm coated Zn-Li alloy: In vitro and in vivo studies, *Acta Biomater.* (2020).
- [14] S. Zhao, J.-M. Seitz, R. Eifler, H.J. Maier, R.J. Guillory II, E.J. Earley, A. Drelich, J. Goldman, J.W. Drelich, Zn-Li alloy after extrusion and drawing: structural, mechanical characterization, and biodegradation in abdominal aorta of rat, *Mater. Sci. Eng. C.* 76 (2017) 301–312.
- [15] G.N. Schrauzer, Lithium: occurrence, dietary intakes, nutritional essentiality, *J. Am. Coll. Nutr.* 21 (2002) 14–21.
- [16] P. Fattahi, G. Yang, G. Kim, M.R. Abidian, A review of organic and inorganic biomaterials for neural interfaces, *Adv. Mater.* 26 (2014) 1846–1885.
- [17] S. Borhani, S. Hassanajili, S.H.A. Tafti, S. Rabbani, Cardiovascular stents: overview, evolution, and next generation, *Prog. Biomater.* 7 (2018) 175–205.
- [18] X. Wang, S. Xu, S. Zhou, W. Xu, M. Leary, P. Choong, M. Qian, M. Brandt, Y.M. Xie, Topological design and additive manufacturing of porous metals for bone scaffolds and orthopaedic implants: A review, *Biomaterials.* 83 (2016) 127–141.
- [19] I.D. Papel, J. Frodel, G.R. Holt, W.F. Larrabee, N.E. Nachlas, S.S. Park, J.M. Sykes, D.M. Toriumi, *Facial plastic and reconstructive surgery*, Thieme New York, NY, 2002.
- [20] E.O. Martz, V.K. Goel, M.H. Pope, J.B. Park, Materials and design of spinal implants—a review, *J. Biomed. Mater. Res.* 38 (1997) 267–288.
- [21] T. Albrektsson, G. Zarb, P. Worthington, A.R. Eriksson, The long-term efficacy of currently used dental implants: a review and proposed criteria of success, *Int j Oral Maxillofac Implant.* 1 (1986) 11–25.
- [22] USA Department of Commerce, *The Medical Technology Industry in the United States: Overview*, Sel. USA. (n.d.). <https://www.selectusa.gov/medical-technology-industry-united-states#:~:text=Overview,to grow to %24208 billion.&text=U.S. medical device companies are,innovative and high technology products>.
- [23] Market Report, *Medical Device Market Report: Trends, Forecast and Competitive Analysis*, 2019.
- [24] R. Radha, D. Sreekanth, Insight of magnesium alloys and composites for orthopedic implant applications—a review, *J. Magnes. Alloy.* 5 (2017) 286–312.

- [25] M. Navarro, A. Michiardi, O. Castano, J.A. Planell, *Biomaterials in orthopaedics*, J. R. Soc. Interface. 5 (2008) 1137–1158.
- [26] P. Libby, P. Theroux, *Pathophysiology of coronary artery disease*, Circulation. 111 (2005) 3481–3488.
- [27] A. Gruntzig, D.A. Kumpe, *Technique of percutaneous transluminal angioplasty with the Gruntzig ballon catheter*, Am. J. Roentgenol. 132 (1979) 547–552.
- [28] RadiologyInfo.org, *Angioplasty and Vascular Stenting*, (2019). <https://www.radiologyinfo.org/en/info.cfm?pg=angioplasty> (accessed March 10, 2019).
- [29] P. Poncin, J. Proft, *Stent tubing: understanding the desired attributes*, in: Med. Device Mater. Proc. Mater. Process. Med. Devices Conf., 2004: pp. 253–259.
- [30] T. Schmidt, J.D. Abbott, *Coronary stents: history, design, and construction*, J. Clin. Med. 7 (2018) 126.
- [31] P.K. Bowen, E.R. Shearier, S. Zhao, R.J. Guillory, F. Zhao, J. Goldman, J.W. Drelich, *Biodegradable metals for cardiovascular stents: from clinical concerns to recent Zn-Alloys*, Adv. Healthc. Mater. 5 (2016) 1121–1140.
- [32] M. Moravej, D. Mantovani, *Biodegradable metals for cardiovascular stent application: interests and new opportunities*, Int. J. Mol. Sci. 12 (2011) 4250–4270.
- [33] G. Gottstein, *Strength and Deformation of Polycrystals*, in: Phys. Found. Mater. Sci., Springer, 2004: pp. 257–264.
- [34] G. Gottstein, *Dynamic Recrystallization*, in: Phys. Found. Mater. Sci., Springer, 2004: pp. 348–355.
- [35] K. Huang, R.E. Logé, *A review of dynamic recrystallization phenomena in metallic materials*, Mater. Des. 111 (2016) 548–574.
- [36] Y. Yun, Z. Dong, N. Lee, Y. Liu, D. Xue, X. Guo, J. Kuhlmann, A. Doepke, H.B. Halsall, W. Heineman, others, *Revolutionizing biodegradable metals*, Mater. Today. 12 (2009) 22–32.
- [37] F. Witte, *The history of biodegradable magnesium implants: a review*, Acta Biomater. 6 (2010) 1680–1692.
- [38] M. Schinhammer, A.C. Hänzi, J.F. Löffler, P.J. Uggowitzer, *Design strategy for biodegradable Fe-based alloys for medical applications*, Acta Biomater. 6 (2010) 1705–1713.
- [39] K. Prasad, O. Bazaka, M. Chua, M. Rochford, L. Fedrick, J. Spoor, R. Symes, M. Tieppo, C. Collins, A. Cao, others, *Metallic biomaterials: Current challenges and opportunities*, Materials (Basel). 10 (2017) 884.

- [40] D. Pierson, J. Edick, A. Tauscher, E. Pokorney, P. Bowen, J. Gelbaugh, J. Stinson, H. Getty, C.H. Lee, J. Drelich, others, A simplified in vivo approach for evaluating the bioabsorbable behavior of candidate stent materials, *J. Biomed. Mater. Res. Part B Appl. Biomater.* 100 (2012) 58–67.
- [41] R.J. Werkhoven, W.H. Sillekens, J. Van Lieshout, Processing aspects of magnesium alloy stent tube, in: *Magnes. Technol.* 2011, Springer, 2011: pp. 419–424.
- [42] R. Bonan, A.W. Asgar, *Biodegradable Stents: Where Are We in 2009?*, (2009).
- [43] N. A Nawawi, A. SF Alqap, I. Sopyan, Recent progress on hydroxyapatite-based dense biomaterials for load bearing bone substitutes, *Recent Patents Mater. Sci.* 4 (2011) 63–80.
- [44] D. Apelian, M. Paliwal, D.C. Herrschaft, Casting with zinc alloys, *Jom.* 33 (1981) 12–20.
- [45] G. Li, H. Yang, Y. Zheng, X.-H. Chen, J.-A. Yang, D. Zhu, L. Ruan, K. Takashima, Challenges in the use of zinc and its alloys as biodegradable metals: perspective from biomechanical compatibility, *Acta Biomater.* (2019).
- [46] U.S. Geological Survey, *Zinc Mineral Commodity Summary*, 2020. <https://pubs.usgs.gov/periodicals/mcs2020/mcs2020-zinc.pdf>.
- [47] M.J. Jackson, *Physiology of zinc: general aspects*, in: *Zinc Hum. Biol.*, Springer, 1989: pp. 1–14.
- [48] D.A. Jones, *Electrode Potentials*, in: *Princ. Prev. Corros.*, 2nd ed., Prentice Hall, 1996: p. 44.
- [49] D. Bian, W. Zhou, Y. Liu, N. Li, Y. Zheng, Z. Sun, Fatigue behaviors of HP-Mg, Mg--Ca and Mg--Zn--Ca biodegradable metals in air and simulated body fluid, *Acta Biomater.* 41 (2016) 351–360.
- [50] L. Elkaïam, O. Hakimi, E. Aghion, Stress Corrosion and Corrosion Fatigue of Biodegradable Mg-Zn-Nd-Y-Zr Alloy in In-Vitro Conditions, *Metals (Basel)*. 10 (2020) 791.
- [51] F.E. Goodwin, L.H. Kallien, W. Leis, Interaction of Creep and Ageing Behaviors in Zinc Die Castings, (2016).
- [52] H. Jin, S. Zhao, R. Guillory, P.K. Bowen, Z. Yin, A. Griebel, J. Schaffer, E.J. Earley, J. Goldman, J.W. Drelich, Novel high-strength, low-alloys Zn-Mg (< 0.1 wt.% Mg) and their arterial biodegradation, *Mater. Sci. Eng. C*. 84 (2018) 67–79.
- [53] J.C.T. Farge, W.M. Williams, The recrystallization behaviour of zinc alloys containing magnesium, cadmium, copper, silver, lead and iron, *Can. Metall. Q.* 5 (1966) 265–272.
- [54] United States Geological Survey, *Zinc Statistics and Information*, (n.d.). <https://www.usgs.gov/centers/nmic/zinc-statistics-and-information>.

- [55] M.G. Soni, S.M. White, W.G. Flamm, G.A. Burdock, Safety evaluation of dietary aluminum, *Regul. Toxicol. Pharmacol.* 33 (2001) 66–79.
- [56] P.K. Krajewski, A.L. Greer, W.K. Krajewski, Main Directions of Recent Works on Al-Zn-Based Alloys for Foundry Engineering, *J. Mater. Eng. Perform.* 28 (2019) 3986–3993.
- [57] W.R. Osorio, C.A. Santos, J.M. V Quaresma, A. Garcia, Mechanical properties as a function of thermal parameters and microstructure of Zn--Al castings, *J. Mater. Process. Technol.* 143 (2003) 703–709.
- [58] A. Pola, M. Tocci, F.E. Goodwin, Review of Microstructures and Properties of Zinc Alloys, *Metals (Basel)*. 10 (2020) 253.
- [59] A.E. Ares, L.M. Gassa, Corrosion susceptibility of Zn--Al alloys with different grains and dendritic microstructures in NaCl solutions, *Corros. Sci.* 59 (2012) 290–306.
- [60] W.R. Osório, C.M. Freire, A. Garcia, The effect of the dendritic microstructure on the corrosion resistance of Zn--Al alloys, *J. Alloys Compd.* 397 (2005) 179–191.
- [61] A. Flynn, The role of dietary calcium in bone health, *Proc. Nutr. Soc.* 62 (2003) 851–858.
- [62] Y. Jun, X. Wang, M. Jiang, W. Wang, Effect of calcium treatment on non-metallic inclusions in ultra-low oxygen steel refined by high basicity high Al<sub>2</sub>O<sub>3</sub> slag, *J. Iron Steel Res. Int.* 18 (2011) 8–14.
- [63] S.S.S. Kumari, R.M. Pillai, B.C. Pai, Role of calcium in aluminium based alloys and composites, *Int. Mater. Rev.* 50 (2005) 216–238.
- [64] C.S. Lakshmi, J.E. Manders, D.M. Rice, Structure and properties of lead--calcium--tin alloys for battery grids, *J. Power Sources.* 73 (1998) 23–29.
- [65] S. Wasiur-Rahman, M. Medraj, Critical assessment and thermodynamic modeling of the binary Mg--Zn, Ca--Zn and ternary Mg--Ca--Zn systems, *Intermetallics.* 17 (2009) 847–864.
- [66] H.F. Li, X.H. Xie, Y.F. Zheng, Y. Cong, F.Y. Zhou, K.J. Qiu, X. Wang, S.H. Chen, L. Huang, L. Tian, others, Development of biodegradable Zn-1X binary alloys with nutrient alloying elements Mg, Ca and Sr, *Sci. Rep.* 5 (2015) 10719.
- [67] V. Desai, S.G. Kaler, Role of copper in human neurological disorders, *Am. J. Clin. Nutr.* 88 (2008) 855S--858S.
- [68] J.R. Davis, others, *Copper and copper alloys*, ASM international, 2001.
- [69] B. Predel, Cu-Zn (Copper-Zinc), in: *Landolt-Börnstein - Gr. IV Phys. Chem. - Cr-Cs--Cu-Zr*, Springer, 1994: pp. 1–11.
- [70] C. Zhou, H.-F. Li, Y.-X. Yin, Z.-Z. Shi, T. Li, X.-Y. Feng, J.-W. Zhang, C.-X. Song, X.-S.

- Cui, K.-L. Xu, others, Long-term in vivo study of biodegradable Zn-Cu stent: A 2-year implantation evaluation in porcine coronary artery, *Acta Biomater.* 97 (2019) 657–670.
- [71] B. Müller-Oerlinghausen, W. Felber, A. Berghöfer, E. Lauterbach, B. Ahrens, The impact of lithium long-term medication on suicidal behavior and mortality of bipolar patients, *Arch. Suicide Res.* 9 (2005) 307–319.
- [72] Y. Liang, Z. Du, C. Guo, C. Li, Thermodynamic modeling of the Li--Zn system, *J. Alloys Compd.* 455 (2008) 236–242.
- [73] H. Okamoto, Li-Zn (Lithium-Zinc), *J. Phase Equilibria Diffus.* 33 (2012) 345.
- [74] S. Zhu, C. Wu, G. Li, Y. Zheng, J.-F. Nie, Microstructure, mechanical properties and creep behaviour of extruded Zn-xLi (x= 0.1, 0.3 and 0.4) alloys for biodegradable vascular stent applications, *Mater. Sci. Eng. A.* 777 (2020) 139082.
- [75] R.K. Rude, Physiology of magnesium metabolism and the important role of magnesium in potassium deficiency, *Am. J. Cardiol.* 63 (1989) G31--G34.
- [76] A.M. Uwitonze, M.S. Razzaque, Role of magnesium in vitamin D activation and function, *J Am Osteopat. Assoc.* 118 (2018) 181–189.
- [77] G. Paolisso, A. Scheen, F. d’Onofrio, P. Lefebvre, Magnesium and glucose homeostasis, *Diabetologia.* 33 (1990) 511–514.
- [78] P. Ghosh, M.D. Mezbahul-Islam, M. Medraj, Critical assessment and thermodynamic modeling of Mg--zn, Mg--sn, Sn--Zn and Mg--Sn--Zn systems, *Calphad.* 36 (2012) 28–43.
- [79] H. Gong, K. Wang, R. Strich, J.G. Zhou, In vitro biodegradation behavior, mechanical properties, and cytotoxicity of biodegradable Zn--Mg alloy, *J. Biomed. Mater. Res. Part B Appl. Biomater.* 103 (2015) 1632–1640.
- [80] J. Kubásek, D. Vojtěch, E. Jablonská, I. Pospěšilová, J. Lipov, T. Ruml, Structure, mechanical characteristics and in vitro degradation, cytotoxicity, genotoxicity and mutagenicity of novel biodegradable Zn--Mg alloys, *Mater. Sci. Eng. C.* 58 (2016) 24–35.
- [81] K. Mijndonckx, N. Leys, J. Mahillon, S. Silver, R. Van Houdt, Antimicrobial silver: uses, toxicity and potential for resistance, *Biometals.* 26 (2013) 609–621.
- [82] J.M. Corrêa, M. Mori, H.L. Sanches, A.D. da Cruz, E. Poiate, I.A.V.P. Poiate, Silver nanoparticles in dental biomaterials, *Int. J. Biomater.* 2015 (2015).
- [83] T. Gomez-Acebo, Thermodynamic assessment of the Ag-Zn system, *Calphad.* 22 (1998) 203–220.
- [84] M. Sikora-Jasinska, E. Mostaed, A. Mostaed, R. Beanland, D. Mantovani, M. Vedani, Fabrication, mechanical properties and in vitro degradation behavior of newly developed

- ZnAg alloys for degradable implant applications, *Mater. Sci. Eng. C*. 77 (2017) 1170–1181.
- [85] P. Li, C. Schille, E. Schweizer, F. Rupp, A. Heiss, C. Legner, U.E. Klotz, J. Geis-Gerstorfer, L. Scheideler, Mechanical characteristics, in vitro degradation, cytotoxicity, and antibacterial evaluation of Zn-4.0 Ag alloy as a biodegradable material, *Int. J. Mol. Sci.* 19 (2018) 755.
- [86] S.P. Nielsen, The biological role of strontium, *Bone*. 35 (2004) 583–588.
- [87] S.G. Hibbins, Strontium and strontium compounds, *Kirk-Othmer Encycl. Chem. Technol.* (2000).
- [88] P.J. Spencer, A.D. Pelton, Y.-B. Kang, P. Chartrand, C.D. Fuerst, Thermodynamic assessment of the Ca--Zn, Sr--Zn, Y--Zn and Ce--Zn systems, *Calphad*. 32 (2008) 423–431.
- [89] H. Yang, B. Jia, Z. Zhang, X. Qu, G. Li, W. Lin, D. Zhu, K. Dai, Y. Zheng, Alloying design of biodegradable zinc as promising bone implants for load-bearing applications, *Nat. Commun.* 11 (2020) 1–16.
- [90] Y. Zhang, Y. Lu, X. Xu, L. Chen, T. Xiao, X. Luo, Y. Yan, D. Li, Y. Dai, K. Yu, Microstructure, Corrosion Behaviors in Different Simulated Body Fluids and Cytotoxicity of Zn--Li Alloy as Biodegradable Material, *Mater. Trans.* 60 (2019) 583–586.
- [91] National Institutes of Health: Office of Dietary Supplements, Zinc: Fact Sheet for Health Professionals, (2020). <https://ods.od.nih.gov/factsheets/Zinc-HealthProfessional/#en2>.
- [92] National Institutes of Health: Office of Dietary Supplements, Calcium: Fact Sheet for Consumers, (2019). <https://ods.od.nih.gov/factsheets/Calcium-Consumer/>.
- [93] National Institutes of Health: Office of Dietary Supplements, Copper: Fact Sheet for Health Professionals, (2020). <https://ods.od.nih.gov/factsheets/Copper-HealthProfessional/>.
- [94] European Chemicals Agency, Lithium Hydroxide Basic toxicokinetics, (2010). <https://echa.europa.eu/registration-dossier/-/registered-dossier/14855/7/2/2>.
- [95] B. Mehus, J. LeRoy, Acute and Chronic Lithium Toxicity, (2016). <https://www.acep.org/how-we-serve/sections/toxicology/news/august-2016/acute-and-chronic-lithium-toxicity/>.
- [96] National Institutes of Health: Office of Dietary Supplements, Magnesium: Fact Sheet for Consumers, (2020). <https://ods.od.nih.gov/factsheets/Magnesium-Consumer/#howmuch> (accessed January 9, 2020).
- [97] P.L. Drake, K.J. Hazelwood, Exposure-related health effects of silver and silver compounds: a review, *Ann. Occup. Hyg.* 49 (2005) 575–585.

- [98] C.T. Price, J.R. Langford, F.A. Liporace, Essential nutrients for bone health and a review of their availability in the average North American diet, *Open Orthop. J.* 6 (2012) 143.
- [99] A.S. Prasad, A. Miale Jr, Z. Farid, H.H. Sandstead, A.R. Schulert, others, Zinc metabolism in patients with the syndrome of iron deficiency anemia, hepatosplenomegaly, dwarfism, and hypogonadism., *J. Lab. Clin. Med.* 61 (1963) 537–549.
- [100] N. Roohani, R. Hurrell, R. Kelishadi, R. Schulin, Zinc and its importance for human health: An integrative review, *J. Res. Med. Sci. Off. J. Isfahan Univ. Med. Sci.* 18 (2013) 144.
- [101] P. Li, C. Schille, E. Schweizer, E. Kimmerle-Müller, F. Rupp, A. Heiss, C. Legner, U.E. Klotz, J. Geis-Gerstorfer, L. Scheideler, Selection of extraction medium influences cytotoxicity of zinc and its alloys, *Acta Biomater.* 98 (2019) 235–245.
- [102] C. Wang, H.T. Yang, X. Li, Y.F. Zheng, In vitro evaluation of the feasibility of commercial Zn alloys as biodegradable metals, *J. Mater. Sci. Technol.* 32 (2016) 909–918.
- [103] M. Bost, S. Houdart, M. Oberli, E. Kalonji, J.-F. Huneau, I. Margaritis, Dietary copper and human health: Current evidence and unresolved issues, *J. Trace Elem. Med. Biol.* 35 (2016) 107–115.
- [104] M. Gitlin, Lithium side effects and toxicity: prevalence and management strategies, *Int. J. Bipolar Disord.* 4 (2016) 1–10.
- [105] Y.-X. Yin, C. Zhou, Y.-P. Shi, Z.-Z. Shi, T.-H. Lu, Y. Hao, C.-H. Liu, X. Wang, H.-J. Zhang, L.-N. Wang, Hemocompatibility of biodegradable Zn-0.8 wt%(Cu, Mn, Li) alloys, *Mater. Sci. Eng. C.* 104 (2019) 109896.
- [106] S.H. Duda, J. Wiskirchen, G. Tepe, M. Bitzer, T.W. Kaulich, D. Stoeckel, C.D. Claussen, Physical properties of endovascular stents: an experimental comparison, *J. Vasc. Interv. Radiol.* 11 (2000) 645–654.
- [107] D.C. Zipperian, *Metallographic Handbook*, (2011) 196–199.  
<http://www.metallographic.com/Brochures/Met-Manual-2b.pdf>.
- [108] NACE International, NACE TM0169/G31-12a Standard Guide for Laboratory Immersion Corrosion Testing of Metals, (2012) 1–9.
- [109] ISO, 19007:2018 Nanotechnologies - In vitro MTS assay for measuring the cytotoxic effect of nanoparticles, *Int. Organ. Stand. Geneva.* (2018).
- [110] E8/E8M-16a Standard Test Methods for Tension Testing of Metallic Materials, (2017) 1–4.
- [111] E384-17 Standard Test Method for Microindentation Hardness of Materials, (2017) 1–9.
- [112] M. Schmid, Vapor Pressure Calculator, (2018).

[https://www.iap.tuwien.ac.at/www/surface/vapor\\_pressure](https://www.iap.tuwien.ac.at/www/surface/vapor_pressure).

- [113] D. Li, S. Fürtauer, H. Flandorfer, D.M. Cupid, Thermodynamic assessment of the Cu--Li system and prediction of enthalpy of mixing of Cu--Li--Sn liquid alloys, *Calphad*. 53 (2016) 105–115.
- [114] C. Guo, Y. Liang, C. Li, Z. Du, Thermodynamic description of the Al--Li--Zn system, *Calphad*. 35 (2011) 54–65.
- [115] W. Gierlotka, S. Chen, Thermodynamic descriptions of the Cu--Zn system, *J. Mater. Res.* 23 (2008) 258–263.
- [116] B. Sundman, I. Ansara, The Gulliver--Scheil method for the calculation of solidification paths, in: *SGTE Caseb.*, Elsevier, 2008: pp. 343–346.
- [117] D. Vojtěch, J. Kubásek, J. Šerák, P. Novák, Mechanical and corrosion properties of newly developed biodegradable Zn-based alloys for bone fixation, *Acta Biomater.* 7 (2011) 3515–3522.
- [118] X. Liu, J. Sun, F. Zhou, Y. Yang, R. Chang, K. Qiu, Z. Pu, L. Li, Y. Zheng, Micro-alloying with Mn in Zn--Mg alloy for future biodegradable metals application, *Mater. Des.* 94 (2016) 95–104.
- [119] G.K. Levy, A. Kafri, Y. Ventura, A. Leon, R. Vago, J. Goldman, E. Aghion, Surface stabilization treatment enhances initial cell viability and adhesion for biodegradable zinc alloys, *Mater. Lett.* 248 (2019) 130–133.
- [120] C. Xiao, L. Wang, Y. Ren, S. Sun, E. Zhang, C. Yan, Q. Liu, X. Sun, F. Shou, J. Duan, others, Indirectly extruded biodegradable Zn-0.05 wt% Mg alloy with improved strength and ductility: In vitro and in vivo studies, *J. Mater. Sci. Technol.* 34 (2018) 1618–1627.
- [121] P.K. Bowen, J. Drelich, J. Goldman, Magnesium in the murine artery: Probing the products of corrosion, *Acta Biomater.* 10 (2014) 1475–1483.
- [122] L. Berzina-Cimdina, N. Borodajenko, Research of calcium phosphates using Fourier transform infrared spectroscopy, *Infrared Spectrosc. Sci. Eng. Technol.* 12 (2012) 251–263.
- [123] I.R. Gibson, W. Bonfield, Preparation and characterization of magnesium/carbonate co-substituted hydroxyapatites, *J. Mater. Sci. Mater. Med.* 13 (2002) 685–693.
- [124] E. Mostaed, M. Sikora-Jasinska, A. Mostaed, S. Loffredo, A.G. Demir, B. Previtali, D. Mantovani, R. Beanland, M. Vedani, Novel Zn-based alloys for biodegradable stent applications: design, development and in vitro degradation, *J. Mech. Behav. Biomed. Mater.* 60 (2016) 581–602.
- [125] B.V. Crist, Volume 2: Commercially Pure Binary Oxides, in: *Handbooks Monochromatic XPS Spectra*, XPS International LLC, 2004: pp. 43–49.

- [126] J. Winiarski, W. Tylus, K. Winiarska, I. Szczygieł, B. Szczygieł, XPS and FT-IR characterization of selected synthetic corrosion products of zinc expected in neutral environment containing chloride ions, *J. Spectrosc.* 2018 (2018).
- [127] M. Ni, B.D. Ratner, Differentiating calcium carbonate polymorphs by surface analysis techniques—an XPS and TOF-SIMS study, *Surf. Interface Anal. An Int. J. Devoted to Dev. Appl. Tech. Anal. Surfaces, Interfaces Thin Film.* 40 (2008) 1356–1361.
- [128] H. Dong, J. Zhou, S. Virtanen, Fabrication of ZnO nanotube layer on Zn and evaluation of corrosion behavior and bioactivity in view of biodegradable applications, *Appl. Surf. Sci.* 494 (2019) 259–265.
- [129] Q. Yang, L. Chen, J. Xu, Y. Gong, L. Deng, C. Chen, Study of the corrosion and surface film growth on AZ63 magnesium alloy in MgSO<sub>4</sub> solution, *J. Electrochem. Soc.* 164 (2017) C324.
- [130] L. He, G. Dong, C. Deng, Effects of strontium substitution on the phase transformation and crystal structure of calcium phosphate derived by chemical precipitation, *Ceram. Int.* 42 (2016) 11918–11923.
- [131] N.T. Mai, T.T. Thuy, D.M. Mott, S. Maenosono, Chemical synthesis of blue-emitting metallic zinc nano-hexagons, *CrystEngComm.* 15 (2013) 6606–6610.
- [132] D.L. Felker, P.M.A. Sherwood, Zinc phosphate (Zn<sub>3</sub>(PO<sub>4</sub>)<sub>2</sub>) by XPS, *Surf. Sci. Spectra.* 9 (2002) 106–113.
- [133] Y. Zhou, J. Peng, M. Wang, J. Mo, C. Deng, M. Zhu, Tribochemical Behavior of Pure Magnesium During Sliding Friction, *Metals (Basel).* 9 (2019) 311.
- [134] A.P. Savintsev, Y.O. Gavasheli, Z.K. Kalazhokov, K.K. Kalazhokov, X-ray photoelectron spectroscopy studies of the sodium chloride surface after laser exposure, in: *J. Phys. Conf. Ser.* 2016: p. 12118.
- [135] Z. Li, Z.-Z. Shi, Y. Hao, H.-F. Li, H.-J. Zhang, X.-F. Liu, L.-N. Wang, Insight into role and mechanism of Li on the key aspects of biodegradable ZnLi alloys: Microstructure evolution, mechanical properties, corrosion behavior and cytotoxicity, *Mater. Sci. Eng. C.* (2020) 111049.
- [136] Y. Zhang, Y. Yan, X. Xu, Y. Lu, L. Chen, D. Li, Y. Dai, Y. Kang, K. Yu, Investigation on the microstructure, mechanical properties, in vitro degradation behavior and biocompatibility of newly developed Zn-0.8% Li-(Mg, Ag) alloys for guided bone regeneration, *Mater. Sci. Eng. C.* 99 (2019) 1021–1034.
- [137] Y. Lu, A.R. Bradshaw, Y.L. Chiu, I.P. Jones, Effects of secondary phase and grain size on the corrosion of biodegradable Mg--Zn--Ca alloys, *Mater. Sci. Eng. C.* 48 (2015) 480–486.
- [138] W.R. Osório, C. Brito, L.C. Peixoto, A. Garcia, Electrochemical behavior of Zn-rich Zn--

- Cu peritectic alloys affected by macrosegregation and microstructural array, *Electrochim. Acta.* 76 (2012) 218–228.
- [139] B.-A. Mei, O. Munteshari, J. Lau, B. Dunn, L. Pilon, Physical interpretations of Nyquist plots for EDLC electrodes and devices, *J. Phys. Chem. C.* 122 (2018) 194–206.
- [140] B. Bhattacharyya, Chapter 2--electrochemical machining: macro to micro, *Electrochem. Micromach. Nanofabrication, MEMS Nanotechnol-Ogy.* (2015) 25–52.
- [141] A. Janotti, C.G. de Walle, Fundamentals of zinc oxide as a semiconductor, *Reports Prog. Phys.* 72 (2009) 126501.
- [142] F.-Y. Ma, Corrosive effects of chlorides on metals, *Pitting Corros.* 294 (2012) 139–178.
- [143] K. V Akpanyung, R.T. Loto, Pitting corrosion evaluation: a review, in: *J. Phys. Conf. Ser.*, 2019: p. 22088.
- [144] E.P. on Additives, P. or Substances used in Animal Feed (FEEDAP), Scientific Opinion on the safety and efficacy of tetra-basic zinc chloride for all animal species, *EFSA J.* 10 (2012) 2672.
- [145] Z. Feng, M. An, L. Ren, J. Zhang, P. Yang, Z. Chen, Corrosion mechanism of nanocrystalline Zn--Ni alloys obtained from a new DMH-based bath as a replacement for Zn and Cd coatings, *RSC Adv.* 6 (2016) 64726–64740.
- [146] I. Suzuki, Cathodic Control by Sacrificial Metal, in: *Corros. Coatings*, CRC Press, 1989: p. 25.
- [147] H. Tanaka, A. Fujioka, A. Futoyu, K. Kandori, T. Ishikawa, Synthesis and characterization of layered zinc hydroxychlorides, *J. Solid State Chem.* 180 (2007) 2061–2066.
- [148] Outotec, HSC Chemistry Software v5.11, (2002).
- [149] A. Stirling, I. Papai, H<sub>2</sub>CO<sub>3</sub> Forms via HCO<sub>3</sub><sup>-</sup> in Water, *J. Phys. Chem. B.* 114 (2010) 16854–16859.
- [150] L. Ibsen, Fluids, Electrolytes, and Acid-Base Status in Critical Illness, (n.d.). [http://pedscem.org/FILE-CABINET/Practical/Akron\\_pdfs/8FLUIDS.PDF](http://pedscem.org/FILE-CABINET/Practical/Akron_pdfs/8FLUIDS.PDF).
- [151] A. Fattah-Alhosseini, O. Imantalab, S. Vafaeian, G. Ansari, Corrosion behavior of pure copper surrounded by Hank's physiological electrolyte at 310 K (37 C) as a potential biomaterial for contraception: An analogy drawn between micro-and nano-grained copper, *J. Mater. Eng. Perform.* 26 (2017) 3739–3749.
- [152] M. Gholami, M. Mhaede, F. Pastorek, I. Altenberger, B. Hadzima, M. Wollmann, L. Wagner, Corrosion Behavior and Mechanical Properties of Ultrafine-Grained Pure Copper with Potential as a Biomaterial, *Adv. Eng. Mater.* 18 (2016) 615–623.

- [153] N. Mora, E. Cano, E.M. Mora, J.M. Bastidas, Influence of pH and oxygen on copper corrosion in simulated uterine fluid, *Biomaterials*. 23 (2002) 667–671.
- [154] P.K. Bowen, J.-M. Seitz, R.J. Guillory, J.P. Braykovich, S. Zhao, J. Goldman, J.W. Drelich, Evaluation of wrought Zn–Al alloys (1, 3, and 5 wt% Al) through mechanical and in vivo testing for stent applications, *J. Biomed. Mater. Res. Part B Appl. Biomater.* 106 (2018) 245–258.
- [155] F.C. Porter, *Zinc handbook: properties, processing, and use in design*, Crc Press, 1991.
- [156] H. Li, H. Yang, Y. Zheng, F. Zhou, K. Qiu, X. Wang, Design and characterizations of novel biodegradable ternary Zn-based alloys with IIA nutrient alloying elements Mg, Ca and Sr, *Mater. Des.* 83 (2015) 95–102.
- [157] R.S. Witte, J.S. Witte, *Analysis of Variance (One Factor)*, in: *Statistics (Ber.)*, 11th ed., Wiley, 2017: pp. 292–318.
- [158] T.H. Courtney, *Strengthening of Crystalline Materials*, in: *Mech. Behav. Mater.*, McGraw-Hill, 1990: pp. 186–203.
- [159] B.I. Edelson, W.M. Baldwin, No Title, *Trans. Amer. Soc. Met.* 55 (1962) 230.
- [160] G. Liu, G.J. Zhang, X.D. Ding, J. Sun, K.H. Chen, The influences of multiscale-sized second-phase particles on ductility of aged aluminum alloys, *Metall. Mater. Trans. A*. 35 (2004) 1725–1734.
- [161] I.L. Mogford, The deformation and fracture of two-phase materials, *Metall. Rev.* 12 (1967) 49–68.
- [162] G.E. Dieter, *Elements of the Theory of Plasticity*, in: *Mech. Metall.*, 3rd ed., McGraw-Hill Education, 2013: pp. 77–80.
- [163] A.A. Griffith, VI. The phenomena of rupture and flow in solids, *Philos. Trans. R. Soc. London. Ser. A, Contain. Pap. a Math. or Phys. Character.* 221 (1921) 163–198.
- [164] A.T. Zehnder, Griffith Theory of Fracture, in: *Encycl. Tribol.*, 2013: pp. 1570–1573.
- [165] G.E. Dieter, Fracture, in: *Mech. Metall.*, 3rd ed., McGraw-Hill Education, 2013: pp. 246–249.
- [166] Impress LTD, Cu Zn5, (n.d.). <http://copperalliance.org.uk/uploads/2018/03/cuzn5-cw5001-datasheet-d1.pdf> (accessed September 22, 2018).
- [167] Aurubis, Material Datasheet CuZn5, (n.d.). [http://www.aurubis-stolberg.com/wdb/band/eng/Brass/CuZn5-PNA\\_221\\_EN.pdf](http://www.aurubis-stolberg.com/wdb/band/eng/Brass/CuZn5-PNA_221_EN.pdf) (accessed September 22, 2018).
- [168] M. Krystýnová, P. Doležal, S. Fintová, M. Březina, J. Zapletal, J. Wasserbauer,

- Preparation and characterization of zinc materials prepared by powder metallurgy, *Metals (Basel)*. 7 (2017) 396.
- [169] Los Alamos National Laboratory, Periodic Table of Elements: Zinc, (2016). <https://periodic.lanl.gov/30.shtml> (accessed August 5, 2020).
- [170] Los Alamos National Laboratory, Periodic Table of Elements: Copper, (2016). <https://periodic.lanl.gov/29.shtml> (accessed August 5, 2020).
- [171] Los Alamos National Laboratory, Periodic Table of Elements: Lithium, (2016). <https://periodic.lanl.gov/3.shtml> (accessed August 5, 2020).
- [172] G.E. Dieter, Strengthening Mechanisms, in: *Mech. Metall.*, 3rd ed., McGraw-Hill Education, 2016: pp. 184–240.
- [173] J. Pelleg, Strengthening Mechanisms, in: *Mech. Prop. Mater.*, Springer, 2013: pp. 236–239.
- [174] P. Zhang, S.X. Li, Z.F. Zhang, General relationship between strength and hardness, *Mater. Sci. Eng. A*. 529 (2011) 62–73.
- [175] G. Gottstein, Strengthening Mechanisms, in: *Phys. Found. Mater. Sci.*, Springer, 2004: pp. 264–278.
- [176] H.S. Kim, On the rule of mixtures for the hardness of particle reinforced composites, *Mater. Sci. Eng. A*. 289 (2000) 30–33.
- [177] P. Noell, J. Carroll, K. Hattar, B. Clark, B. Boyce, Do voids nucleate at grain boundaries during ductile rupture?, *Acta Mater.* 137 (2017) 103–114.
- [178] S. Gatea, H. Ou, B. Lu, G. McCartney, Modelling of ductile fracture in single point incremental forming using a modified GTN model, *Eng. Fract. Mech.* 186 (2017) 59–79.
- [179] A. Pineau, A.A. Benzerga, T. Pardoen, Failure of metals I: Brittle and ductile fracture, *Acta Mater.* 107 (2016) 424–483.
- [180] W. Qin, J. Li, Y. Liu, J. Kang, L. Zhu, D. Shu, P. Peng, D. She, D. Meng, Y. Li, Effects of grain size on tensile property and fracture morphology of 316L stainless steel, *Mater. Lett.* 254 (2019) 116–119.
- [181] I. Konovalenko, P. Maruschak, J. Brezinová, J. Brezina, Morphological Characteristics of Dimples of Ductile Fracture of VT23M Titanium Alloy and Identification of Dimples on Fractograms of Different Scale, *Materials (Basel)*. 12 (2019) 2051.
- [182] W.T. Becker, *Ductile and Brittle Fracture*, (2002).
- [183] K. Gall, N. Yang, M. Horstemeyer, D.L. McDowell, J. Fan, The debonding and fracture of Si particles during the fatigue of a cast Al-Si alloy, *Metall. Mater. Trans. A*. 30 (1999)

3079–3088.

- [184] B. Alberts, A. Johnson, J. Lewis, M. Raff, K. Roberts, P. Walter, Fibroblasts and their transformations: the connective-tissue cell family, in: *Mol. Biol. Cell*. 4th Ed., Garland Science, 2002.
- [185] F. Fernandez-Madrid, S. Noonan, J. Riddle, The " spindle-shaped" body in fibroblasts: intracellular collagen fibrils., *J. Anat.* 132 (1981) 157.
- [186] O.L. Huk, I. Catelas, F. Mwale, J. Antoniou, D.J. Zukor, A. Petit, Induction of apoptosis and necrosis by metal ions in vitro, *J. Arthroplasty*. 19 (2004) 84–87.
- [187] L. Fowler, H. Engqvist, C. Öhman-Mägi, Effect of Copper Ion Concentration on Bacteria and Cells, *Materials (Basel)*. 12 (2019) 3798.
- [188] H. Guo, Y. He, Y. Zheng, Y. Cui, In vitro studies of biodegradable Zn-0.1 Li alloy for potential esophageal stent application, *Mater. Lett.* 275 (2020) 128190.
- [189] T. Scientific, 14025 - HBSS, calcium, magnesium, no phenol red, (n.d.). <https://www.thermofisher.com/us/en/home/technical-resources/media-formulation.153.html>.
- [190] T.S.N.S. Narayanan, I.-S. Park, M.-H. Lee, *Surface Modification of Magnesium and Its Alloys for Biomedical Applications: Modification and Coating Techniques*, Elsevier, 2015.

APPENDIX I – HBSS composition and ion concentration

**Table 8:** Composition of HBSS.

<b>Component</b>	<b>Concentration (mg/L)</b>
CaCl <sub>2</sub> (anhydrous)	140
MgCl <sub>2</sub> -6H <sub>2</sub> O	100
MgSO <sub>4</sub> -7H <sub>2</sub> O	100
KCl	400
KH <sub>2</sub> PO <sub>4</sub>	60
NaHCO <sub>3</sub>	350
NaCl	8000
Na <sub>2</sub> HPO <sub>4</sub>	48
D-Glucose (Dextrose)	1000

Reference: [189]

**Table 9:** Ion concentration in HBSS.

<b>Component</b>	<b>Concentration (mmol/L)</b>
Na <sup>+</sup>	145
Cl <sup>-</sup>	144.6
K <sup>+</sup>	5.8
Ca <sup>2+</sup>	1.3
Mg <sup>2+</sup>	0.4
HPO <sub>4</sub> <sup>2-</sup>	0.8
SO <sub>4</sub> <sup>2-</sup>	0.4
d-Glucose	5.5
HCO <sub>3</sub> <sup>-</sup>	±26.2
HEPES	±25

Reference: [190]

APPENDIX II – Zn-Li-Cu CALPHAD TDB code for PANDAT software

```

$ Zn-Li-Cu Ternary System
$ -----
$ 2019.11.19
$
$ TDB file created by J. Young
$
$ The University of Alabama
$
$ The parameter set is taken from:
$ Thermodynamic modeling of the Li-Zn system.
$ Y.Liang, Z.Du, C.Guo, C.Li, J.All.Comp., 455 (2008) 236-242.
$
$ Thermodynamic assessment of the Cu-Li system and prediction of enthalpy
$ of mixing of Cu-Li-Sn liquid alloys.
$ D. Li, S. Furtauer, H. Flandorfer, D.M. Cupid, Calphad, 53 (2016) 105-115.
$
$ Thermodynamic description of the Al-Li-Zn system.
$ C. Guo, Y. Liang, C. Li, Z. Du, Calphad, 35.1 (2011) 54-65.
$
$ Thermodynamic description of the Cu-Zn system.
$ W. Gierlotka, S-w. Chen, J.Mater.Res, 23.1 (2008) 258-263.
$
$ -----
$
ELEMENT /- ELECTRON_GAS      0.0000E+00 0.0000E+00 0.0000E+00!
ELEMENT VA VACUUM           0.0000E+00 0.0000E+00 0.0000E+00!
ELEMENT LI BCC_A2           6.9410E+00 4.6233E+03 2.9096E+01!
ELEMENT ZN HCP_A3           6.5390E+01 5.6568E+03 4.1631E+01!
ELEMENT CU FCC_A1           6.3546E+01 5.0041E+03 3.3150E+01!
$
$ -----
$
FUNCTION GHSERLI 200.00 -10583.817+217.637482*T-38.940488*T*LN(T)
+35.466931E-3*T**2-19.869816E-6*T**3+159994*T**(-1);      453.60 Y
-559579.123+10547.879893*T-1702.8886493*T*LN(T)+2258.329444E-3*T**2
-571.066077E-6*T**3+33885874*T**(-1);      500.00 Y
-9062.994+179.278285*T-31.2283718*T*LN(T)+2.633221E-3*T**2-0.438058E-
6*T**3
-102387*T**(-1);      3000.00 N !

```

FUNCTION GLILIQ 200.00 -7883.612+211.841861\*T-38.940488\*T\*LN(T)  
+35.466931E-3\*T\*\*2-19.869816E-6\*T\*\*3+159994\*T\*\*(-1); 250.00 Y  
+12015.027-362.187078\*T+61.6104424\*T\*LN(T)-182.426463E-3\*T\*\*2  
+63.955671E-6\*T\*\*3-559968\*T\*\*(-1); 453.60 Y  
-6057.31+172.652183\*T-31.2283718\*T\*LN(T)+2.633221E-3\*T\*\*2-0.438058E-  
6\*T\*\*3  
-102387\*T\*\*(-1); 3000.00 N !

FUNCTION GLIFCC 200.00 -10691.817+218.937482\*T-38.940488\*T\*LN(T)  
+35.466931E-3\*T\*\*2-19.869816E-6\*T\*\*3+159994\*T\*\*(-1); 453.60 Y  
-559687.123+10549.179893\*T-1702.8886493\*T\*LN(T)+2258.329444E-3\*T\*\*2  
-571.066077E-6\*T\*\*3+33885874\*T\*\*(-1); 500.00 Y  
-9170.994+180.578285\*T-31.2283718\*T\*LN(T)+2.633221E-3\*T\*\*2-0.438058E-  
6\*T\*\*3  
-102387\*T\*\*(-1); 3000.00 N !

FUNCTION GLIHCP 200.00 -10737.817+219.637482\*T-38.940488\*T\*LN(T)  
+35.466931E-3\*T\*\*2-19.869816E-6\*T\*\*3+159994\*T\*\*(-1); 453.60 Y  
-559733.123+10549.879893\*T-1702.8886493\*T\*LN(T)+2258.329444E-3\*T\*\*2  
-571.066077E-6\*T\*\*3+33885874\*T\*\*(-1); 500.00 Y  
-9216.994+181.278285\*T-31.2283718\*T\*LN(T)+2.633221E-3\*T\*\*2-0.438058E-  
6\*T\*\*3  
-102387\*T\*\*(-1); 3000.00 N !

FUNCTION GHSERZN 298.15  
-7285.787+118.470069\*T-23.701314\*T\*LN(T)-1.712034E-3\*T\*\*2  
-1.264963E-6\*T\*\*3; 692.68 Y  
-11070.559+172.34566\*T-31.38\*T\*LN(T)+470.514E24\*T\*\*(-9); 1700.00 N !

FUNCTION GZNLIQ 298.15  
-128.574+108.177079\*T-23.701314\*T\*LN(T)-1.712034E-3\*T\*\*2-1.264963E-  
6\*T\*\*3  
-358.958E-21\*T\*\*7; 692.68 Y  
-3620.391+161.608594\*T-31.38\*T\*LN(T); 1700.00 N !

FUNCTION GZNFCC 298.15  
-4315.967+116.900389\*T-23.701314\*T\*LN(T)-1.712034E-3\*T\*\*2-1.264963E-  
6\*T\*\*3;  
692.68 Y  
-8100.739+170.77598\*T-31.38\*T\*LN(T)+470.514E24\*T\*\*(-9); 1700.00 N !

FUNCTION GZNBCC 298.15  
-4398.827+115.959669\*T-23.701314\*T\*LN(T)-1.712034E-3\*T\*\*2-1.264963E-  
6\*T\*\*3;  
692.68 Y

```

-8183.599+169.83526*T-31.38*T*LN(T)+470.514E24*T**(-9);      1700.00 N !

FUNCTION GHSERCU  298.15 -7770.458+130.485403*T-24.112392*T*LN(T)
-.00265684*T**2+1.29223E-07*T**3+52478*T**(-1);      1358.01 Y
-13542.33+183.804197*T-31.38*T*LN(T)+3.64643E+29*T**(-9);  2000 N !

FUNCTION GCULIQ  298.15 +12964.84-9.510243*T-5.839E-
21*T**7+GHSERCU#;
                                1358.01 Y
+13495.4-9.920463*T-3.646E+29*T**(-9)+GHSERCU#;      2000 N !

FUNCTION GCUBCC  298.15 +4017-1.255*T+GHSERCU#;      3200 N !

$-----
TYPE_DEFINITION % SEQ *!
DEFINE_SYSTEM_DEFAULT ELEMENT 2 !
DEFAULT_COMMAND DEF_SYS_ELEMENT VA /- !

$-----
$ PARAMETERS FOR LIQUID PHASE
$-----
PHASE LIQUID % 1 1.0 !
CONSTITUENT LIQUID :LI,ZN,CU : !
PARAMETER G(LIQUID,LI;0)  298.15 +GLILIQ#;      3000 N !
PARAMETER G(LIQUID,ZN;0)  298.15 +GZNLIQ#;      1700 N !
PARAMETER G(LIQUID,CU;0)  298.15 +GCULIQ#;      3200 N !
PARAMETER G(LIQUID,LI,ZN;0) 298.15 -45258.6+26.3677*T;      6000 N !
PARAMETER G(LIQUID,LI,ZN;1) 298.15 +22887.2-4.1921*T;      6000 N !
PARAMETER G(LIQUID,LI,ZN;2) 298.15 -4552.6+4.0715*T;      6000 N !
PARAMETER G(LIQUID,CU,ZN;0) 298.15 -84075.696+335.98*T-
40.5377*T*LN(T);
                                6000 N !
PARAMETER G(LIQUID,CU,ZN;1) 298.15 -7230.333+3.89*T;      6000 N !
PARAMETER G(LIQUID,CU,ZN;2) 298.15 +3104.189-0.124*T;      6000 N !
PARAMETER G(LIQUID,CU,LI;0) 298.15 +11794.6115+1.78*T-
2.72360272*T*LN(T);
                                6000 N !
PARAMETER G(LIQUID,CU,LI;1) 298.15 -22042.9488+29*T-1.4*T*LN(T); 6000
N !
PARAMETER G(LIQUID,CU,LI;2) 298.15 -14500+16*T-1.15*T*LN(T);  6000
N !

$-----
$ FUNCTIONS FOR LIZN
$-----

```

PHASE LIZN % 3 0.5 0.5 3 !

```
  CONSTITUENT LIZN : LI,ZN : LI,ZN : VA : !
  PARAMETER G(LIZN,LI:LI:VA;0) 298.15 +0; 6000 N !
  PARAMETER G(LIZN,ZN:ZN:VA;0) 298.15 +0; 6000 N !
  PARAMETER G(LIZN,LI:ZN:VA;0) 298.15 -26930.7+10.006*T; 6000 N !
  PARAMETER G(LIZN,ZN:LI:VA;0) 298.15 -26930.7+10.006*T; 6000 N !
  PARAMETER G(LIZN,LI,ZN:LI:VA;0) 298.15 -26474.4+30.2611*T; 6000 N !
  PARAMETER G(LIZN,LI:LI,ZN:VA;0) 298.15 -26474.4+30.2611*T; 6000 N !
  PARAMETER G(LIZN,LI,ZN:LI:VA;1) 298.15 -11635.9+1.4065*T; 6000 N !
  PARAMETER G(LIZN,LI:LI,ZN:VA;1) 298.15 -11635.9+1.4065*T; 6000 N !
  PARAMETER G(LIZN,LI,ZN:ZN:VA;0) 298.15 -13623.4+1.7890*T; 6000 N !
  PARAMETER G(LIZN,ZN:LI,ZN:VA;0) 298.15 -13623.4+1.7890*T; 6000 N !
  PARAMETER G(LIZN,LI,ZN:ZN:VA;1) 298.15 -4786.2-4.0231*T; 6000 N !
  PARAMETER G(LIZN,ZN:LI,ZN:VA;1) 298.15 -4786.2-4.0231*T; 6000 N !
```

\$-----

\$ FUNCTIONS FOR BCC\_A2

\$-----

TYPE\_DEFINITION > GES AMEND\_PHASE\_DESCRIPTION BCC\_A2 MAGNETIC  
-1.0 4E-01 !

PHASE BCC\_A2 %> 2 1 3 !

```
  CONSTITUENT BCC_A2 : LI,ZN,CU : VA : !
  PARAMETER G(BCC_A2,LI:VA;0) 298.15 +GHSERLI#; 3000 N !
  PARAMETER G(BCC_A2,ZN:VA;0) 298.15 +GZNBCC#; 1700 N !
  PARAMETER G(BCC_A2,CU:VA;0) 298.15 +GCUBCC#; 3200 N !
  PARAMETER G(BCC_A2,LI,ZN:VA;0) 298.15 -54260.4+45.7720*T; 6000 N !
  PARAMETER G(BCC_A2,LI,ZN:VA;1) 298.15 +25153.3; 6000 N !
  PARAMETER G(BCC_A2,CU,LI:VA;0) 298.15 +50000; 6000 N !
```

\$-----

\$ PARAMETERS FOR LIZN4\_BETA

\$-----

PHASE LIZN4\_BETA %' 3 .2 .8 .5 !

```
  CONSTITUENT LIZN4_BETA : LI,ZN : LI,ZN : VA : !
  PARAMETER G(LIZN4_BETA,LI:LI:VA;0) 298.15 +0; 6000 N !
  PARAMETER G(LIZN4_BETA,ZN:ZN:VA;0) 298.15 +0; 6000 N !
  PARAMETER G(LIZN4_BETA,LI:ZN:VA;0) 298.15 -191.117297-0.0855*T; 6000
```

N !

```
  PARAMETER G(LIZN4_BETA,ZN:LI:VA;0) 298.15 +191.117297+0.0855*T; 6000
```

N !

```
  PARAMETER G(LIZN4_BETA,LI,ZN:LI:VA;0) 298.15 +4904.759-1.9606*T;
    6000 N !
  PARAMETER G(LIZN4_BETA,LI,ZN:LI:VA;1) 298.15 -7361.9444+8.2575*T;
    6000 N !
  PARAMETER G(LIZN4_BETA,LI:LI,ZN:VA;0) 298.15 +20574.6225-7.4146*T;
    6000 N !
```

PARAMETER G(LIZN4\_BETA,LI:LI,ZN:VA;1) 298.15 -29447.7776+33.0299\*T;  
 6000 N!  
 PARAMETER G(LIZN4\_BETA,ZN:LI,ZN:VA;0) 298.15 +19682.1047-7.8141\*T;  
 6000 N!  
 PARAMETER G(LIZN4\_BETA,ZN:LI,ZN:VA;1) 298.15 -29447.7776+33.0299\*T;  
 6000 N!  
 PARAMETER G(LIZN4\_BETA,LI,ZN:ZN:VA;0) 298.15 +5159.5184-1.8466\*T;  
 6000 N!  
 PARAMETER G(LIZN4\_BETA,LI,ZN:ZN:VA;1) 298.15 -7361.9444+8.2575\*T;  
 6000 N!

\$-----  
 \$ PARAMETERS FOR HCP\_A3  
 \$-----

TYPE\_DEFINITION 'GES AMEND\_PHASE\_DESCRIPTION LIZN4\_BETA  
 DIS\_PART HCP\_A3,,,!  
 PHASE HCP\_A3 % 2 1.0 .5 !  
 CONSTITUENT HCP\_A3 :LI, ZN, CU : VA : !  
 PARAMETER G(HCP\_A3,LI:VA;0) 298.15 +GLIHCP#; 3200 N!  
 PARAMETER G(HCP\_A3,ZN:VA;0) 298.15 +GHSERZN#; 3800 N!  
 PARAMETER G(HCP\_A3,CU:VA;0) 298.15 +600+0.2\*T+GHSERCU#; 3200  
 N!  
 PARAMETER G(HCP\_A3,LI,ZN:VA;0) 298.15 -29301.52-.2586\*T; 6000 N!  
 PARAMETER G(HCP\_A3,LI,ZN:VA;1) 298.15 +15702.15+3.5167\*T; 6000 N!  
 PARAMETER G(HCP\_A3,CU,ZN:VA;0) 298.15 -14432.17-10.7814\*T; 6000 N!

\$-----  
 \$ PARAMETERS FOR FCC\_A1  
 \$-----

TYPE\_DEFINITION < GES AMEND\_PHASE\_DESCRIPTION FCC\_A1 MAGNETIC  
 -3.0 2.8E-01 !  
 PHASE FCC\_A1 %< 2 1.0 1 !  
 CONSTITUENT FCC\_A1 :CU,ZN,LI : VA : !  
 PARAMETER G(FCC\_A1,CU:VA;0) 298.15 +GHSERCU#; 3200 N!  
 PARAMETER G(FCC\_A1,ZN:VA;0) 298.15 +GZNFCC#; 3000 N!  
 PARAMETER G(FCC\_A1,LI:VA;0) 298.15 +GLIFCC#;  
 3000 N!  
 PARAMETER G(FCC\_A1,CU,ZN:VA;0) 298.15 -42803.75+10.02258\*T; 6000  
 N!  
 PARAMETER G(FCC\_A1,CU,ZN:VA;1) 298.15 +2936.39-3.05323\*T; 6000 N!  
 PARAMETER G(FCC\_A1,CU,ZN:VA;2) 298.15 +9034.20-5.39314\*T; 6000 N!  
 PARAMETER G(FCC\_A1,CU,LI:VA;0) 298.15 +34383.0459-70.0863278\*T  
 +11.3754566\*T\*LN(T);  
 6000 N!  
 PARAMETER G(FCC\_A1,CU,LI:VA;1) 298.15 -204984.122+140.574711\*T; 6000  
 N!

```

$-----
$ PARAMETERS FOR LI2ZN3_ALPHA
$-----
PHASE LI2ZN3_ALPHA % 2 2 3 !
  CONSTITUENT LI2ZN3_ALPHA :LI :LI,ZN : !
  PARAMETER G(LI2ZN3_ALPHA,LI:ZN;0) 298.15 -85329.5+30.2362*T
    +2*GHSERLI#+3*GHSERZN#; 6000 N !
  PARAMETER G(LI2ZN3_ALPHA,LI:LI;0) 298.15 +19964.6+5*GHSERLI#; 6000
N !
  PARAMETER G(LI2ZN3_ALPHA,LI:LI,ZN;0) 298.15 -7720.6+12.5469*T; 6000
N !
  PARAMETER G(LI2ZN3_ALPHA,LI:LI,ZN;1) 298.15 +1001.2+1.0070*T; 6000
N !

```

```

$-----
$ PARAMETERS FOR LI2ZN3_BETA
$-----
PHASE LI2ZN3_BETA % 2 2 3 !
  CONSTITUENT LI2ZN3_BETA :LI,ZN :LI,ZN : !
  PARAMETER G(LI2ZN3_BETA,LI:ZN;0) 298.15 -84218.4+27.7580*T
    +2*GHSERLI#+3*GHSERZN#; 6000 N !
  PARAMETER G(LI2ZN3_BETA,ZN:LI;0) 298.15 +84218.4-27.7580*T
    +3*GHSERLI#+2*GHSERZN#; 6000 N !
  PARAMETER G(LI2ZN3_BETA,LI:LI;0) 298.15 +9307.8+5*GHSERLI#; 6000
N !
  PARAMETER G(LI2ZN3_BETA,ZN:ZN;0) 298.15 +9307.8+5*GHSERZN#;
6000 N !
  PARAMETER G(LI2ZN3_BETA,*:LI,ZN;0) 298.15 +7367.6+6.9984*T; 6000 N !
  PARAMETER G(LI2ZN3_BETA,*:LI,ZN;1) 298.15 +8734.9-11.9000*T; 6000
N !
  PARAMETER G(LI2ZN3_BETA,LI,ZN:*;0) 298.15 -87667.4+59.7976*T; 6000
N !
  PARAMETER G(LI2ZN3_BETA,LI,ZN:*;1) 298.15 +49513.8-70.0108*T; 6000
N !

```

```

$-----
$ PARAMETERS FOR LIZN2
$-----
PHASE LIZN2 % 2 1 2 !
  CONSTITUENT LIZN2 :LI : ZN : !
  PARAMETER G(LIZN2,LI:ZN;0) 298.15 -52025.3+20.4705*T
    +GHSERLI#+2*GHSERZN#; 6000 N !

```

```

$-----
$ PARAMETERS FOR LI2ZN5_ALPHA

```

```

$-----
PHASE LI2ZN5_ALPHA % 2 2 5 !
  CONSTITUENT LI2ZN5_ALPHA :LI,ZN :ZN : !
  PARAMETER G(LI2ZN5_ALPHA,LI:ZN;0) 298.15 -122660.9+51.3440*T
    +2*GHSERLI#+5*GHSERZN#; 6000 N !
  PARAMETER G(LI2ZN5_ALPHA,ZN:ZN;0) 298.15 +12169.3+7*GHSERZN#;
6000 N !
  PARAMETER G(LI2ZN5_ALPHA,LI,ZN:ZN;0) 298.15 -7605.3; 6000 N !

$-----
$ PARAMETERS FOR LI2ZN5_BETA
$-----
PHASE LI2ZN5_BETA % 2 2 5 !
  CONSTITUENT LI2ZN5_BETA :LI,ZN :ZN : !
  PARAMETER G(LI2ZN5_BETA,LI:ZN;0) 298.15 -122652.3+51.3303*T
    +2*GHSERLI#+5*GHSERZN#; 6000 N !
  PARAMETER G(LI2ZN5_BETA,ZN:ZN;0) 298.15 +26766.0+7*GHSERZN#;
6000 N !
  PARAMETER G(LI2ZN5_BETA,LI,ZN:ZN;0) 298.15 -7128.3; 6000 N !
  PARAMETER G(LI2ZN5_BETA,LI,ZN:ZN;1) 298.15 -30111.7; 6000 N !

$-----
$ PARAMETERS FOR LIZN4_ALPHA
$-----
PHASE LIZN4_ALPHA % 2 1 4 !
  CONSTITUENT LIZN4_ALPHA :LI,ZN :LI,ZN : !
  PARAMETER G(LIZN4_ALPHA,LI:ZN;0) 298.15 -78372+43.2115*T
    +GHSERLI#+4*GHSERZN#; 6000 N !
  PARAMETER G(LIZN4_ALPHA,ZN:LI;0) 298.15 +78372-43.2115*T
    +4*GHSERLI#+GHSERZN#; 6000 N !
  PARAMETER G(LIZN4_ALPHA,LI:LI;0) 298.15 +15000.0+5*GHSERLI#; 6000
N !
  PARAMETER G(LIZN4_ALPHA,ZN:ZN;0) 298.15 +15000.0+5*GHSERZN#;
6000 N !
  PARAMETER G(LIZN4_ALPHA,*:LI,ZN;0) 298.15 -18698.3+7.7695*T; 6000
N !
  PARAMETER G(LIZN4_ALPHA,LI,ZN:*;0) 298.15 -33953.6+20.1515*T; 6000
N !

$-----
$ PARAMETERS FOR ε
$-----
PHASE EPSILON % 1 1.0 !
  CONSTITUENT EPSILON :CU,ZN : !
  PARAMETER G(EPSILON,CU;0) 298.15 +GHSERCU#; 6000 N !

```

N!  
 PARAMETER G(EPSILON,ZN;0) 298.15 +2969.82-1.56968\*T+GHSERZN#; 6000  
 PARAMETER G(EPSILON,CU,ZN;0) 298.15 -35433.3+5.24516\*T; 6000 N!  
 PARAMETER G(EPSILON,CU,ZN;1) 298.15 +25276.81-9.96989\*T; 6000 N!

\$-----  
 \$ PARAMETERS FOR BCC- $\beta$ , $\delta$   
 \$-----

PHASE BETA % 1 1.0!  
 CONSTITUENT BETA :CU,ZN :!  
 PARAMETER G(BETA,CU;0) 298.15 +GCUBCC#; 3200 N!  
 PARAMETER G(BETA,ZN;0) 298.15 +GZNBCC#; 3000 N!  
 PARAMETER G(BETA,CU,ZN;0) 298.15 -51595.87+13.06392\*T; 6000 N!  
 PARAMETER G(BETA,CU,ZN;1) 298.15 +7562.13-6.45432\*T; 6000 N!  
 PARAMETER G(BETA,CU,ZN;2) 298.15 +30743.74-29.91503\*T; 6000 N!

\$-----  
 \$ PARAMETERS FOR  $\beta'$   
 \$-----

PHASE BETA2 % 1 1.0!  
 CONSTITUENT BETA2 :CU,ZN :!  
 PARAMETER G(BETA2,CU;0) 298.15 +GCUBCC#; 3200 N!  
 PARAMETER G(BETA2,ZN;0) 298.15 +GZNBCC#; 3000 N!  
 PARAMETER G(BETA2,CU,ZN;0) 298.15 -56815.585+20.1526\*T; 6000 N!  
 PARAMETER G(BETA2,CU,ZN;1) 298.15 +7742.904-6.4549\*T; 6000 N!  
 PARAMETER G(BETA2,CU,ZN;2) 298.15 +30743.740-29.9210\*T; 6000 N!

\$-----  
 \$ PARAMETERS FOR  $\gamma$   
 \$-----

PHASE GAMMA % 4 0.15385 0.15385 0.23076 0.46154!  
 CONSTITUENT GAMMA :CU,ZN :CU,ZN :CU :ZN :!  
 PARAMETER G(GAMMA,CU:CU:CU:ZN;0) 298.15  
 +0.53846\*GHSERCU#+0.46154\*GHSERZN#  
 -9132.295645-3.257625638\*T; 6000 N!  
 PARAMETER G(GAMMA,ZN:CU:CU:ZN;0) 298.15  
 +0.38462\*GHSERCU#+0.61538\*GHSERZN#  
 -3395.352225-5.265766609\*T; 6000 N!  
 PARAMETER G(GAMMA,CU:ZN:CU:ZN;0) 298.15  
 +0.38462\*GHSERCU#+0.61538\*GHSERZN#  
 -11552.71-1.67824\*T; 6000 N!  
 PARAMETER G(GAMMA,ZN:ZN:CU:ZN;0) 298.15  
 +0.23076\*GHSERCU#+0.76924\*GHSERZN#  
 -5815.76658-3.686380972\*T; 6000 N!

APPENDIX III – Example calculation of corrosion rate

Immersion corrosion rate based on sample weight loss can be calculated by:

$$CR = \frac{87.6 \cdot \Delta W}{A \cdot t \cdot \rho}$$

Example: A single measurement for pure Zn after 12 days of immersion.

Initial weight = 1.2021 g; final weight = 1.2016 g;  $\Delta W = 0.5$  mg.

Additionally, sample geometry is rectangular prism with hole. Dimensions of the sample are provided in Figure 48.

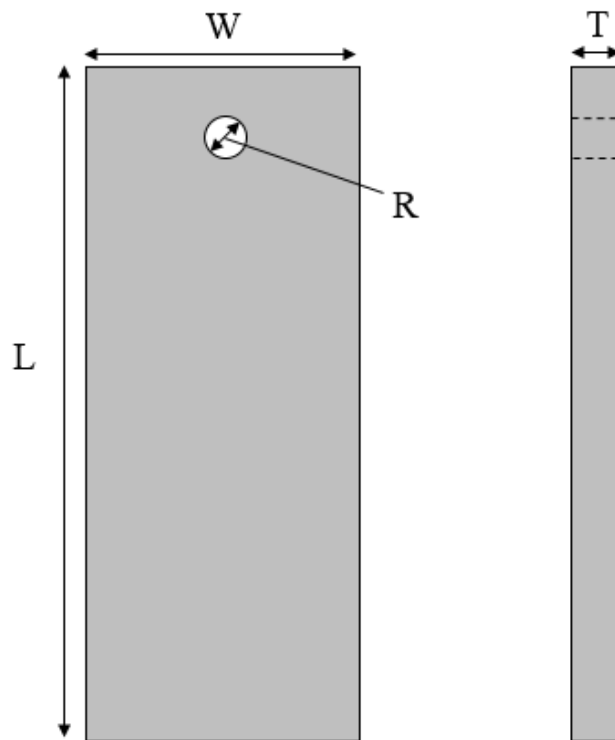


**Figure 48:** Front and side view of corrosion sample.

Given width (W) = 0.942 cm, length (L) = 1.112 cm, thickness (T) = 0.174 cm, and radius (R) = 0.0795 cm, sample surface area is calculated as:

$$A = [(2 \cdot W \cdot L) + (2 \cdot W \cdot H) + (2 \cdot T \cdot H)] - (2\pi R^2) + (2\pi \cdot R \cdot T) = 2.857 \text{ cm}^2$$

Duration (t) of the test is 12 days = 288 h.

Density ( $\rho$ ) of Zn = 7.14 g/cm<sup>3</sup>

$$\therefore CR = \frac{87.6 \cdot 0.5}{2.857 \cdot 288 \cdot 7.14} = 0.00746 \text{ mm/yr}$$

#### APPENDIX IV – Example calculation of Vickers hardness

The shape of the Vickers hardness indenter is a square-based pyramid with angle of  $136^\circ$  between opposite faces, shown in Figure 49.

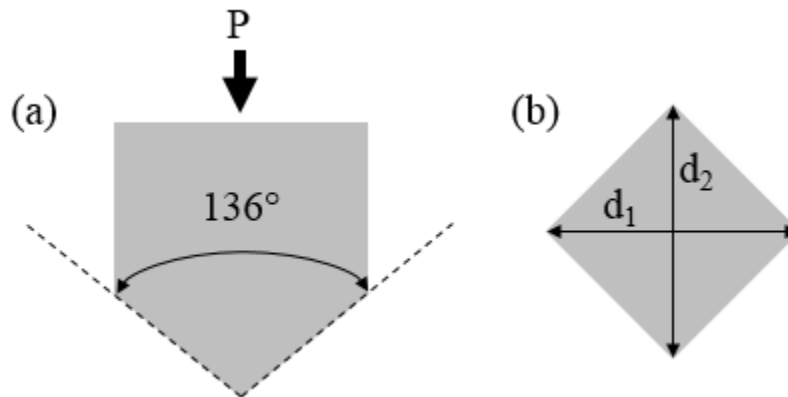


**Figure 49:** Schematic of (a) Vickers hardness indenter and (b) shape of indentation.

$HV = \frac{P}{A}$  where  $A$  is surface area of indentation.

$$\text{Also, } A = \frac{d_1 d_2}{2 \sin(136^\circ/2)} = \frac{d_1 d_2}{1.8544}$$

$$\therefore HV = \frac{1.8544 \cdot P}{d_1 d_2}$$

Example: A single measurement for hot-rolled pure Zn where  $P = 0.2$  kgf gives:  $d_1 = 0.0925$  mm and  $d_2 = 0.1005$  mm.

$$HV = \frac{1.8544 \cdot 0.2}{0.0925 \cdot 0.1005} = 39.89 \frac{kg}{mm^2} = 39.89 HV0.2$$

APPENDIX V – Optical microscopy of NIH3T3 cells

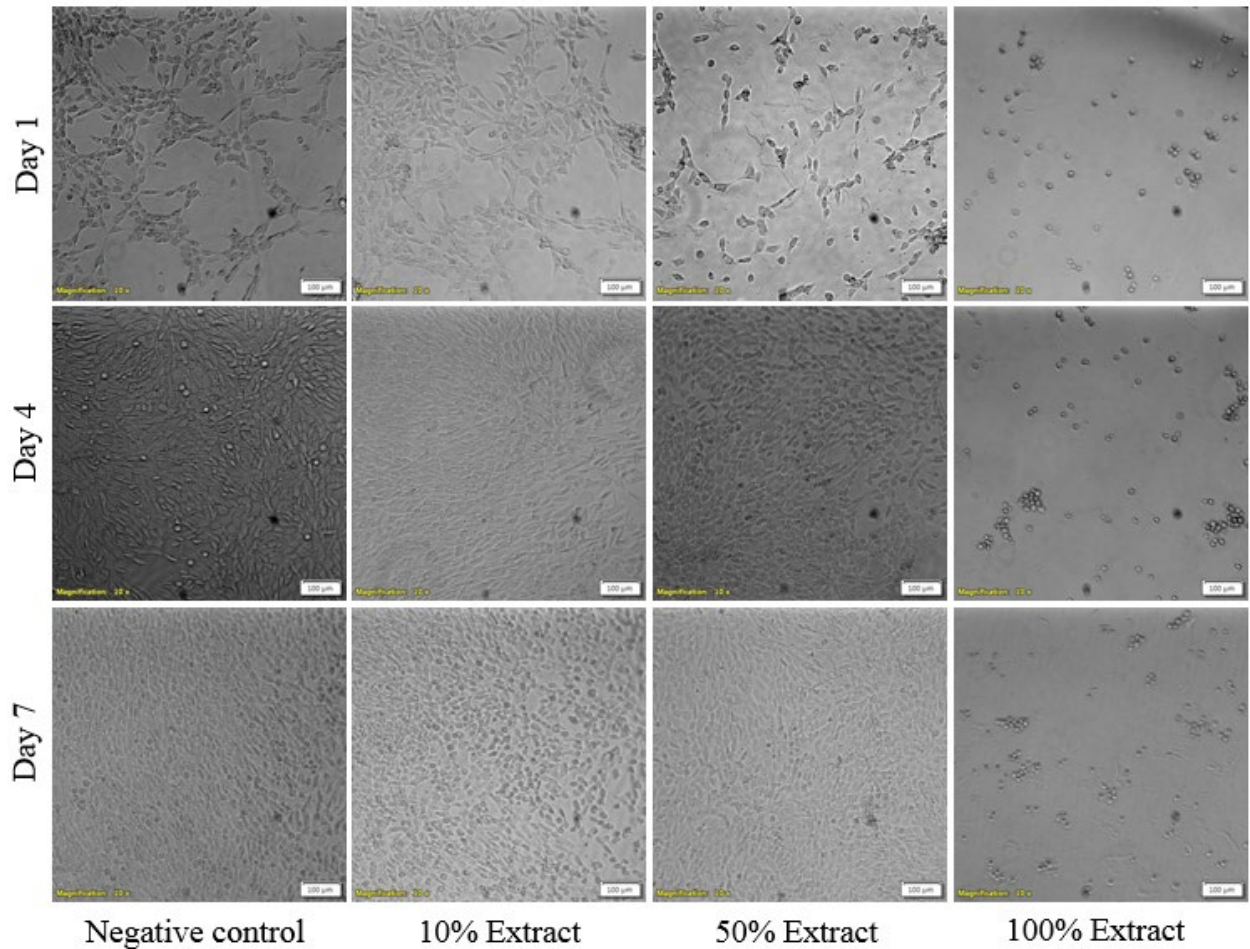


**Figure 50:** Representative optical images of NIH3T3 cells incubated with 10%, 50%, and 100% pure Zn and negative control extracts for 1, 4, and 7 days.

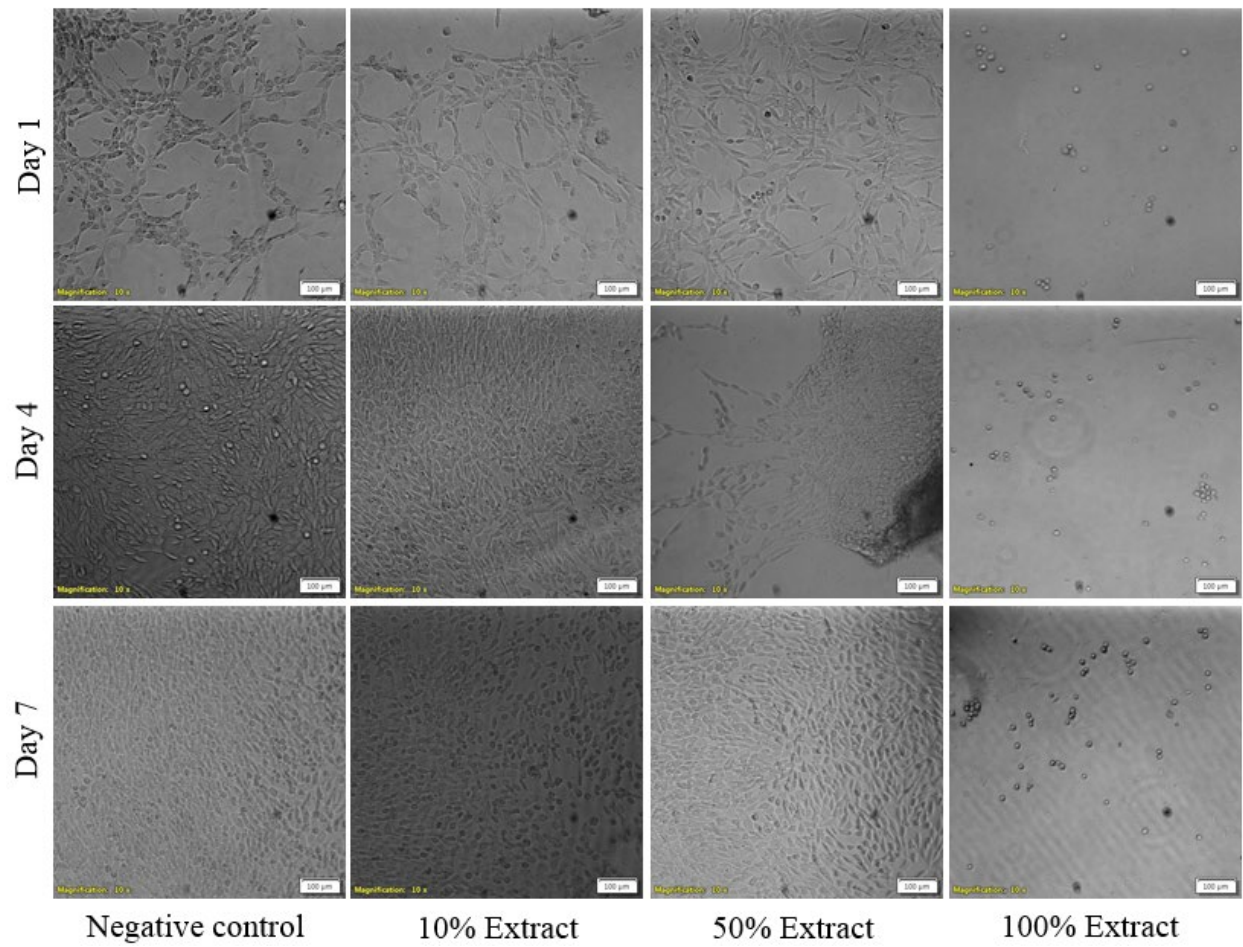


**Figure 51:** Representative optical images of NIH3T3 cells incubated with 10%, 50%, and 100% Zn-0.3Li-2Cu alloy and negative control extracts for 1, 4, and 7 days.

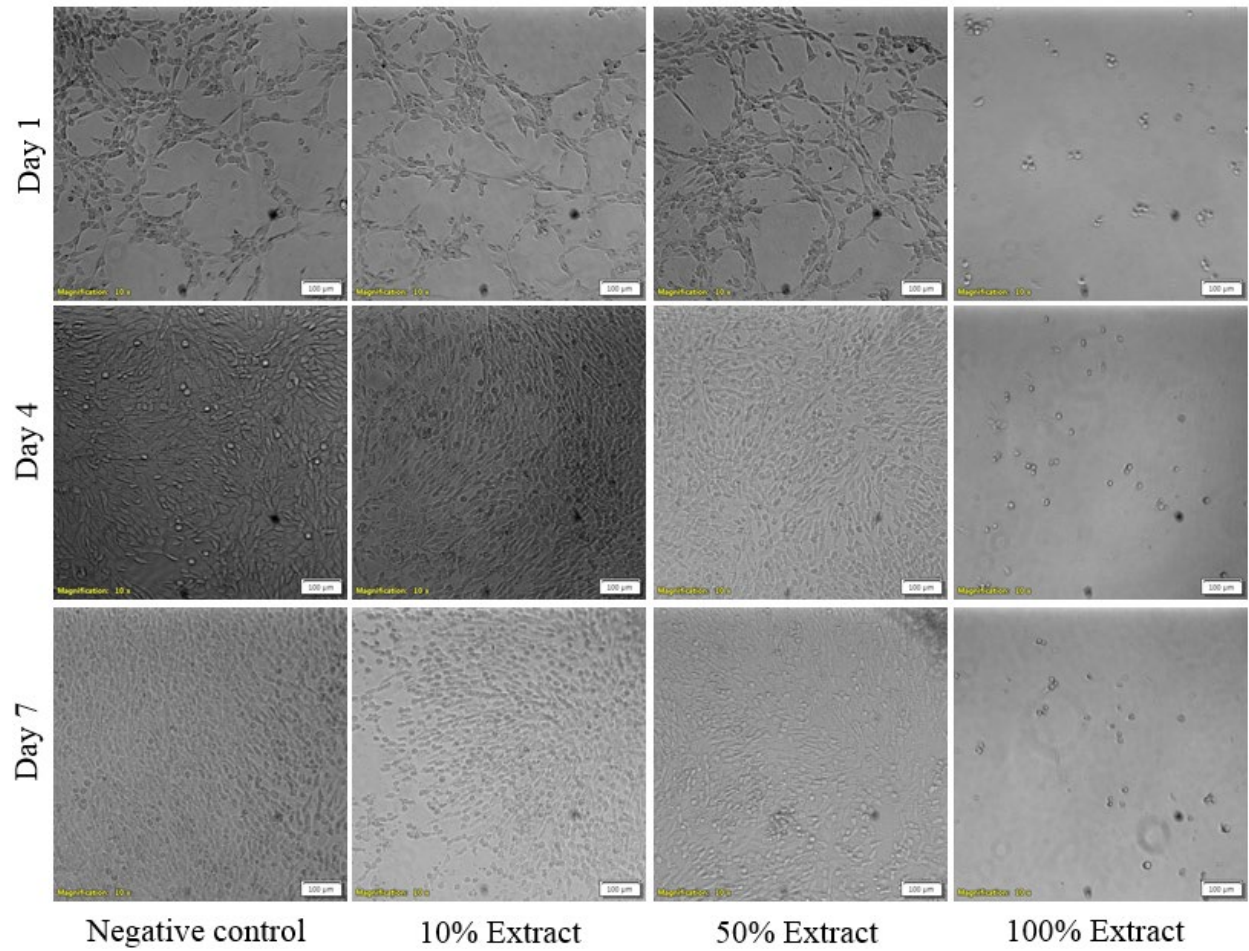


**Figure 52:** Representative optical images of NIH3T3 cells incubated with 10%, 50%, and 100% Zn-0.3Li-3.5Cu alloy and negative control extracts for 1, 4, and 7 days.

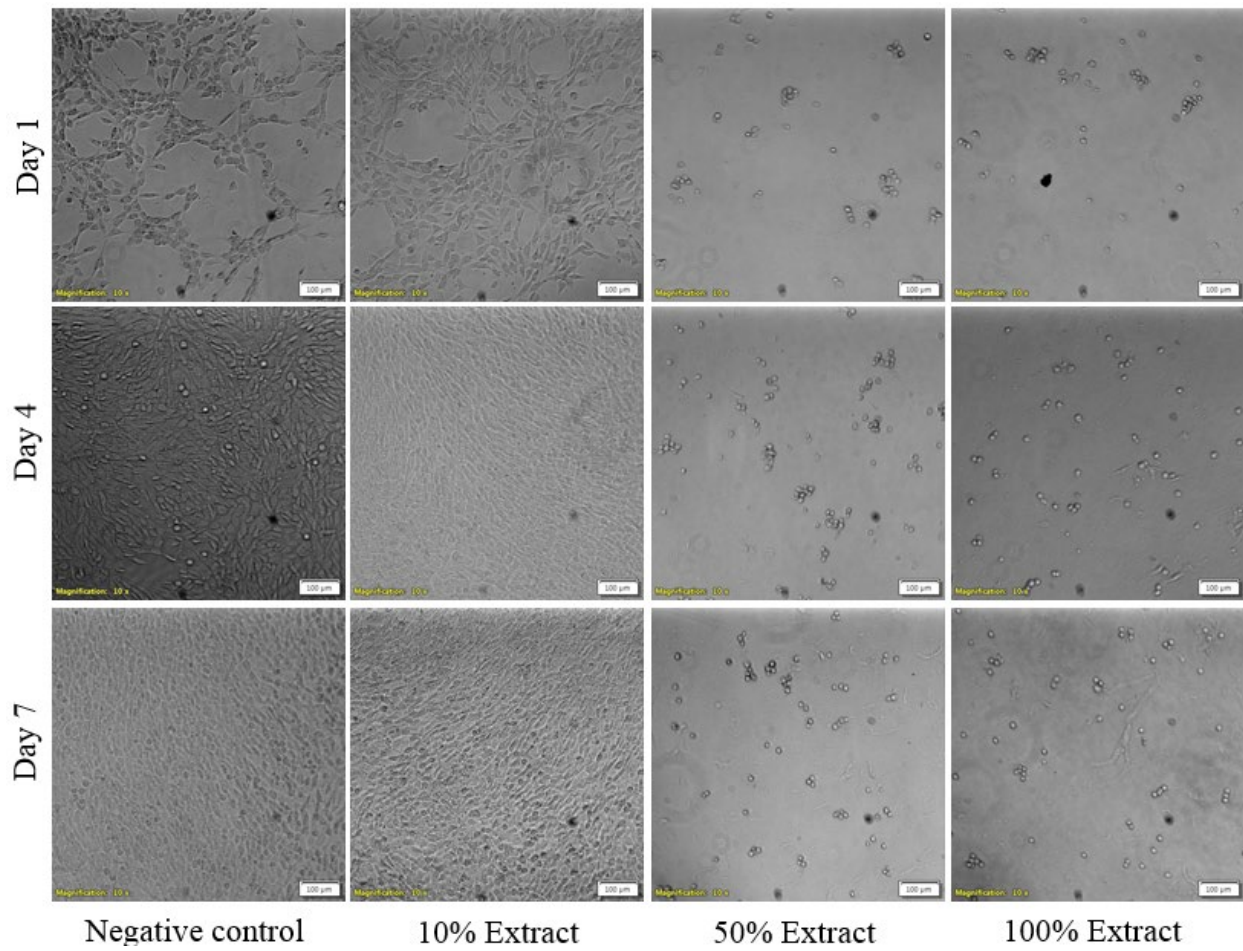


**Figure 53:** Representative optical images of NIH3T3 cells incubated with 10%, 50%, and 100% Zn-0.3Li-5Cu alloy and negative control extracts for 1, 4, and 7 days.